The Kinematics of Circumstellar Disks around T Tauri Stars

Thesis by

David W. Koerner

In Partial Fulfillment of the Requirements

for the Degree of

Doctor of Philosophy

California Institute of Technology

Pasadena, California

1995

(Defended September 13, 1994)

Acknowledgments

There are many people who have contributed, directly and indirectly, to work presented here on the kinematics of circumstellar disks. Indisputably first and foremost among them is my thesis advisor, Anneila Sargent. Together with her collaborator, S.V.W. Beckwith, she virtually founded the entire field of investigation with the discovery of systematic velocity variations in a gaseous disk around HL Tauri. This work could not exist without her seminal contribution, and I count it a tremendous privilege to have enjoyed the benefits of her rich research background and experience. However, I owe an even greater debt to her as the recipient of high-quality mentoring above and beyond the call of duty. Her encouragement, support, and expert professional guidance have been helpful in far too many ways to be listed here; I can only say that I count myself extremely lucky among graduate students!

Thanks must also go to a veritable community of individuals responsible for the immensely successful operation of the Owens Valley Millimeter Array. Observations presented here are innovative largely because they were obtained with an instrument on the cutting edge of technology, and I'm deeply thankful for the scientific and technical skill of those responsible for what is assuredly one of the premier scientific instruments of our time. I am especially grateful for the vision of Nick Scoville, Director of Owens Valley Radio Observatory, that continues to drive this development, and I thank him for the generous policy that permits liberal access to graduate students. Mention must also be made of the genius displayed by highly competent on-site astronomers, Steve Scott, Steve Padin, and Dave Woody, and that virtuoso of mm-wave interferometry, John Carlstrom. Although I have not worked directly for any of these, I am acutely aware that much of the credit for the opportunity to do this work goes to them. Heart-felt thanks!

There are several people whose direct contribution to this work must also not

go unmentioned. I thank Dave Stevenson for many discussions which contributed directly to the modeling in this work and for early review of parts of the manuscript. Claire Chandler took full responsibility for preparing VLA observe files at a critical time, leaving me free to concentrate on completing the text. Steve Leroy and Stuart McMuldroch provided valuable assistance in adapting a widely used set of TEX macros to get this work into its present form. Finally, at the last minute, Gery Allan assisted with proofreading of the entire manuscript and typing references.

Personal thanks must also be extended to those who have been helpful during observing runs and with data reduction. The millimeter array is an increasingly complex instrument; Tony Phillips was enormously helpful with on-the-spot trouble shooting. His expertise and re-assuring manner have lowered my blood pressure on numerous occassions. For assistance with observing and data reduction and general camaraderie, I thank fellow graduate students Rachel Akeson, Peter Bryant, and Mark Gurwell, and Post-Docs Min Yun and Eugene de Geus. More recently, Celeste Sleeper has given needed inspiration with her enthusiasm for the subject of planet formation. Lastly, the graduate student to whom I owe most is Stuart McMuldroch. Early conversations encouraged my initial decision to pursue this line of study, and subsequent interactions have spanned a vast range of technical, philosophical, and personal subjects that have continued to make it meaningful.

Finally, I am extremely fortunate to have the benefit of enviable domestic support. I owe a great deal to my Significant Other, Gery, and children Noah and Rachel. They have showed tremendous love and patience during my tenure as a graduate student. Together with my supportive parents, we have experienced the very best that "Family Values" can offer, and I greatly look forward to spending a greater amount of post-graduate "quality time" with them.

Abstract

Aperture synthesis images of molecular gas around the T Tauri stars, GM Aurigae, RY Tauri, DL Tauri, DO Tauri, and AS 209 are interpreted with the aid of a kinematic model of a circumstellar disk. The velocity structure and morphology of the gas strongly suggest that circumstellar disks with radii of a few hundred AU are present around all five stars. Explicit identification of kinematic patterns in the spectral line maps is achieved for the two largest disks, GM Aur and DO Tau.

Maps of the relatively old T Tauri star, GM Aur, in the ^{13}CO(2→1) line at 4″ resolution reveal compact gas associated with the stellar position and at the core of a larger rotating gaseous disk, 950 × 530 AU in extent. The mean velocity gradient across the disk, which is oriented along PA ≈ 50°, is consistent with rotation about an axis at PA = 140°. The structure observed in ^{13}CO aperture synthesis maps agrees well with synthetic maps of the gas emission generated from a model. For a disk that is inclined 30° from face on, in Keplerian rotation, a 0.80 $M_\odot$ central mass (star + disk), a systemic velocity, V_{HEL}, of 15.38 km s^{-1}, and a mass, 0.1 $M_\odot$ is derived.

A survey of T Tauri stars for circumstellar molecular gas also yields evidence for rotating disks. RY Tau, DL Tau, DO Tau, and AS 209 are detected in CO(2→1) emission elongated along PA ≈ 48°, 84°, 160°, and 138°, respectively, with deconvolved half-maximum radii of 110, 250, 350, and 290 AU in aperture synthesis images at ∼ 2-3″ resolution. Three of these, RY Tau, DL Tau, and AS 209, exhibit velocity gradients parallel to this direction in first moment velocity maps, suggesting rotation of the circumstellar gas. Spectra of RY Tau and AS 209 exhibit a characteristic double-peaked shape, but that of DO Tau is dominated by the presence of high-velocity blue-shifted gas. DL Tau's spectrum has a linewidth that is too narrow (ΔV = 1 km s^{-1}) to be resolved into double peaks. Position-Velocity Diagrams (PVDs) constructed parallel and perpendicular to the axis of elongation imply rotation and infall or outflow, re-

spectively. Those for RY Tau, DL Tau, and AS 209 show predominantly rotation, but some evidence of an orthogonal gradient (infall or outflow) is seen for RY Tau and AS 209. In contrast, the PVDs for DO tau suggest that its molecular emission originates predominantly from outflow or infall.

Recent evidence of infall in circumstellar gas around T Tauri stars has motivated construction of a kinematic model of molecular emission from a disk of rotating and infalling gas. The velocity structure of the model disk assumes that infalling gas obeys angular momentum conservation on ballistic trajectories until it reaches the radial value, R_{disk}, where the magnitude of the rotational velocity component reaches the Keplerian value. For $R < R_{disk}$, gas is assumed to be in circular Keplerian orbits. Synthetic spectral line maps are generated by the model and cross-correlated with aperture synthesis maps for a range of the free parameters, including R_{disk}. The best-fit value of R_{disk} for RY Tau, DL Tau, and AS 209, approximately matches that of the outer radius of their emission, indicating these disks are predominantly in Keplerian rotation. However, emission from these stars is marginally resolved and uncertainties in the best-fit parameters are correspondingly high. In contrast, kinematic patterns are well-resolved in emission from DO Tau found in maps within a narrow, near-systemic velocity range. These are best matched by simulations from a model disk with $R_{disk} = 350$ AU and an outer radius of 500 AU. This result strongly suggests that, in this case, infall from the molecular cloud onto a rotating disk is still in progress.

Table of Contents

List of Figures

Chapter 2:

List of Tables

Chapter 3:

CHAPTER 1

Introduction

1. Motivation

Parallel progress in distinct fields of study – the formation of stars and solar system cosmogony – has recently culminated in the birth of a hybrid discipline: the origin of planetary systems. Advances in astronomical techniques, especially increased spatial resolution at long wavelengths, now permit detailed observations of circumstellar matter around newly forming stars. At the same time, space exploration and meteoritic analyses have provided vestigial evidence of early solar system events, while increased high-speed computing ability has aided simulations of key planet-forming processes. The end result of these developments is an increased expectation that planetary systems spontaneously form as an adjunct of star formation.

Although planetary systems may be common, direct detection of planets around a solar-type star other than our own Sun has not yet been achieved. Evidence has continued to accumulate for the existence of disks of dust and gas around very young stars, however (cf. Beckwith & Sargent 1993a). As the existence of such disks has become established, interest has turned to their potential role in forming planetary systems. The property of circumstellar disks with most consequence for planetary system formation is undoubtedly the mass of material available to planet-forming processes. Estimates of circumstellar mass based on models of the Spectral Energy Distribution (SED) of excess long-wavelength emission suggest that sufficient mass exists around at least 50% of all T Tauri stars for the formation of some kind of planetary system (Strom *et al.* 1989; Beckwith *et al.* 1990; André & Montmerle 1994; Henning *et al.* 1994). However, it is unclear in such observations whether this material is *protoplanetary* or *protostellar*. It was once commonly assumed that high-resolution imaging, alone, could decide this issue, since infalling material was expected to exist in a spherical configuration and orbiting material in a plane, but it is now evident, theoretically and observationally, that flattened circumstellar material may be cen-

trifugally unsupported (Galli & Shu 1993; Hayashi *et al.* 1993; Stahler *et al.* 1994). Direct observations of the velocity structure of the circumstellar material, as traced by the distribution of molecular line emission, can discriminate between infalling and orbiting states. It is the aim of this dissertation to determine the kinematic state of circumstellar material in a sample of T Tauri stars and, by implication, the likelihood of extra-solar planet formation.

2. Overview

The main body of this work begins in Chapter 2 with aperture synthesis maps of molecular line emission from the T Tauri star GM Aurigae. A model of a disk in Keplerian rotation is used to simulate the morphology of emission as it appears in maps at distinct velocities. This work has been published in the journal *Icarus* in collaboration with A.I. Sargent and S.V.W. Beckwith and provides compelling evidence for Keplerian rotation of gas in a potentially protoplanetary disk. In Chapter 3, a molecular gas survey of a small sample of T Tauri stars is analyzed for evidence that circumstellar gas resides in centrifugally supported disks. Morphological evidence is considered from aperture synthesis maps of CO($2\rightarrow1$) emission from RY Tauri, DL Tauri, DO Tauri, and AS 209. A preliminary analysis of the velocity structure makes use of first moment velocity maps, spectra, and Position-Velocity Diagrams. A kinematic model of a disk with an infalling and rotating velocity structure follows in Chapter 4, and the corresponding appearance of spectral line maps is investigated for disks with different degrees of centrifugal support. In Chapter 5, this model is used to generate synthetic maps for disks which are then cross-correlated with spectral line images of molecular gas emission from the sample presented in Chapter 3. The central mass, inclination angle and centrifugal radius of the model disk are varied and best-fit values are obtained. Conclusions are discussed as they naturally arise in each chapter. These are summarized in in Chapter 6 and wider implications are discussed.

CHAPTER 2

GM Aurigae

1. Introduction

The existence of circumstellar disks around very young low-mass stars is inferred from their observed spectral energy distributions (SED) at infrared and submillimeter wavelengths (Adams *et al.* 1987; 1988; Strom *et al.* 1989; Beckwith *et al.* 1990, hereafter BSCG; Adams *et al.* 1990). Surveys in the Taurus-Auriga dark cloud indicate that circumstellar disks surround nearly half of all T Tauri stars (Strom *et al.*1989; BSCG). High resolution imaging of a few of these systems, using aperture synthesis techniques, confirms the existence of disk-like morphology (Sargent and Beckwith 1987; 1991; Weintraub *et al.* 1989; Kawabe *et al.* 1993; Koerner *et al.* 1993; Sargent and Beckwith 1993). Disk properties – masses, temperatures, and radii (Beckwith and Sargent 1993a) – are consistent with conditions in the proto-solar nebula (cf. Lin and Papaloizou 1984; Safronov 1991), and in at least one case, HL Tauri, the circumstellar gas appears to move in Keplerian orbits (Sargent and Beckwith 1987; 1991). Since typical T Tauri star ages range from 10^5 to 10^7 years, and masses are between 1 and 3 $M_\odot$, these star-disk systems are analagous to the early solar system, before the formation of planets. Studies of T Tauri stars may therefore provide a means of investigating the early evolution of the proto-solar nebula. In particular, properties of disks around *older* T Tauri stars potentially constrain the dispersal timescales for nebular gas and dust, the critical building material for planets.

Here we present aperture synthesis maps of gas and dust around GM Aurigae, a T Tauri star with mass 0.72-$M_\odot$ and luminosity 0.7-$L_\odot$ (BSCG), in the Taurus–Auriga complex at 140-pc distance (Elias 1978). At 2×10^6 years (BSCG), GM Aur is almost an order of magnitude older than other low mass stars imaged to date (cf. Beckwith and Sargent 1993a; Sargent and Beckwith 1993). Continuum fluxes at infrared and millimeter wavelengths are consistent with the presence of a circumstellar

dust disk of mass at least 0.2-$M_\odot$ (Strom *et al.* 1989; BSCG; Adams *et al.* 1990). However, anomalously low near- to mid-infared emission levels (Rydgren and Vrba 1983) suggest a cleared region in the inner disk extending radially from the star out to several tenths of an AU (Strom *et al.* 1989; BSCG). This inner "clearing," and the fact that GM Aur shows the H_α and X-ray emission typical of young stars (Cohen and Kuhi 1979; Feigelson and DeCampli 1981) but little evidence of the expected energetic mass loss and concomitant accretion associated with very early star formation (cf. Cabrit *et al.* 1991), suggest that this system characterizes a transition phase between active accretion and disk dissipation. Studies of the circumstellar gas and dust around GM Aur may therefore shed light on the transition stage.

2. Observations

Observations of the 1.4 mm continuum and ^{13}CO (2→1) line emission at 220.4 GHz from GM Aur were made between 1990, December and 1991, March, using the Owens Valley millimeter-wave array. Three configurations of three 10.4 m telescopes, with baselines up to 55 m E–W and 80 m N–S, produced a synthesized beam of $3''.5 \times 5''.8$ (FWHM) at PA = 4.4°. Cryogenically-cooled SIS receivers on each telescope produced over-all system temperatures of 500–1000 K. Two filter banks, 32 × 1 MHz and 32 × 50 kHz, centered at v_{hel} = 15.0 km s^{-1}, the radial velocity of GM Aur (Hartmann *et al.* 1986), provided spectral resolutions of 1.3 and 0.07 km s^{-1}. Continuum measurements were made simultaneously in a 375 MHz broad-band channel. The quasar, NRAO150, was observed to calibrate visibility phases; the absolute flux density scale relied on measurements of Uranus and 3C 273. Maps made with the NRAO AIPS software package are centered on the GM Aur position, $\alpha = 04^h51^m59^s.76$, $\delta = 30°17'14''.7$ (Herbig and Bell 1988). Uncertainties in absolute fluxes and positions are estimated to be 15% and $0''.5$, respectively.

3. Continuum Emission

The $\lambda = 1.4$ mm continuum emission at the position of GM Aur is unresolved in our $3''.5 \times 5''.8$ (525 × 870 AU) beam. Peak flux is 181 mJy, consistent with other sub-millimeter measurements (Weintraub *et al.* 1989; BSCG; Adams *et al.* 1990; Beckwith and Sargent 1991). Along the elongation axis of the molecular structure discussed below (PA $\approx 50°$), continuum spatial resolution is $\sim 4''$, implying a 300 AU upper limit to the radius of any dust disk.

The continuum SED for GM Aur, including IRAS fluxes, published sub-millimeter fluxes, and our 1.4-mm flux, is plotted in Figure 2.1. Several authors (Strom *et al.* 1989; BSCG; Adams *et al.* 1990; Beckwith and Sargent 1991; Marsh and Mahoney 1992) have fit disk models to the SED of GM Aur, using independent data sets and adopting different disk inclinations and opacity laws. As a consequence, estimated disk masses range over two orders of magnitude, from 0.013 $M_\odot$ to 1.0 $M_\odot$. Our model fit to the combined data sets is shown as a solid line in Figure 2.1. Following BSCG, effective temperature and density profiles which vary radially as power laws ($T \propto r^{-q}$ and $\Sigma \propto r^{-p}$, respectively) and a mass opacity coefficient which varies as a power law in frequency ($\kappa_\nu \propto \nu^{-\beta}$) are assumed. The effective temperature (as distinct from the mid-plane temperature) at an appropriate reference radius (in this case, 1 AU), and the temperature power-law index, q, are derived from the SED amplitude and slope in the optically thick 25–60 μm region. An inner disk radius, r_0, is obtained from fitting the low 12 μm point. The outer disk radius, R_d, is constrained by fluxes near the SED turnover frequency, ν_d; the model depends very weakly on R_d at all other wavelengths. At sub-millimeter and millimeter wavelengths, continuum emission is likely to be optically thin, and the slope of the SED is very sensitive to the opacity index, β, while amplitude depends on the proportionality constant used for κ_ν and in the total disk mass, M_d (Beckwith and Sargent 1991). The choice of

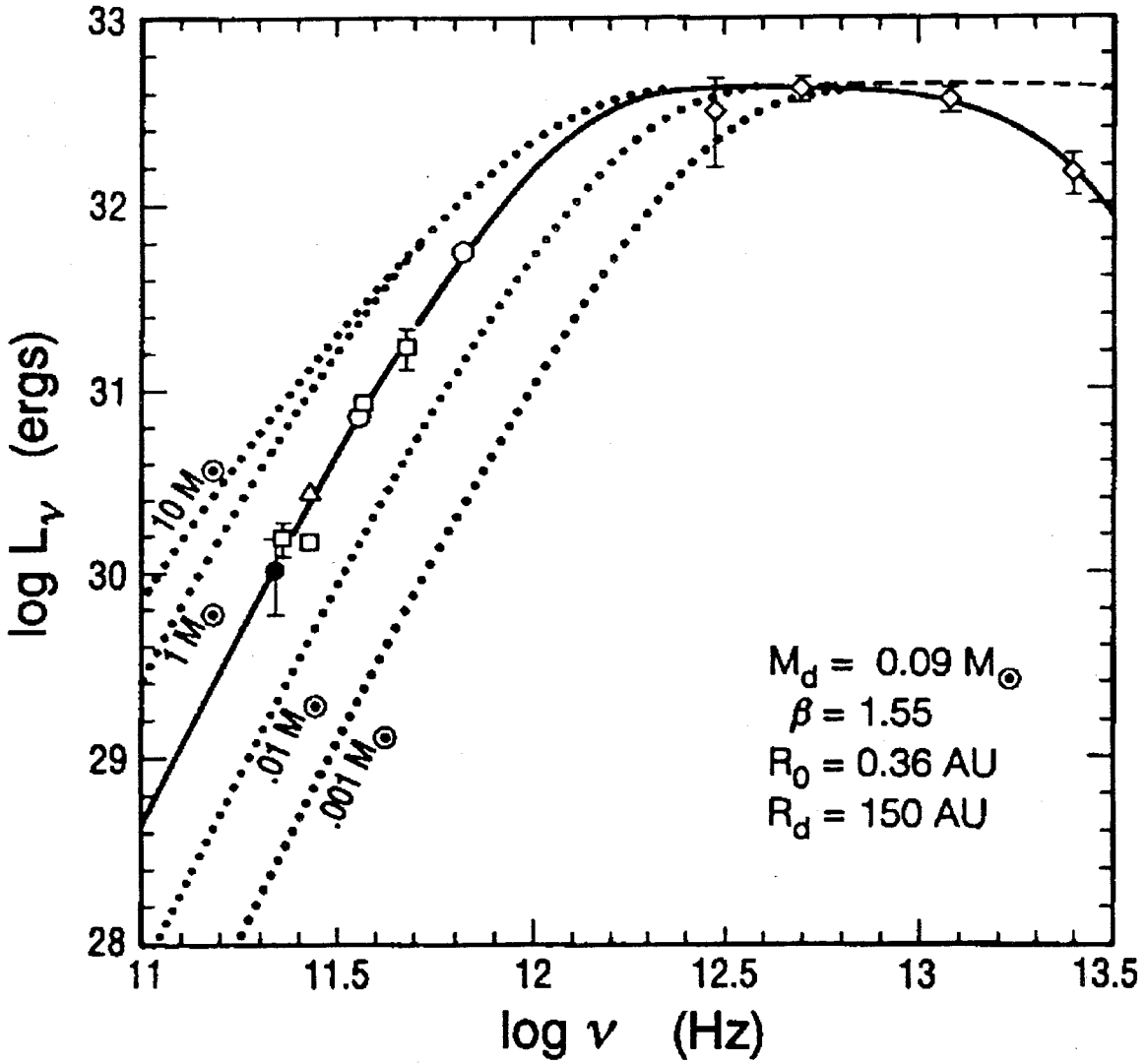

Figure 2.1. The spectral energy distribution of GM Aur. The ordinate is log L_ν, where $L_\nu = \nu F_\nu 4\pi D^2$ ergs. The filled circle is the $\lambda = 1.4$ mm flux from this work. Other flux measurements are represented by squares (Beckwith and Sargent 1991), open circles (Weintraub *et al.* 1989), a triangle (Adams *et al.* 1990), and diamonds (IRAS). Error bars appear only when larger than the symbol. The solid line is the calculated emission from a 0.09-$M_\odot$ disk, inclined at 30°, and with radius 150 AU. Dotted lines illustrate the model dependence on M_d alone; the observed variation changes little for values of β within an acceptable range. An inner gap of 0.36 AU is required to fit the the 12μm and, to some extent, the 25μm IRAS points. The dashed line shows the expected emission from a disk extending from the stellar surface to 150 AU.

inclination angle i (between disk rotational axis and line of sight) has a small effect for $i \leq 80°$. In summary, although the model requires specification of eight parameters (M_d, r_0, R_d, T_0(1AU), q, p, i, and κ_ν), not all of these affect it significantly. Three parameters, q, r_0, and T_0(1AU), are established from the infrared spectral region, while three more, R_d, p and i, have minimal effect. This leaves only two to be determined by a fit to the entire data set, M_d and κ_ν (see BSCG).

The mass opacity coefficient appropriate to circumstellar disks, κ_ν, is not well known and is the principal source of uncertainty in estimates of M_d (Adams *et al.* 1987; BSCG; Beckwith and Sargent 1991). As discussed in BSCG, κ_ν is extrapolated from long wavelength observations of molecular clouds as $\kappa_\nu = 0.1(\nu/10^{12}\mathrm{Hz})^\beta$ cm^2 g^{-1}. No ratio of gas to dust mass is explicitly assumed in these calculations; they rely instead on measurements of the ratio of visual extinction to long-wavelength optical depth, A_V/τ_ν, and assume a ratio of A_V to hydrogen column density similar to that found for the intercloud medium (cf. Hildebrand 1983). As an added check, kinematic modeling of molecular line emission provides an independent constraint on the central mass (star + disk) and, in turn, on κ_ν. Uncertainty in the stellar mass and model-fitting allows for some deviation, but it is sufficiently small to exclude order of magnitude increases in M_d.

For $i \approx 30°$, suggested by models of the molecular line emission (see below), we obtain $r_0 = 0.36$ AU, T_0(1AU) = 167 K, and q = 0.50. These are very similar to the values obtained by BSCG, 0.3 AU, 152 K, and 0.51 respectively, for a face-on disk. As in BSCG, we set the index of the radial density profile, p, to 1.5. Simultaneous fitting of the 450-μm point (near ν_d) and other sub-millimeter data requires $R_d \geq 150$ AU, independent of other parameter choices, but the model is otherwise relatively insensitive to increases in R_d out to 300 AU, our upper limit to the disk size. Using $R_d = 150$ AU, we then derive β and M_d by minimizing χ^2 over an array of values for

β and M_d (as described by Beckwith and Sargent 1991). M_d and β lie within ranges 0.07–0.13 $M_\odot$ and 1.2–1.8, respectively, for χ^2 within $\Delta\chi^2$=1 of its minimum value (~68% confidence level for each parameter estimate); the best-fit parameters are M_d = 0.09 $M_\odot$ and β = 1.55. As we discuss below, $M_d \sim 0.1\ M_\odot$ is consistent with results of kinematic modeling. This is a substantially larger disk mass than derived by Beckwith and Sargent 1991 with few sub-millimeter measurements, but is smaller by an order of magnitude than that of Adams *et al.* 1990 using a lower κ_ν (Draine and Lee 1984; Adams *et al.* 1987). To illustrate the dependence of our model on disk mass alone, the expected SED's for other values of M_d are shown as dotted lines in Figure 2.1.

4. Line Emission

A map of the ^{13}CO(2→1) emission from GM Aurigae, integrated over the 4.1-km s^{-1} width of the three central channels of the 1-MHz filter bank, is shown in Figure 2.2a. No emission above a 2σ level of 400 mJy beam^{-1} is found in channels outside this range, 13.6 $\leq v_{hel} \leq$ 17.7 km s^{-1}. A Gaussian model fit yields a de-convolved source size of 6$''$.8 × 3$''$.8 (950 × 530 AU), elongated along PA = 53°, with flux 9.7 Jy km s^{-1}.

Figure 2.3 displays emission profiles oriented parallel (solid line) and perpendicular (dotted line) to the long axis of the structure seen in Figure 2.2a. Comparison with a profile of the CLEAN beam (dashed line) shows a central unresolved core surrounded by extended emission. The outermost regions of the emission exhibit some irregular morphology. As discussed below, clumps to the NE and SW in Figure 2.2 also have independent velocity signatures.

Emission from the inner disk is likely to be extremely optically thick, sensitive to gas temperature but not column density (cf. Beckwith and Sargent 1993b). However, the brightness temperature of peak emission in the central 1 MHz channel

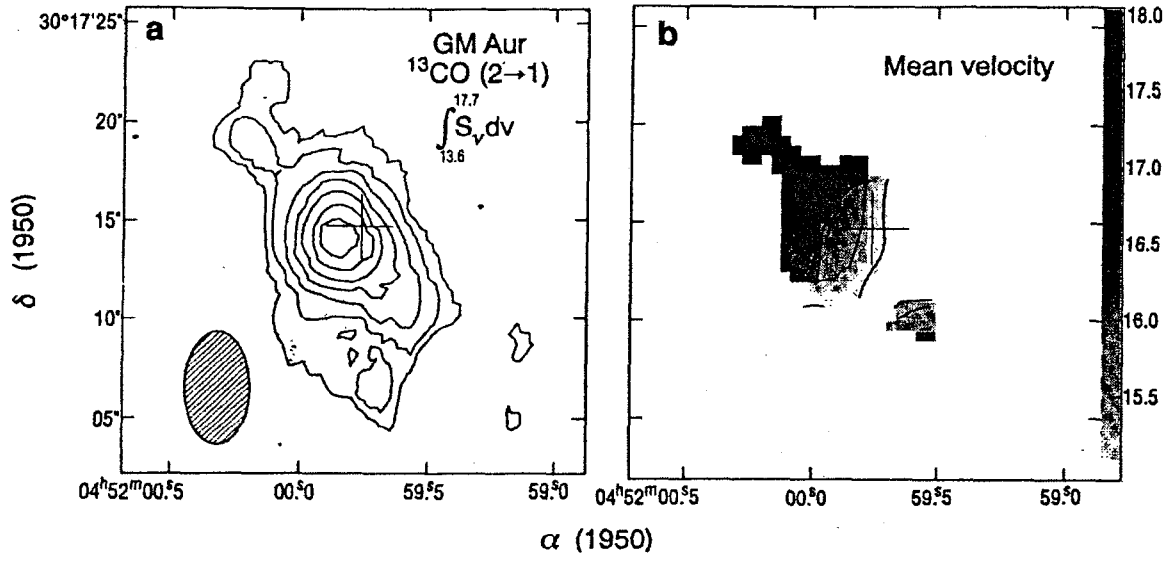

Figure 2.2. a) A map of ^{13}CO (2→1) emission toward GM Aur integrated over the velocity range, v_{hel} = 13.6 to 17.7 km s^{-1}. The contour interval is 0.5 Jy beam^{-1} km s^{-1}, 1σ. Contours start at the 2σ level. Peak emission is 4.5 Jy beam^{-1} km s^{-1}. A cross marks the stellar coordinates of Herbig and Bell 1988. The synthesized beam is displayed as a hatched region. b) A map of the mean velocity variations across the structure seen in a). Grey-scale values correspond to the heliocentric velocity scale on the right. The contour interval is 0.5 km s^{-1}. A gradient is evident along the axis of elongation, at PA ~ 50°.

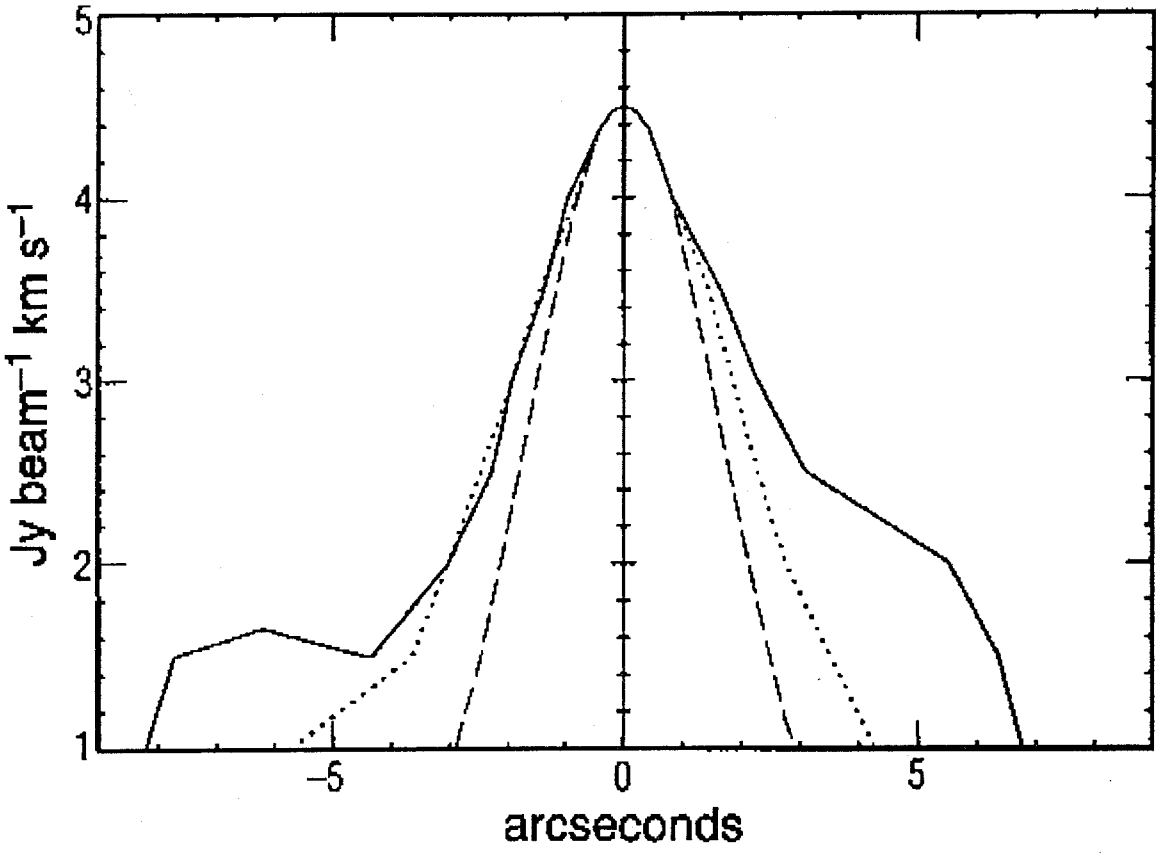

Figure 2.3. Profiles of $^{13}CO(2\rightarrow1)$ line emission (see Fig. 2.2) taken parallel (solid line) and perpendicular (dotted line) to the axis of elongation (PA $\approx 50°$). The CLEAN beam profile, nearly identical along both these directions, is shown as a dashed line with FWHM of 4″.

is only about 6 K. Since this is lower than ambient temperatures in the Taurus cloud, any optically thick region is probably smaller than the beam and limited to the unresolved core evident in Figure 2.3. We can estimate an upper limit to the size of this region by assuming a disk-averaged kinetic temperature, of order a few $\times$ 10 K (Beckwith and Sargent 1993a). This temperature largely reflects conditions near the optically-thick "edge," since the emitting surface area scales as (radius)^2.

For an optically thick source with emission approximated by the Rayleigh-Jeans law, the disk-averaged kinetic temperature, T_k, and the line-center intensity of peak emission, B, are related by:

$$B \times \left(\frac{\Omega_b}{\Omega_s}\right) \approx \frac{2kT_k}{\lambda^2},$$

where Ω_b is the solid angle of the synthesized beam and Ω_s the solid angle subtended by the optically thick source. For a Keplerian disk, the source size of the optically thick region is given by:

$$\Omega_s = \frac{\pi R_d^2}{D^2} \times f(i).$$

Here R_d is the radius of the optically thick region, D the distance to the source, and $f(i)$ is the fraction of circular disk area appearing within the bandwidth. The term, $f(i)$, reflects both a $\cos(i)$ inclination effect and exclusion of disk area with Keplerian line-of-sight velocities outside the bandwidth. Combining these expressions yields:

$$R_d \approx \left[\frac{B\Omega_b D^2 \lambda^2}{2kT_k \pi f(i)}\right]^{1/2}.$$

For D = 140 pc and λ = 1.4 mm with B = 1.6 Jy beam^{-1}:

$$R_d \approx \frac{530}{\sqrt{T_k f(i)}} \mathrm{AU}.$$

For a central 1-$M_\odot$ mass emitting in a 1 MHz (1.36 km s^{-1} at 1.4 mm) bandwidth, $f(i)$ $\sim$ 3/5 and 1/5 at inclinations i = 30° and 60°, respectively. Then T_k = 20 K implies an optically-thick region of radius between 150 and 250 AU. Higher temperatures or a face-on orientation would indicate a somewhat smaller size.

5. Velocity Structure

Figure 2.2b shows a grey scale contoured map of the first-order moment in mean velocity across the central 1 MHz channels. The velocity at the stellar position lies between the 15.0 km s^{-1} and 15.5 km s^{-1} contours, in good agreement with the value 15.0 $\pm$ 1.3 km s^{-1} obtained by Hartmann *et al.* (1986). A distinct gradient is apparent along the axis of elongation. Red-shifted emission to the NE and blue-shifted to the SW are consistent with rotation about an axis oriented at PA $\approx 140°$. Although this velocity structure is not inconsistent with outflow, the narrow range of ^{13}CO velocities, $\pm$ 2 km s^{-1}, and the fact that no high-velocity [OI] or [SII] emission has been detected toward GM Aur (Cabrit *et al.* 1991) argue against this interpretation.

The distribution of $^{13}CO(2\rightarrow1)$ line emission in the 50 kHz filterbank, shown in Figures 2.4a–h also supports the rotational interpretation. If the structure seen in Figure 2.2a is a rotating disk viewed predominantly face-on ($i \approx 30°$), the line-of-sight component of Keplerian velocity will be small, requiring extremely high velocity resolution to adequately sample the disk velocity structure. In Figure 2.4, we have binned the data over velocity ranges that improve the signal-to-noise ratio, but remain narrow enough to preserve distinct characteristics of a rotational pattern. The rapid structure shift observed across the maps at 0.1-km s^{-1} resolution suggests that any disk associated with GM Aur is oriented with a small angle between its rotational axis and the line of sight.

The mean velocities associated with the NE and SW clump in Figure 2.2 are inconsistent with Keplerian rotation; the NE clump is more highly red-shifted than nearby gas, while the SW clump appears to have a retrograde mean velocity. This is also reflected in Figures 2.4a, b and g, where the rotational pattern is disrupted in the vicinity of the clumps. We return to this question below.

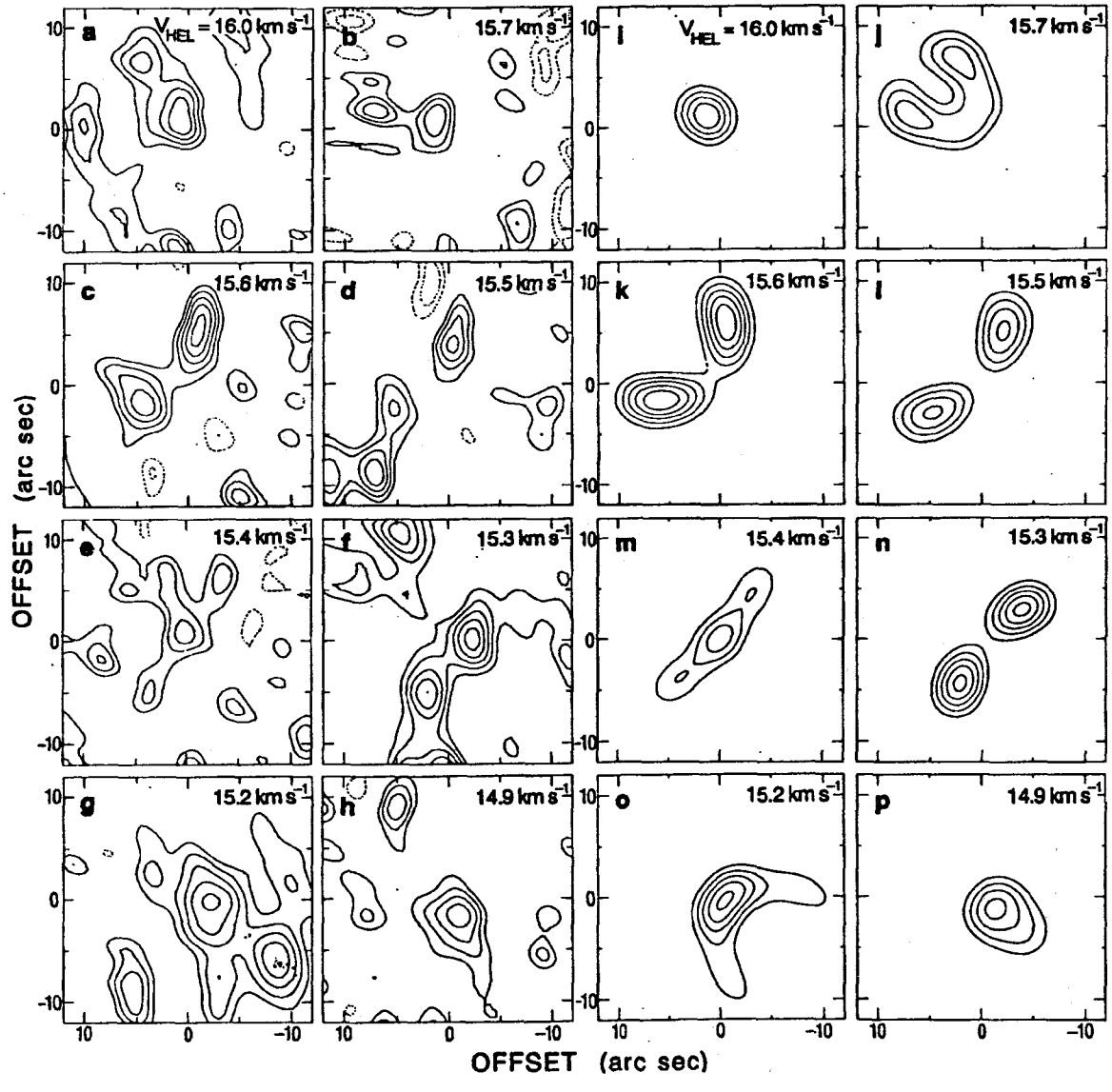

Figure 2.4. Aperture synthesis maps of GM Aur at ~0.1-km s^{-1} velocity resolution. Most are averaged over bandwidth 0.14-km s^{-1}; high SNR in 3 of the 4 central channels permitted 0.07-km s^{-1}. The contour interval in each map is at the 1σ level; this varies from map to map but is typically ~1 Jy; contours start at 2σ. i–p) Synthetic maps produced by a model Keplerian disk (see text), inclined 30° from face on, with 0.8-$M_{\odot}$ central mass and referenced to a line-center velocity of 15.38 km s^{-1}. Velocity widths correspond to those in Figures 2.3a–h.

6. Kinematic Modeling

Synthetic maps, shown in Figures 2.4i–p, were generated from a parametrized disk radial emissivity profile, ϵ(r). The disk was gridded in Cartesian coordinates and, following Sargent and Beckwith 1987, Keplerian line-of-sight velocities for an edge-on disk were assigned to grid points. The disk-intensity pattern was inclined and rotated, and new line-of-sight velocity components were calculated, multiplying by $\sin(i)$, where the inclination angle, i, is measured between disk-plane normal and line of sight. Disk emission was then excluded for all grid points with line-of-sight velocities outside the bandwidth of the modeled channel map. The final image resolution was degraded to that of aperture synthesis maps by convolution with a Gaussian "beam."

The disk emissivity profile, ϵ(r), was constructed to approximate an optically thick inner core plus an extended optically thin disk. This form was chosen simply to reproduce emission intensity on a particular sector of the disk; line-of-sight velocities entirely determine which sector appears in a given channel. Unknown optical depth, insufficient spatial resolution, and narrow-band noise preclude detailed inference of physical properties, such as T(r) or Σ(r), from fitting of the emissivity profile. Parameters derived below from kinematic modeling, however, have negligible dependence on $\epsilon(r)$. The rate of pattern variation from channel to channel depends on the intrinsic Keplerian velocity, $\sqrt{GM/r}$, and its component along the line of sight, $\propto \sin(i)$. The pattern outline is sensitive to i, providing an additional constraint; $\epsilon(r)$ determines only the brightness distribution within it.

To approximate the observed brightness distribution, two radial Gaussian functions were combined in the form

$$\epsilon(r) = A_1 e^{-(r/\sigma_1)^2} + A_2 e^{-(r/\sigma_2)^2},$$

where A_j are amplitudes of the core and outer disk with associated halfwidths, $B(\sigma_j)$

$= \sigma_j\sqrt{ln2}$. Models were run, gridding over inclination angle i, position angle PA, and central mass M as free parameters; i and PA were gridded in increments of 10°, and M, in increments of 0.1 $M_\odot$. The observed brightness distribution was approximated by $\epsilon(r)$ with halfwidths $B_1 = 100$ AU and $B_2 = 1100$ AU for the inner core and outer disk, respectively, and with amplitude ratios A_1:A_2 of ~10:1. As discussed below, emission disrupted by the NE and SW clumps (Figure 2.4b and g), was modeled with $B_1 = 200$ in Figure 2.4j and with $B_1 = 200$, $B_2 = 1500$, and A_1:$A_2 \sim$ 30:1 in Figure 2.4o.

Synthetic maps from the range of models described above were compared to the observed by simple inspection. Criteria for a good "fit" required that model maps simultaneously approximate emission morphology in Figures 2.4c-f and that emission from the central disk become compact near the stellar position at velocities corresponding to Figure 2.4a and h. The first condition, though also affected by M, predominantly constrains i. The intensity pattern of an edge-on disk ($i = 90°$) lies along a line and is distributed in channel maps throughout a range of velocities encompassing tangential Keplerian motion from detectable fractions of the disk emission. Relative to the smaller-i case, emission appears in a maximum number of narrow-band channel maps with minimum size per map and little variation between adjacent channel maps; morphology is either point-like or linear along the axis of elongation. Radiation from a nearly face-on disk (i close to 0°), on the other hand, is more nearly confined to the natural line width (thermal or turbulent), since tangential rotational motion is no longer directly along the line of sight. In spectral line maps, it emanates from sectors of an elliptical region with eccentricity $\propto i$ and is divided among fewer channel maps with greater map-to-map variation as i decreases; the morphology of line-center emission is linearly extended perpendicular to the major axis of the ellipse (see Figures 2.4e and 2.4f). The eccentricity of the emitting elliptical region (hence

i) is most easily observed in the central channels. The second requirement further constrains the central mass, M, since Keplerian velocity is proportional to its square root; as M gets large, the velocity at which the inner (highest velocity) portions of the disk appear unresolved is increasingly distant from line center.

To match the structure observed in Figures 2.4a–h with the above model requires $i = 30° \pm 10°$ about PA $= 50° \pm 10°$ with $M = 0.8 \pm 0.1\ M_\odot$ and systemic velocity $v_{\rm hel} = 15.38 \pm .05$ km s^{-1}. Uncertainties represent the coarse parameter grid interval. Parameter values more than one grid interval away produced synthetic maps which clearly could not meet the above criteria for comparison with Figures 2.4a, c–f, and h.

Emission in Figures 2.4b and g deviates noticeably from the model. In both figures, the emission in the modeled sector of the outer disk is reduced relative to the inner core. Some approximation of this effect has been achieved in Figures 2.4j and o by varying $\epsilon(r)$ to match the brightness pattern on the Keplerian sector defined by the above model parameters. Emission is also present outside this sector in Figure 2.4a and h and at the position of the NE and SW clumps seen in Figure 2.2. These gaseous condensations are unresolved; observations at higher spatial resolution may be required to understand their morphology and kinematics within the context of a large disk. Nevertheless, we note that fragmentation of collapsing gas, either before or after disk formation, is an outcome of many numerical simulations (cf. Bodenheimer *et al.* 1993).

As an additional test, the values $i = 30°$, PA $= 50°$, $M = 0.8\ M_\odot$, and $v_{\rm rad} = 15.38$ km s^{-1} with $\epsilon(r)$ as in Figures 2.4i, k-n, and p were used to construct models of the emission in the 1-MHz channels contributing to Figure 2.2. Velocity resolution, 1.4 km s^{-1}, is much lower, but higher-velocity gas is imaged in the outer two channels, probing the inner disk more effectively. Expected model emission is

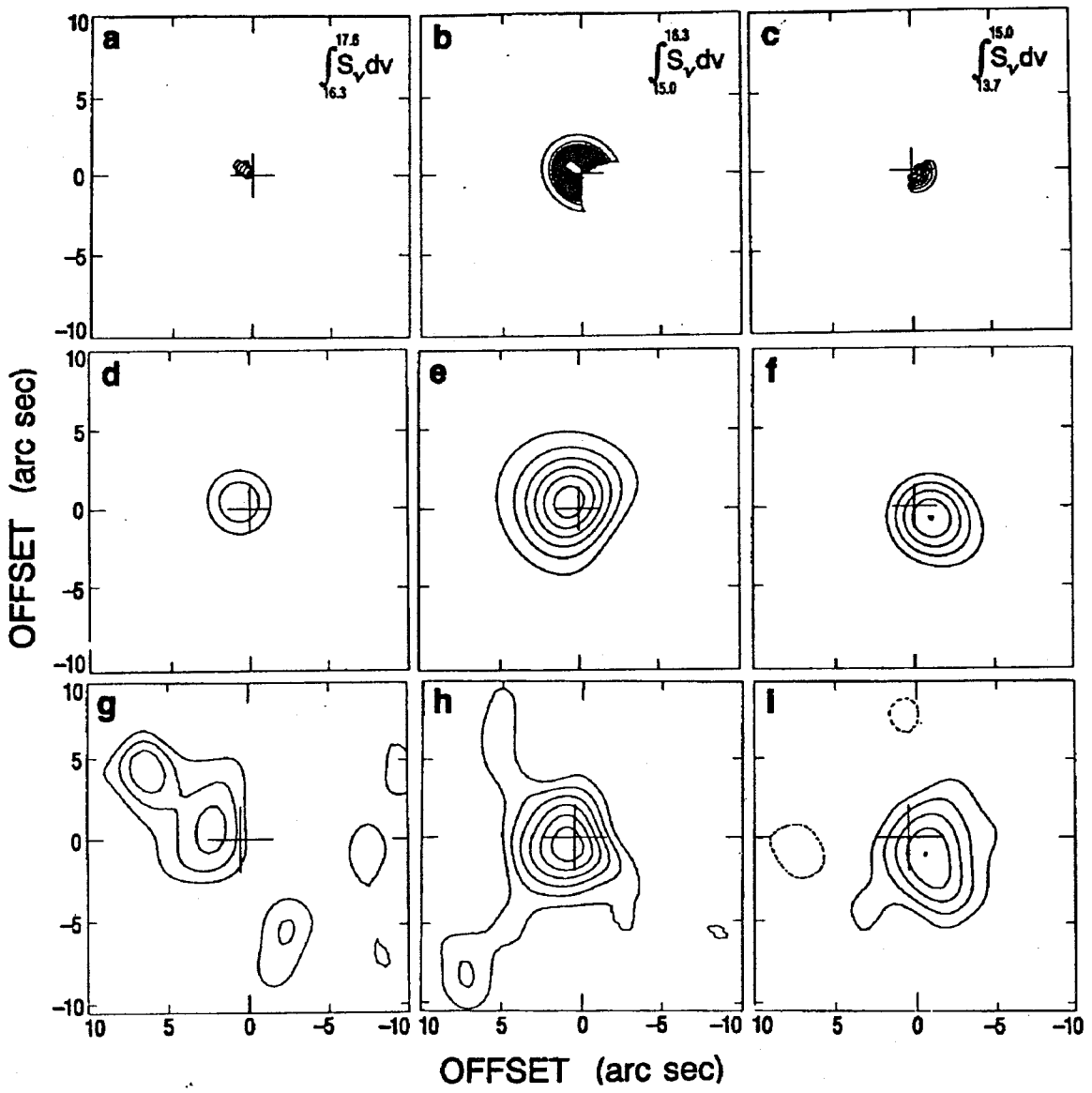

Figure 2.5. a–c) The same model molecular disk used for Figure 2.3, as it would appear unconvolved in velocity bands corresponding to the central 1-MHz channels that gave rise to Figure 2.2a. The disk areas shown have line-of-sight, Keplerian, velocity components that fall within the channel width. A cross marks the model center. d–f) The same disk as above, convolved with a Gaussian "beam" to match the spatial resolution in our aperture synthesis maps. Contours again start at 2σ and are separated by 1σ (200 mJy). g–i) Aperture synthesis maps of GM Aurigae at 1.3 km s^{-1} resolution centered at v_{hel} = 17.0, 15.7, and 14.4 km s^{-1}, respectively (from left to right).

shown unconvolved in Figures 2.5a-c and convolved in Figures 2.5d-f. Comparison with individual channel maps, shown in Figures 2.5g-i, strongly supports the existence of a rotating disk. Though emission is largely unresolved, peak positions are aligned in similar relative positions and with similar relative flux levels.

Figures 2.4 and 2.5 show good agreement between observed and modeled emission morphology, using the same values for disk orientation, central mass, and radial velocity. The stellar mass of 0.72 $M_\odot$ (BSCG) and our estimate of the total central mass M, 0.8±0.1 $M_\odot$, lead to an inner disk mass, $M_d \sim 0.1\ M_\odot$. Due to uncertainties in both stellar and central masses, M_d may be larger by a factor of 3, while no lower limit can be obtained from the kinematic modeling alone. Nevertheless, model comparison rules out a compact 1 $M_\odot$ disk and concomitantly low κ_ν (Adams *et al.* 1990) and establishes the rotation of gas around GM Aur out to many hundreds of AU in a self-consistent way.

7. Discussion

Our aperture synthesis maps, together with kinematic modeling, provide compelling evidence for a rotating disk around GM Aurigae. Integrated ^{13}CO(2→1) line emission, 530 AU × 950 AU in extent, indicates an optically-thick core with radius between approximately 150 and 250 AU. There is a velocity gradient, consistent with rotation, along the elongation axis at PA ≈ 50°. Spectral line maps at high velocity resolution ($\sim$ 0.1 km s^{-1}) reveal the velocity structure in detail; the morphology is reproduced by a single model of a disk, inclined at 30°, in Keplerian motion about a 0.80-$M_\odot$ central mass with systemic velocity, $v_{\rm hel}$ = 15.38 km s^{-1}, and lead to $M_d \sim$ 0.1 $M_\odot$ for the mass of the inner disk. Modeling of emission in 3 broad-band channels probes higher velocities associated with the inner disk and confirms the fitted parameters. In addition, compact dust emission possesses spectral energy characteristics which are well modeled by a 150-AU disk, similar in size to the optically-thick

molecular disk. Its mass, $M_d \approx 0.09\ M_\odot$, agrees remarkably well with that obtained from kinematic analyses.

A timescale for dust dispersal, 0.3–1.0 $\times$ 10^7 years, and an inverse correlation between near- to mid-infrared flux and T-Tauri stellar age (Strom *et al.* 1990; Skrutskie *et al.* 1991) has been inferred from infrared surveys. Since there is no similar correlation at millimeter wavelengths which sample the cold, outer disk, these timescales may apply only to clearing of the inner regions (Beckwith and Sargent 1991). In the case of GM Aur's anomalously low mid-infrared flux, it is implicitly assumed that any "clearing" interpretation reflects depletion of small dust particles in the inner regions (cf. Beckwith and Sargent 1993a), perhaps by coagulation into particles larger than 10 μm. The observed low values of the 12 μm flux may, however, result from an optically-thin residual shell (Mathieu *et al.* 1991) or combined effects of dust grain opacity and vertical disk structure (Boss and Yorke 1993). Opening of an actual gap could also be affected by dynamical interaction with planetesimals, protoplanets, or a low-mass stellar companion (Mathieu *et al.* 1991). Limits on radial velocity variations for GM Aur argue against a stellar mass companion within the gap radius (0.36 AU), but do not exclude a brown dwarf or protoplanet (Mathieu, private communication).

With mass nearly an order of magnitude larger than required for a "minimum mass" solar nebula (0.01 $M_\odot$) (Weidenshilling 1977), a dense inner region with radius $\sim$150 AU, and compelling evidence for Keplerian rotation, GM Aur may well represent a protoplanetary system disk. At 2 $\times$ 10^6 years, GM Aur is the oldest T Tauri star for which a gaseous disk has been imaged. Stellar age, low stellar extinction, cessation of observable outflow, and possible clearing of inner dust imply that the disk is relatively evolved. This is the first direct evidence of a significant gaseous disk in such an object, and therefore provides an important constraint on dust and gas

survival times in potentially planet-forming disks. Single-telescope surveys of more-evolved ($\sim 10^8$ years) young stars have failed to detect circumstellar molecular line emission (Skrutskie *et al.* 1991; Yamashita *et al.* 1993). Our result demonstrates that further interferometric observations, with higher sensitivity to small-scale gas, are necessary to better constrain gas persistence timescales.

The millimeter-wave observations presented here presage a burgeoning era of protoplanetary research, as sensitivity and spatial resolution of millimeter interferometers increases. Searches for gas in older T Tauri stars will address in greater detail the question of timescales for disk dispersal in the outer solar nebula. Future interferometric observations of GM Aur and similar systems, in several molecular lines and at higher spatial resolution, will constrain radial temperature, density, and chemical profiles in the disk. These are fundamental to any accurate reconstruction of the details of planetary cosmogony, both in the proto-solar nebula and the wider context of other possible planetary systems.

CHAPTER 3

A Survey of T Tauri Stars for Circumstellar Gas

1. Background and Motivation

The small fraction of T Tauri stars for which circumstellar molecular gas has been detected stands in marked contrast to the 50% detection rate achieved by continuum surveys (Strom *et al.* 1989; Beckwith *et al.* 1990; André & Montmerle 1994). This largely reflects the fact that single telescope observations of compact circumstellar radiation are more sensitive to broad-band dust continuum emission than to radiation from molecular transitions. Beam dilution and ambient cloud confusion also make it extremely difficult to identify circumstellar molecular line emission unambiguously. Molecular line millimeter-wave interferometry provides the needed sensitivity to detect circumstellar gas on small spatial scales while resolving out large-scale ambient cloud emission. Until recently, however, available millimeter arrays have comprised only three elements. As a result, a single map requires multiple telescope configurations and a large amount of observing time compared to single telescopes.

Circumstellar molecular line emission from a T Tauri star was first detected in aperture synthesis images of circumstellar gas around HL Tauri obtained with the Owens Valley millimeter array (Beckwith *et al.* 1986; Sargent & Beckwith 1987). CO line emission was sufficiently bright in spectral line maps to suggest that circumstellar gas around other T Tauri stars would also be easily detectable. Aperture synthesis maps of T Tauri (Weintraub *et al.* 1987), DG Tauri (Sargent & Beckwith 1989; Ohashi *et al.* 1991), and GG Tauri (Kawabe *et al.* 1993; Koerner *et al.* 1993) confirmed this expectation. Nevertheless, a recent survey with the Owens Valley millimeter array for $^{13}CO(1 \rightarrow 0)$ emission from the T Tauri stars DL Tau, RY Tau, DR Tau, CI Tau, and UZ Tau yielded no detections with limiting fluxes of a few 100 mJy bm^{-1} km s^{-1} obtained in integration times of a few hours (Koerner & Sargent 1994). This result was surprising since these objects exhibit the strong 1.3 mm continuum emission diagnostic of disks (Beckwith *et al.* 1990; Beckwith & Sargent 1993a) and

should be easily detected if their gas to dust ratio is consistent with cosmic levels. Early observations of HL Tau, T Tau, and GG Tau suggested this should nearly be the case, but studies of these objects at other wavelengths indicate they may not be representative of most T Tauri stars. Hubble Space Telescope observations of HL Tau reveal that it is, in fact, an embedded object (Stapelfeldt *et al.* 1994, in preparation.). The Spectral Energy Distribution (SED) of T Tau indicates it would appear as an embedded object from most viewing angles (Kenyon *et al.* 1993a, Calvet & Hartmann 1994), and GG Tau is an unusual hierarchical quadruple star system possessing a large distorted circumbinary disk around one of the close binary pairs (Ghez *et al.* 1993; Koerner *et al.* 1993; Dutrey *et al.* 1994).

The detection of ^{13}CO($2\rightarrow1$) emission at 1.3 mm from GM Aurigae (Chapter 2) was perhaps the first demonstration of the presence of gravitationally bound molecular gas around a more representative T Tauri star. This result confirmed calculations indicating that circumstellar disk emission in the CO ($2\rightarrow1$) transition should be markedly stronger than in the CO ($1\rightarrow0$) line. For disks which are optically thin in both CO($1\rightarrow0$) and CO($2\rightarrow1$) emission, the ratio of brightness temperatures in the respective transitions is proportional to the product of the molecular level populations, n_l, and the integrated cross section, σ_0 (Beckwith & Sargent 1993b). Since CO should be thermalized at the densities and temperatures expected in disks, n_l, the number per unit volume of molecules in the upper level, is given by the Boltzmann formula:

$$n_l = \frac{g_l e^{-\frac{E_l}{kT}}}{Z(T)} f \frac{\rho}{m_0},$$

where g_l is the statistical weight, E_l the level energy, $Z(T)$ the partition function, f the fractional abundance, ρ the mass density, and m_0 the molecular mass. To derive the ratio of expected brightness temperatures, it is only necessary to consider terms with an explicit dependence on the transition. For the rotational levels of CO, these

are

$$g_J = 2J+1 \ , \quad E_J = J(J+1)kT_l/2 \ ,$$
$$\text{and} \quad \sigma_0 = \frac{8\pi^3 kT_l}{h^2 c}\frac{(J+1)^2}{2J+1}\mu^2 \ ,$$

where J is the lower level, T_l is the temperature equivalent, and μ the dipole moment of the transition. Combining these expressions and solving for the brightness temperature ratio, it can readily be seen that optically thin disks should be a factor of 6 brighter in the $(2\rightarrow 1)$ transition than in the $(1\rightarrow 0)$ line, assuming disk-averaged temperatures in the range 30–60 K.

The expected brightness enhancement at $\lambda = 1$ mm and the detection of ^{13}CO $(2\rightarrow 1)$ emission from GM Aur encouraged a renewed search for circumstellar molecular line emission from T Tauri stars. Further impetus was provided by the expansion of the Owens Valley Millimeter Array to five elements, decreasing the time required to acquire an image. Highly sensitive, 3″-resolution mapping is now possible in a single configuration. This work marks a beginning in which the number of T Tauri stars imaged in molecular line emission has been doubled.

2. Observations

The T Tauri stars chosen for observation are among the strongest sources of millimeter continuum emission in the nearest star-forming regions. The 1.3 mm continuum survey of Beckwith *et al.* (1990) with the IRAM 30 m telescope provided target sources in the Taurus-Aurigae dark cloud: RY Tauri, DL Tauri, and DO Tauri. The other source, AS 209, was selected from a similar survey of the ρ Ophiuchi dark cloud by André & Montmerle (1994). These clouds are located at distances of 140 pc and 160 pc, respectively (Elias 1978; Whittet 1974; de Geus *et al.* 1990). The sample is listed in Table 3.1 together with coordinates from the catalog of Herbig & Bell

Table 3.1. Star Properties.

(1) Source	(2) α (1950)	(3) δ (1950)	(4) $F_{1.3mm}$ (mJy)	(5) α_{IR} (2.2-12μm)	(6) M_* ($M_\odot$)	(7) Age ($\times 10^6$ yr)
RY Tauri	04:18:50.80	+28 19 35.0	229[a]	0.05	1.69[a]	0.21[a]
DL Tauri	04:30:36.02	+25 14 24.0	230[a]	–0.37	0.56[a]	1.20[a]
DO Tauri	04:35:24.18	+26 04 55.2	136[a]	–0.33	0.72[a]	0.60[a]
AS 209	16:46:25.24	–14 16 56.5	300[b]	–0.60	—	—

a) Beckwith *et al.* (1990)
b) André & Montmerle (1994)

(1988) and stellar properties of importance to the interpretation of the kinematics of circumstellar gas. The spectral index, $\alpha_{2.2-12\mu}$, was derived from published K-band magnitudes (Cohen & Kuhi 1979; Ghez 1993) and the IRAS flux at 12 μm (Weaver & Jones 1992). Stellar masses and ages are included from published work when available (Beckwith *et al.* 1990).

Observations of 1.3 mm continuum and CO (2→1) line emission at 230.5 GHz from RY Tau, DO Tau, DL Tau, and AS209 were made between 1993, November, and 1994, March, using the Owens Valley millimeter-wave array. A single configuration of five 10.4 m telescopes, with baselines up to 60 m E–W and 60 m N–S, provided an approximately circular 3″ beam. RY Tau and DL Tau were also observed in a more extended configuration with baselines up to 100 m E–W and N–S, yielding spatial resolution of up to 2″ for RY Tau. Cryogenically-cooled SIS receivers on each telescope produced over-all system temperatures of 500–1000 K. The spectrometer of the digital correlator was configured with two bands of Hanning smoothed channels with widths 32 × 1 MHz and 96 × 83 kHz, centered on the CO(2→1) line at the velocities, $V_{LSR} \sim$

6.0–7.5 km s^{-1} for the Taurus sources (Hartmann *et al.* 1986), and $V_{HEL} = -4.0$ km s^{-1} for AS 209 (F.M. Walters, private communication). Spectral resolutions are 1.30 and 0.11 km s^{-1}, respectively, for each band. Continuum measurements were made simultaneously in a broad-band channel of width 1 GHz. The quasar, 0528+134, was observed at 20-minute intervals to calibrate visibility phases for DO, DL, and RY Tau; NRAO 530 was used for AS209. The absolute flux density scale relied on measurements of Uranus and 3C 273. Maps made with the NRAO AIPS software package are centered on the positions in Table 3.1. Uncertainties in absolute fluxes and positions are estimated to be 15% and 0″.5, respectively, for map intensities greater than 10σ, but may as great as 50% and 3″ for features detected at lower levels.

3. Analysis of Molecular Line Observations

For each source, maps of the integrated CO(2→1) emission are displayed in Figures 3.1–3.4. For RY Tau and DL Tau, emission is integrated over the velocity range for which emission appeared above a 2σ level of 300 mJy $beam^{-1}$ in maps with velocity width 0.45 km s^{-1}. The linewidths for AS 209 and DO Tau exceeded the range covered by the high-velocity-resolution band; emission was integrated over the wider 1.30 km s^{-1} channels in which peak map intensity was above a 2σ level of 50 mJy $beam^{-1}$. Individual linewidths are listed in column (2) of Table 3.2.

3.1 Morphology and Orientation of Circumstellar Gas

As a first approximation, an elliptical Gaussian was fit to the emission in the aperture synthesis maps and deconvolved with the restoring beams used in the CLEAN deconvolution process, to determine the radial extent of the circumstellar gas. The radius at half-maximum intensity, R_{HM}, given in column (3) of Table 3.2 is derived from the FWHM major axis of this Gaussian fit. Since expected power-law profiles in temperature result in drastically reduced emission from the outer regions

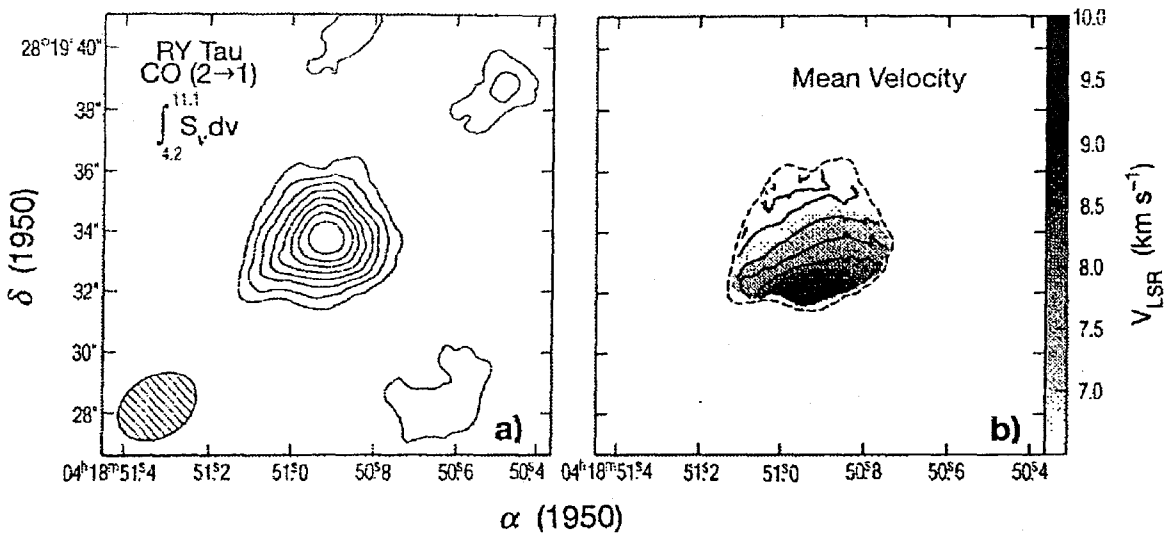

Figure 3.1. a) A map of CO(2→1) emission toward RY Tau integrated over the velocity range, V_{lsr} = 4.2 to 11.1 km s^{-1}. The contour interval is 400 mJy beam^{-1} km s^{-1} (1σ). Contours start at the 2σ level. Peak emission is 3.9 Jy beam^{-1} km s^{-1} with an integrated intensity of 7.3 Jy beam^{-1} km s^{-1} . The synthesized beam, 2″.6 × 1″.9 FWHM at PA -54.27°, is displayed as a hatched region. The apparent elongation to the SE is largely a beam effect. The FWHM deconvolved size of a Gaussian fit to the emission is 2″.3 × 1″.9 oriented at PA 48.6°, but this value is highly uncertain as an indicator of source size and orientation, since it is of order the beam size. b) A map of the mean velocity variations across the structure seen in a). Grey-scale values correspond to the velocity scale shown to the right. The contour interval is 0.5 km s^{-1}. A systematic velocity gradient is evident along the axis of elongation. At the position of peak emission, the gradient is directed along PA ∼ 21°.

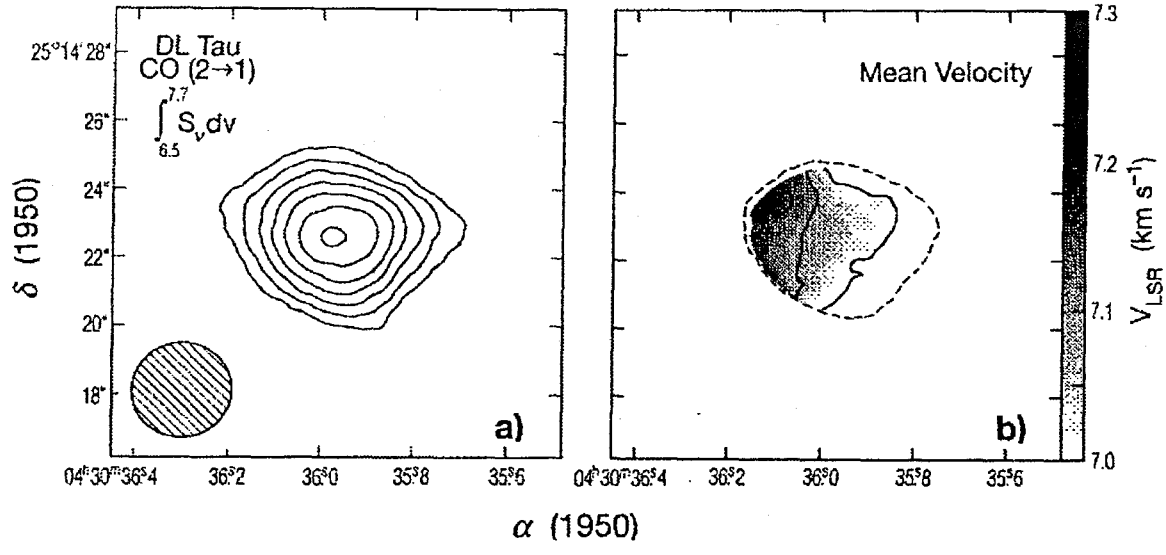

Figure 3.2. a) A map of CO(2→1) emission toward DL Tau integrated over the velocity range, V_{lsr} = 6.5 to 7.7 km s^{-1}. The contour interval is 73 mJy beam^{-1} km s^{-1} (1σ). Contours start at the 2σ level. Peak emission is 594 mJy beam^{-1} km s^{-1} with an integrated intensity of 1.1 Jy beam^{-1} km s^{-1}. The synthesized beam, 2″.9 × 2″.8 at PA −85°, is displayed as a hatched region. The FWHM deconvolved size of a Gaussian fit to the emission is 3″.5 × 2″.5 oriented at PA 84°, b) A map of the mean velocity variations across the structure seen in Figure 2a. Grey-scale values correspond to the velocity scale at the top. The contour interval is 0.1 km s^{-1}. A gradient is evident along the axis of elongation, at PA ∼85°.

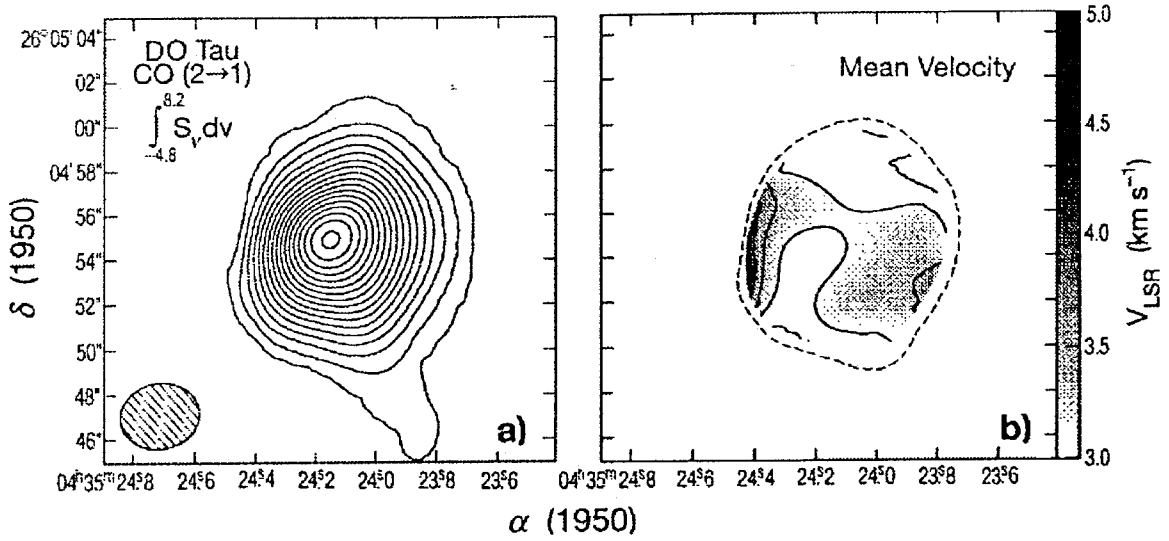

Figure 3.3. a) A map of CO(2→1) emission toward DO Tau integrated over the velocity range, V_{lsr} = -4.8. to 8.2 km s^{-1}. The contour interval is 2.0 Jy beam^{-1} km s^{-1} (2σ). Contours start at the 2σ level. Peak emission is 34.5 Jy beam^{-1} km s^{-1} with an integrated intensity of 100.2 Jy beam^{-1} km s^{-1} . The synthesized beam, $3''.2 \times 2''.9$ FWHM at PA -54.27°, is displayed as a hatched region. The FWHM deconvolved size of a Gaussian fit to the emission is $5''.1 \times 3''.9$ oriented at PA 160°. The aspect ratio of the major and minor axes implies an inclination angle of 40° for a circularly symmetric disk. b) A map of the mean velocity variations across the structure seen in a). Grey-scale values correspond to the velocity scale shown to the right. The contour interval is 0.5 km s^{-1}. A systematic velocity gradient is not easily identified. This may reflect a combination of kinematic effects, such as infall, rotation, and outflow.

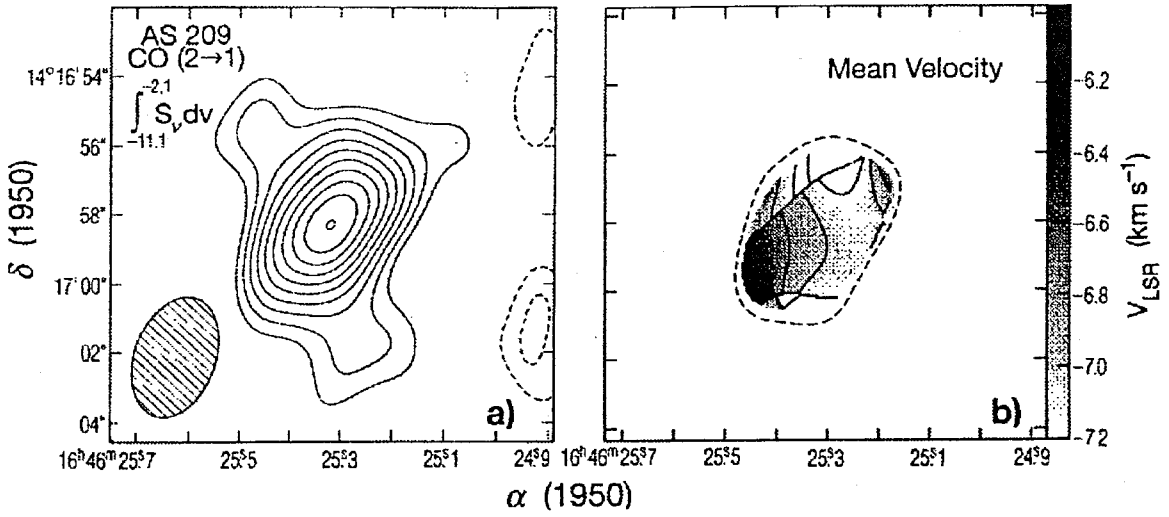

Figure 3.4. a) A map of CO(2→1) emission toward AS 209 integrated over the velocity range, V_{hel} = -11.1 to -2.1 km s^{-1}. The contour interval is 350 mJy beam^{-1} km s^{-1}, 1σ. Contours start at the 2σ level. Peak emission is 3.9 Jy beam^{-1} km s^{-1} with an integrated intensity of 7.4 Jy beam^{-1} km s^{-1} . The synthesized beam, 3″.6 × 2″.3 FWHM at PA -18.6°, is displayed as a hatched region. The FWHM deconvolved size of a Gaussian fit to the emission is 3″.1 × 2″.2 oriented at PA 137.9°. Low level contours are also elongated nearly perpendicular to this axis, as might be expected for CO entrained in an outflow. b) A map of the mean velocity variations across the structure seen in a). Grey-scale values correspond to the velocity scale shown to the right. The contour interval is 0.25 km s^{-1}. There is some indication of a velocity gradient along the CO elongation axis. Deviations from this trend may be due to outflow or infall components.

Table 3.2. Global Properties Derived from CO Emission

(1) Source	(2) ΔV (km/s)	(3) R_{HM} (AU)	(4) $R_{\tau>1}$ (AU)	(5) $\int S_\nu dv$ (Jy/bm km/s)	(6) M_{H_2} ($\times 10^{-6}\ M_\odot$)
RY Tauri	6.9	107	52	6.6	9.6
DL Tauri	1.2	250	53	0.9	1.3
DO Tauri	13.6	350	164	100.2	145
AS 209	10.4	287	115	7.4	10.7

of disks, R_{HW} is only a *lower limit* to the full radial extent of CO. Figures 3.1–3.4 and Table 3.2 demonstrate that all of the sources are resolved in ~2-3″ beams, with values of R_{HM} in the range 100 AU $\lesssim R_{HM} \lesssim$ 400 AU. These dimensions are more like the early solar nebula and are approximately an order of magnitude less than observed in previous aperture synthesis maps of T Tauri stars. This result furthers the contention above that the first objects mapped may not have been typical of T Tauri stars as a whole.

The orientation of circumstellar gas must be determined before a kinematic analysis can be carried out. Emission is preferentially elongated along one axis in all sources in Figures 3.1–4, implying a flattened structure. However, the degree of elongation is uncertain, given the size of some objects relative to the spatial resolution. The P.A. of the projection on the sky of an axis about which the plane of material is inclined (given, for example, by the elongation axis of an inclined disk) must be identified. Equivalently, the P.A. of the sky-projected axis normal to the disk plane (*e.g.*, the orientation of an associated optical jet) can be used. In Table 3.3, the P.A. of CO emission elongation, Θ_{CO}, determined from the Gaussian fit, is listed for each of the sources. Source features that cause the gas to appear extended in a direction

Table 3.3. Diagnostics of Disk Orientation.

(1) Source	(2) Θ_{CO}	(3) $\Theta_{\delta V}$	(4) Θ_{pol}	(5) $\Theta_{jet} + 90°$
RY Tauri	$48° \pm 5°$	21°	$20° \pm 20°_a$	—
DL Tauri	$84° \pm 5°$	84°	$85° \pm 7°_b$	—
DO Tauri	$160° \pm 5°$	—	$170° \pm 1°_a$	$160°_c$
AS 209	$138° \pm 2°$	120°	$134° \pm 10°_a$	—

a) Bastien (1982)
b) Tamura & Sato (1989)
c) Hirth *et al.* (1994)

other than that due to a planar orientation of material can confuse the determination of elongation orientation. These features include azimuthal asymmetries, molecular outflows, or ambient cloud material and, with limited spatial resolution, render it difficult to identify the true morphology and orientation of circumstellar CO gas on the basis of the CO images alone. Independent constraints on the structure of the circumstellar material must be found.

The spatial distribution of the intensity-weighted average velocity ("first moment" with respect to velocity) may provide circumstantial evidence about disk orientation, if systematic velocity gradients are apparent. Maps of the first moment in velocity for the sample sources are shown in Figures 3.1b–4b. To a first approximation, rotation in a flattened disk will appear as a gradient in mean velocity parallel to the elongation axis of the disk. Outflow, or pure infall in the plane of a flattened envelope, on the other hand, will result in a gradient orthogonal to this direction. Thus, the velocity gradient alone is not an unambiguous indicator of disk orientation. Complex mean velocity structure may be due to a combination of these effects,

but requires detailed modeling for interpretation. Kinematic modeling of the high-velocity-resolution maps which contribute to Figures 3.1–3.4 is described in Chapters 4 and 5, but for the purposes of a preliminary interpretation, the coincidence of a mean velocity gradient with the apparent CO elongation axis is here considered a significant clue to disk orientation. The P.A. of any systematic velocity gradient seen in Figures 3.1b–4b, $\Theta_{\delta V}$, is given in column (3) of Table 3.3 for comparison with Θ_{CO}. For RY Tau and AS 209, $\Theta_{\delta V}$ was measured by taking the perpendicular to contours at the position of peak emission in Fig. 3.1a–4a, since curvature was evident in the velocity gradient.

Other constraints on the orientation of a possible disk include the observation of an optical jet, presumably oriented perpendicular to the axis of elongation. The implied disk orientation is given as Θ_{jet} in Table 3.3. However, Θ_{jet} cannot be used alone to define orientation, but agreement between several indicators strongly suggests the correct orientation of planar material. The P.A. of spatially averaged polarization vectors of scattered stellar light, Θ_{pol}, is also a function of the orientation of the scattering material (Elsässer & Staude 1978; Bastien 1982). Monte Carlo models of light scattered by disks and envelopes indicate that Θ_{pol} will be parallel to the elongation axis for flared disks and envelopes, but perpendicular to it for thin disks (Whitney & Hartmann 1992; 1993). In Table 3.3, the agreement between Θ_{CO}, $\Theta_{\delta v}$, and Θ_{pol} is generally quite good and is supported by Θ_{jet} in the case of DO Tau (Hirth *et al.* 1994). This greatly strengthens an interpretation of the structures in Fig. 3.1–3.4 as flattened disks or envelopes.

3.2 Estimates of Optical Depth and Circumstellar Mass

As shown in Chapter 2, an upper limit for the size of a central optically thick region in a circumstellar disk can be derived from the brightness temperature of peak emission at the central velocity. Assuming a typical disk temperature of $T_k = 30$ K

(Beckwith & Sargent 1993), an inclination angle of 45°, and taking into account the average beam size ($\sim 3''$), a limiting radius for an optically thick region for sources at distances of 150 pc is given by:

$$R_{\tau>1} = 80[B]^{1/2} AU$$

where B is the line-center intensity of peak emission (in Jy beam^{-1}) in a 1.30 km s^{-1} wide velocity bin. This is a conservative upper limit, since contributions from optically thin emission are ignored, and higher temperatures will significantly lower the result. For objects where a sizeable fraction of circumstellar mass is still infalling, the average temperature is likely to be higher. In column (4) of Table 3.3, $R_{\tau>1}$ is listed for each source, taking into account individual beam sizes and subtracting any contribution from the peak continuum flux (< 20% for all sources). A comparison with R_{HM} can determine to what extent the emission is optically thin. As will be evident, this is important to know in order to establish the validity of circumstellar mass estimates based on the strength of CO(2→1) emission.

The total mass of circumstellar gas can be calculated from the integrated flux of CO(2→1) emission, $\int S_\nu dv$, using (cf. Scoville et al. 1976):

$$M_{H_2} = 1.42 \times 10^{-10} \frac{(T_x + 0.93)}{e^{-16.76/T_x}} \frac{\tau_{CO}}{(1 - e^{-\tau})} \frac{D_{kpc}^2}{X(CO)} \int S_\nu dv \qquad M_\odot.$$

Here, T_x is an estimated average excitation temperature, τ_{CO} is the optical depth in the CO line, D_{kpc} is the distance to the source in kpc, and $X(CO)$ is the fractional abundance of CO. In the case of optically thin emission,

$$\frac{\tau_{CO}}{(1 - e^{-\tau})} \approx \frac{\tau_{CO}}{(1 - (1 - \tau_{CO}))} = 1,$$

and the mass is calculable without *a priori* knowledge of τ_{CO}. If the magnitude of

the optical depth is completely unknown, the above approximation provides a lower limit to M_{H_2}.

The above calculation was carried out for the sources in Table 3.1 using the integrated line flux in the maps in Figures 3.1–4 with T_x = 30K, $X(CO) = 10^{-4}$, D_{kpc} = 0.140 kpc for the Taurus sources, and 0.160 kpc for AS 209. Integrated intensities, $\int SdV$, and resulting mass estimates, M_{H_2}, are shown in columns (5) and (6), respectively, of Table 3.3. As optical depth decreases, M_{H_2} is increasingly close to the true mass; $R_{\tau>1}/\mathrm{R}_{HM}$ provides a qualitative assessment of the accuracy of the estimate. It can be seen from Table 3.2 that the upper limit to the radius of an optically thick region is at least as large as the present solar system (50 AU) for the entire sample. Molecular masses much larger than the limits in Table 3.2, but confined within a solar-system-sized radius, cannot be ruled out by these observations and are confirmed by estimates from 1.3 mm continuum emission (Beckwith *et al.* 1990; André & Montmerle 1994), typically 2 orders of magnitude larger than limits obtained here. Future observations in optically thin isostopes of CO are needed to refine estimates of the mass of circumstellar gas.

3.3 Summary

Four T Tauri stars, RY Tau, DL Tau, DO Tau, and AS 209, have been imaged in the CO(2→1) line at $\sim 2-3''$ resolution. In all cases, emission is resolved with deconvolved half-maximum radii of 100 to 350 AU. Except for DO Tau, all show evidence of a velocity gradient along the elongation axis, consistent with rotation. The P.A.'s of optical linear polarization and, in one case, an optical jet show remarkable agreement with the orientation of CO elongation and velocity gradients. From the peak strength of line emission, upper limits on the size of any optically thick inner region are found to be 50–150 AU, the approximate size of the solar system. Lower limits to the mass of circumstellar H_2 range over 2 orders of magnitude,

from 1.3 $\times 10^{-6}$ to 1.4 $\times 10^{-4}$ $M_{\odot}$, but these values are very low compared to masses estimated from the continuum emission (Beckwith *et al.* 1990; André & Montmerle 1994). Taken together, these facts suggest that circumstellar gas around these stars is configured in a disk like that believed to have given rise to our solar system. The velocity widths, morphology, and intensity of emission are consistent with centrifugally supported molecular gas sufficiently massive to support planet-forming processes expected within a *protoplanetary* disk. To make this claim unequivocally, however, it is necessary to identify the velocity field of the gas unambiguously.

4. Velocity Structure of Circumstellar Gas

Maps of the first moment with respect to velocity for RY Tau, DL Tau, DO Tau, and AS 209, are shown in Figures 3.1b–4b. The utility of this data representation lies in the simplicity with which it reveals first order trends within a set of spectral line maps or "cube." For example, velocity gradients parallel to the elongation axis of CO emission are highly suggestive of the existence of a rotating disk. However, detailed information about the velocity distribution of emission has been lost by averaging. This is a serious limitation to identifying a unique kinematic signature. In Figure 3.5, a complementary presentation of the data, spatial information is lost but velocity information retained. These CO($2 \rightarrow 1$) spectra were obtained by evaluating the integrated intensity of emission within 5″ of the stellar position in spectral line maps and plotting it as a function of velocity. In this way, the spectral signature of circumstellar gas was partially separated from that of the large ambient cloud.

Models of synthetic spectra from circumstellar disks in Keplerian rotation have been constructed by Beckwith & Sargent (1993). A "double-peaked" line shape is found that distinguishes centrifugally supported disks from spherical regions of infall. This shape results from the $1/\sqrt{r}$ dependence of the Keplerian velocity, the r^2 dependence of emitting areas with the same velocity, and the truncation of the disk

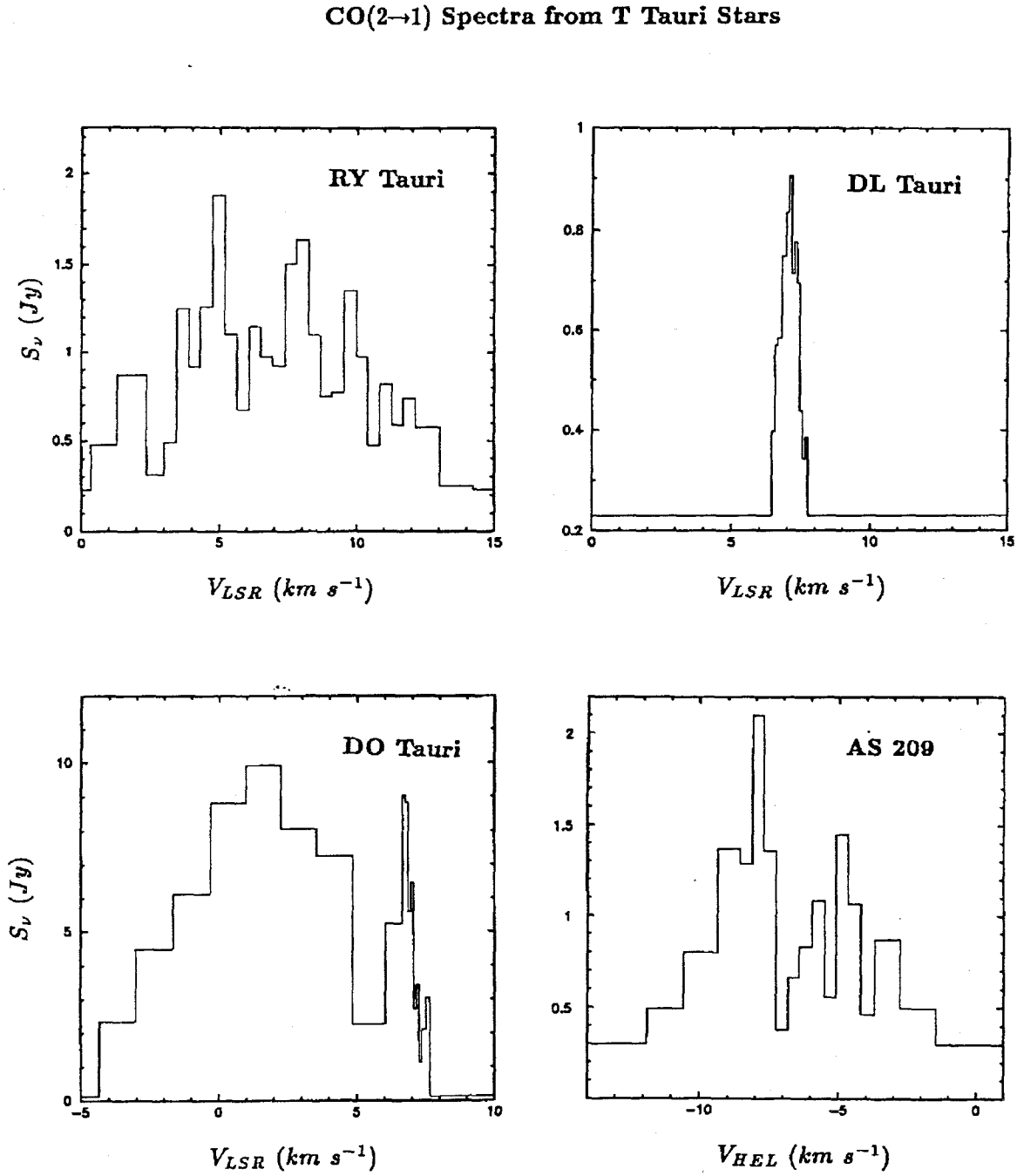

Figure 3.5. CO(2→1) spectra from the T Tauri stars, RY Tau, DL Tau, DO Tau, and AS 209. The integrated intensity from circumstellar emission in high-spatial-resolution spectral line maps is plotted as a function of V_{LSR} (V_{HEL} for AS 209). Variations in velocity resolution are the result of limited bandwidth coverage for the high velocity resolution channels. Molecular lineshapes are uniformly plotted over a width of 15 km s^{-1} for easy comparison. The continuum flux level, evident as a perfectly flat line for DL Tau, is shown outside the region of spectral coverage. The flux scale, in Jy, is not uniform between spectra, but ranges over an order of magnitude to facilitate comparison of lineshapes.

at some outer radius. Peaks in the spectra largely reflect the Keplerian velocities at the outer radius of the disk, modulated by $\sin(i)$, where i is the angle of inclination to the line of sight. Therefore, the peak velocities are a function of disk radius, R_d, central mass, M, and inclination angle, i.

Nevertheless, the existence of a Keplerian disk cannot be conclusively established or even eliminated on the basis of double-peaked spectra. Disks oriented nearly face on may have kinematic linewidths sufficiently small that double-peaked structure is blurred by the natural linewidth. Ambient cloud emission or associated outflows may distort the lineshape or fill in the central intensity minimum. On the other hand, line-center absorption by a cold intervening molecular cloud can mimic double-peaked line shape from a Keplerian disk, especially in ^{12}CO observations, where the emission is likely to be optically thick. Moreover, infall in a *flattened* structure also produces a double-peaked line shape, since infall velocities are also proportional to $1/\sqrt{r}$. This is discussed further in Chapter 4.

The spectra in Figure 3.5 may be used to refine preliminary interpretations of the circumstellar CO emission if the above caveats are kept in mind. Two of the sources, RY Tau and AS 209, have double-peaked lineshapes which are noisy, but reasonably consistent Keplerian rotation. For DL Tau, the line width is so narrow that any kinematic signature is likely to be masked by the natural linewidth. The fourth source, DO Tau, shows a spectral line an order of magnitude stronger than the other sources that is is extremely asymmetric. The dominant blue-shifted wing is most likely due to a molecular outflow, especially since a blue-shifted optical jet is known to emanate from the central star (Hirth *et al.* 1994). Redward of the peak emission, however, there is a narrow feature, centered on the systemic velocity and separated from blue-shifted emission by a prominent dip. This narrow feature and accompanying minimum may arise from a double-peaked spectrum which is associated

Table 3.4. Derived Keplerian Disk Parameters.

(1) Source	(2) $\Delta V_{spectra}$ (km/s)	(3) ΔV_{Kepler} (km/s)	(4) i (degrees)
RY Tauri	1.5	3.7	25
DL Tauri	0.3	1.4	12
DQ Tauri	1.0	1.4	45
AS 209	1.5	1.8	56

with a centrifugally supported disk and overlaps the high velocity feature. However, the central dip is deeper than expected and suspiciously located at the typical velocity of the Taurus molecular cloud, suggesting self-absorption.

None of these spectra can be taken as unambiguous proof of the presence of a Keplerian disk, but they do provide a consistency check. The Keplerian velocity at the outer radius, $\sqrt{GM/R_d}$, can be calculated assuming the central mass is approximately the stellar mass, $M \approx M_*$, listed in Table 3.1, and that the outer disk radius is given by $R_d \approx \mathrm{R}_{HM}$ of Table 3.2. The derived Keplerian velocity can then be modulated over a range of acceptable inclination angles and compared with double-peak velocities suggested by Figure 3.5. If the center-to-peak velocity difference is significantly greater than that predicted for an edge-on Keplerian disk of the observed size, Keplerian rotation can be ruled out as the dominant cause of the spectral lineshape.

Table 3.4 lists Keplerian velocities calculated in this way and center-to-peak velocity differences estimated from the spectra in Figure 3.5. For RY Tau and AS 209, this was simply taken to be half the distance between the channels with the highest amplitudes. For DL Tau, where the narrowness of the line obscures any double-peaked structure, a nominal value of one quarter of the total line width was

chosen. In the case of DO Tau, the distance between the spectral dip and the narrow velocity feature was used. None of the velocities estimated from the spectra exceed those of the Keplerian approximation. In fact, since free fall velocities exceed the Keplerian velocity by a factor of $\sqrt{2}$, this is more consistent with a rotational rather than an infall interpretation. The range of inclination angles required for agreement with Keplerian rotation is plausible and, in the case of the best-resolved disk, is consistent with an estimate based on the aspect ratio of the major and minor axes of CO emission.

4.1 Position-Velocity Diagrams

The first kinematic analysis of circumstellar gas around a T Tauri star was carried out for HL Tau with the aid of a rotation curve (Sargent & Beckwith 1987). Positions of peak emission were plotted as a function of velocity and distance from the star along the apparent axis of elongation. The data were then compared with curves that showed the radial Keplerian velocity for an edge-on disk and a given central mass. A favorable comparison was found, implying that the disk was in Keplerian rotation assuming a radial intensity profile consistent with an outer-edge origin for the peak emission. These assumptions validate the comparison of projected and radial velocities, since they have the consequence that peak emission comes from gas with its tangential velocity nearly all in the line of sight. Full kinematic modeling of aperture synthesis maps is not bound by these assumptions (cf. Beckwith & Sargent 1993; Koerner *et al.* 1993) and is a better method of analysis, but "Position-Velocity diagrams" (PVDs) which plot the full profile of emission along the elongation axis can still provide a useful representation of spectral line data for the purpose of preliminary kinematic interpretation (Richer & Padman 1991; Hayashi *et al.* 1993).

To analyze planar circumstellar gas, it is most useful to construct PVDs along the major and minor axes of CO emission. If the circumstellar gas is rotating, a

characteristic velocity gradient will be evident in the diagram constructed along the major axis, since peak emission shifts along the axis as a function of line-of-sight velocity. If this shift is linear, as in solid body rotation ($V(R) = R\Omega \propto R$), a diagonal ridge of emission appears in the PVD with slope determined by the radial velocity dependence and the inclination of the plane. If the rotation is Keplerian ($V(R) = \sqrt{GM/R} \propto 1/\sqrt{R}$), a diagonal trend is apparent near systemic velocities, but peak emission approximately follows Keplerian curves at high velocities (cf. Richer & Padman 1991; Beckwith & Sargent 1993). The appearance of PVDs can be strongly affected if the beam size used in the observations is of similar size to the emission in spectral line maps (Richer & Padman 1991).

Axisymmetric rotation will produce no diagonal effect in PVDs along the minor axis of emission, since projected velocities exhibit mirror symmetry across the major axis of emission. In contrast, material that is in free-fall will exhibit a gradient along the minor axis if it is confined to a disk. However, the appearance of an infall gradient can be mimicked by the projection of a rotational gradient on a poorly determined minor axis. In addition, infalling material can easily be confused with bi-polar outflows in such analyses, since the projected velocities are in the same direction.

PVDs have been constructed to examine in greater detail the kinematic structure of circumstellar emission around the four T Tauri stars in the sample. They are displayed in Figures 3.6–9. For each source, emission from spectral line maps was averaged over a strip one beam-width wide along axes parallel and perpendicular to the long axis P.A. indicated by the results listed in Table 3.3. Positionally coincident intensity profiles from maps at distinct velocities were then combined to form the two-dimensional arrays that are contoured in Figures 3.6–3.9. The PVD results, together with evidence from the spectra and first moment velocity maps, are now

considered below on a case by case basis.

4.1.1 RY Tau

Since RY Tau is only marginally resolved, the P.A. of CO elongation, 48°, is highly uncertain, and the kinematics of circumstellar gas are correspondingly unclear. In Figure 3.1b, the velocity gradient is fairly regular, but shows some curvature. However, $\Theta_{\delta V}$ agrees well Θ_{pol} for P.A. 20° as the orientation of elongated emission. This result differs somewhat, but not significantly from the uncertain value of Θ_{CO}. The PVDs parallel and perpendicular to this P.A. are shown in Figure 3.6. There is some velocity gradient evident in both PVDs, indicating that gas kinematics cannot be explained entirely by pure rotation about an axis with P.A. perpendicular to 20°. On the other hand, the broad linewidth seen in Figure 3.5 is consistent with rotation, given the high stellar mass estimate ($\Delta V_{Kepler} \propto \sqrt{M_*}$) and small size ($\Delta V_{Kepler} \propto 1/\sqrt{R}$). Here, analysis of emission morphology in spectral line maps is necessary to clarify the kinematics.

4.1.2 DL Tau

In contrast to RY Tau, the orientation of the elongation axis for DL Tau is reasonably well determined. All three diagnostics in Table 3.3 agree within the uncertainties. PVDs have thus been constructed parallel and perpendicular to P.A. 85° and are shown in Figure 3.7. A clear velocity gradient along the major axis is present, indicating rotation. Some variation is evident along the minor axis, but there is no systematic trend. These results, together with the extremely narrow linewidth seen in Figure 3.5, all but exclude infall and outflow as plausible explanations for the kinematics of circumstellar gas in DL Tau. From the PVD alone, it is unclear whether the rotational signature is Keplerian. It remains a strong protoplanetary disk candidate, but kinematic modeling of observations at higher spatial resolution is

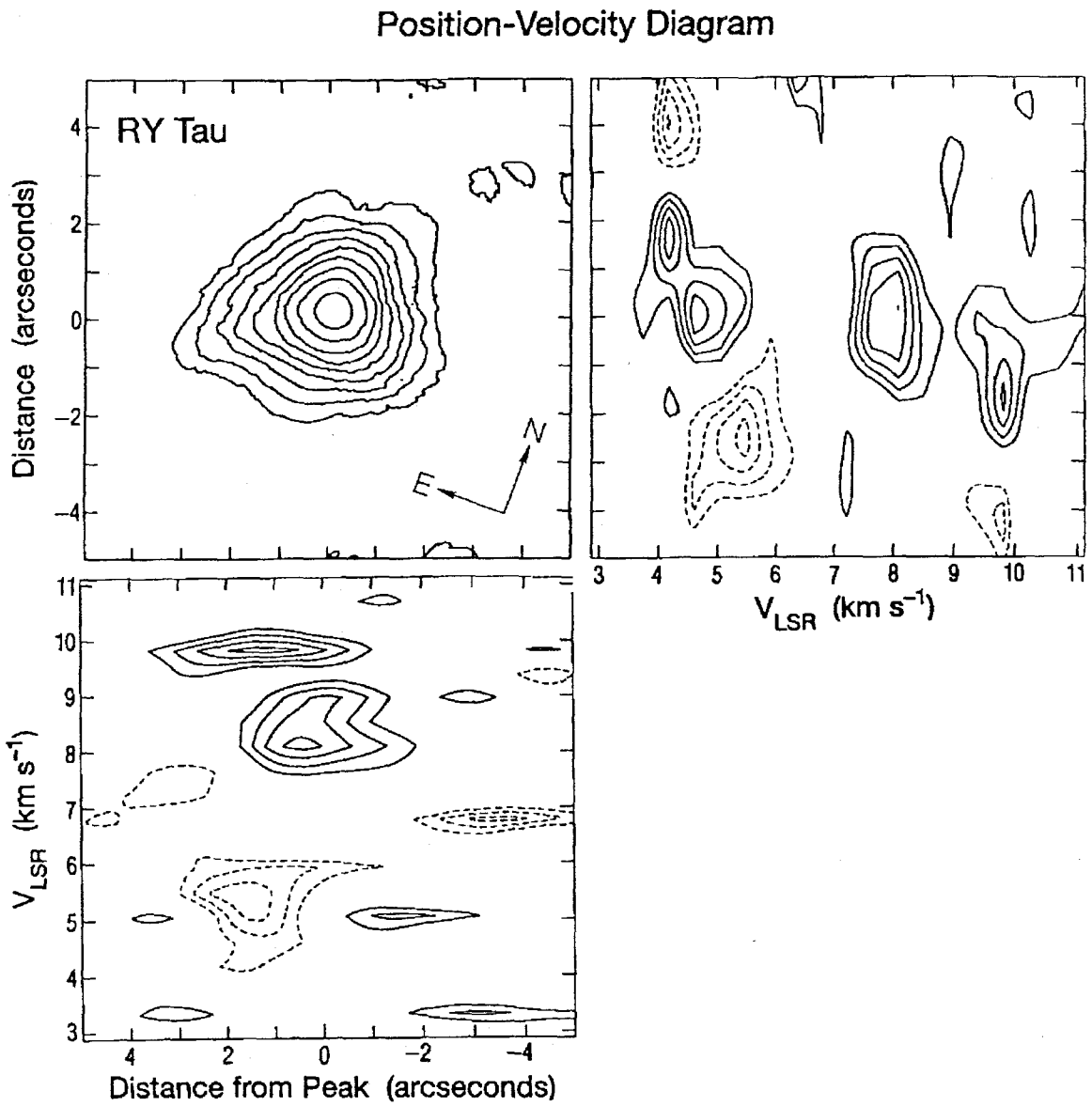

Figure 3.6. Position-Velocity Diagrams (PVDs) for RY Tau taken along axes parallel (upper right) and perpendicular (lower left) to P.A. 20°. A map of the integrated emission (upper left) has been rotated clockwise 20° for comparison to the PVDs. This orientation aligns the vertical axis with the velocity gradient, $\Theta_{\delta V}$, seen in Figure 3.1b and the average linear polarization angle of optical emission (Θ_{pol}). The deconvolved semi-major axis P.A., $\Theta_{CO} \sim 48°$, is similar but not well determined because the emission is only marginally resolved. The apparent elongation direction is largely the result of the shape of the synthesized beam (see Fig. 3.1a). The diagonal trend of emission peaks in both PVDs is either the result of combined kinematic effects or projection of a purely rotational trend on axes which are offset from the true orientation. The orientation of RY Tau is the most uncertain in the sample.

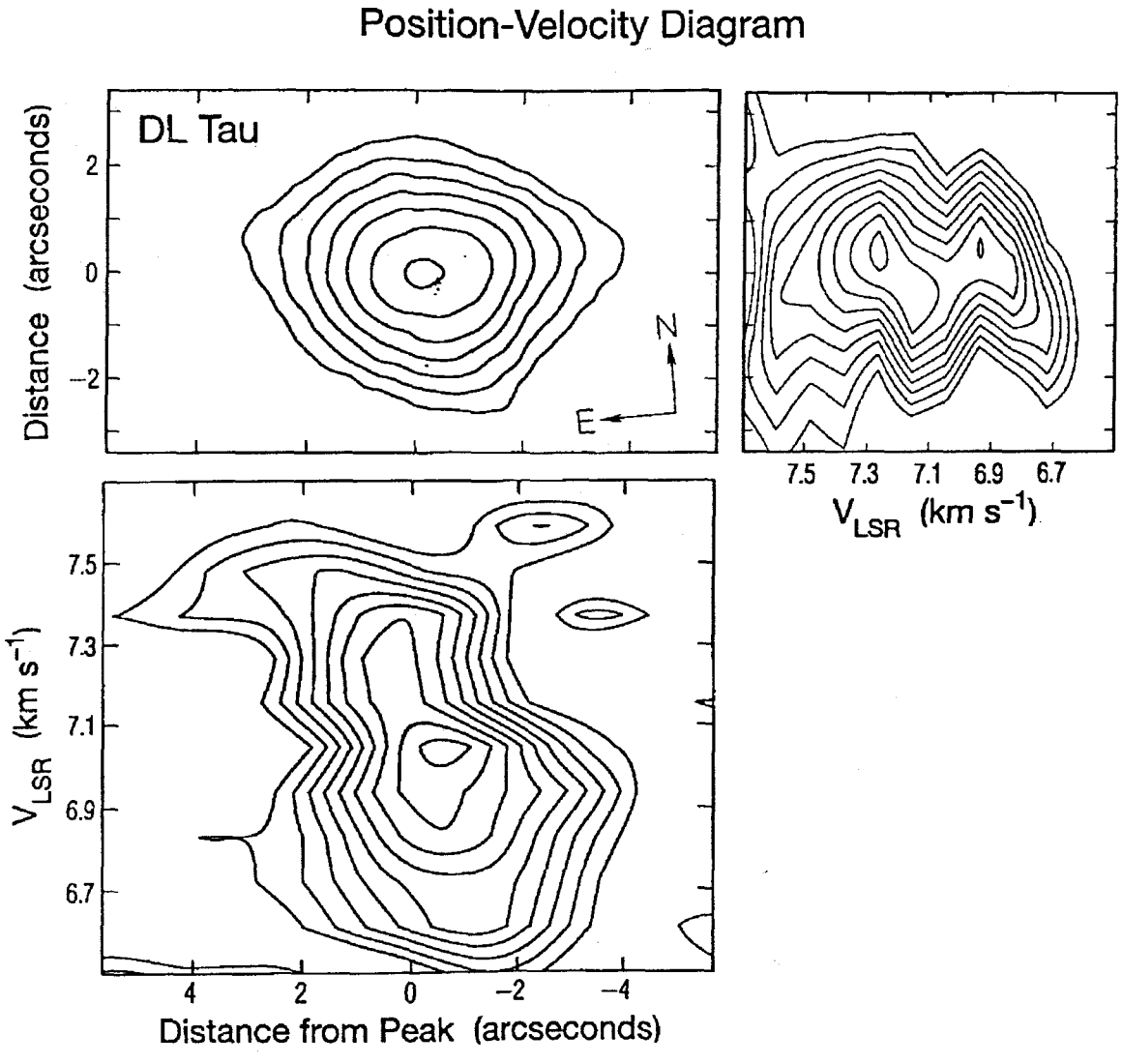

Figure 3.7. Position-Velocity Diagrams (PVDs) for DL Tau taken along axes parallel (lower left) and perpendicular (upper right) to P.A. 85°. A map of the integrated emission (upper left) has been rotated counter-clockwise 5° for comparison to the PVDs. Similar to Figure 3.6, this orientation aligns the horizontal axis with Θ_{CO}, $\Theta_{\delta V}$ and Θ_{pol}. A diagonal trend indicating rotation is apparent in the lower left panel. No similar systematic trend is apparent across the semi-minor axis (upper right).

required to confirm this.

4.1.3 DO Tau

The orientation of DO Tau is also well established (Table 3.3). However, no systematic velocity gradient is apparent in the first moment velocity map of Figure 3.3b. PVDs constructed parallel and perpendicular to P.A. 160°, and displayed in Figure 3.8, show that most of the highly blue-shifted emission originates directly from the central peak. It is unlikely that this emission is due to spatially outflowing gas; molecular outflows are usually offset from gas associated with the stellar position (Fukui *et al.* 1993). Spherical infall in the central region could be the explanation; infall patterns can result in asymmetric line profiles like that of Figure 3.5 if line emission is optically thick and accompanied by a radial temperature gradient (Zhou *et al.* 1993; Chandler & Sargent 1993). An intensity minimum appears in both PVDs at $V_{LSR} \approx$ 6 km s^{-1}, corresponding to the spectral dip in Figure 3.5. A small velocity offset is evident between blue- and red-shifted emission on either side of this minimum along *both* major and minor axes, suggesting that, if this feature is due to a circumstellar kinematic signature, rotation alone does not explain gas motions. This is additional evidence that DO Tau is a likely candidate for combined infall and rotation. Modeling of spectral line maps can confirm this possibility.

4.1.4 AS 209

Although this source exhibits minor complex features, a P.A. of possible disk orientation is identifiable (Table 3.3). The most intense emission is elongated in the same direction as Θ_{pol} and there is some suggestion of an aligned velocity gradient, but its orientation is poorly determined. Therefore, PVDs have been constructed parallel and perpendicular to the average value of Θ_{CO} and Θ_{pol} only. A rotational gradient is in evidence along the major axis of emission. Variation along the minor axis is

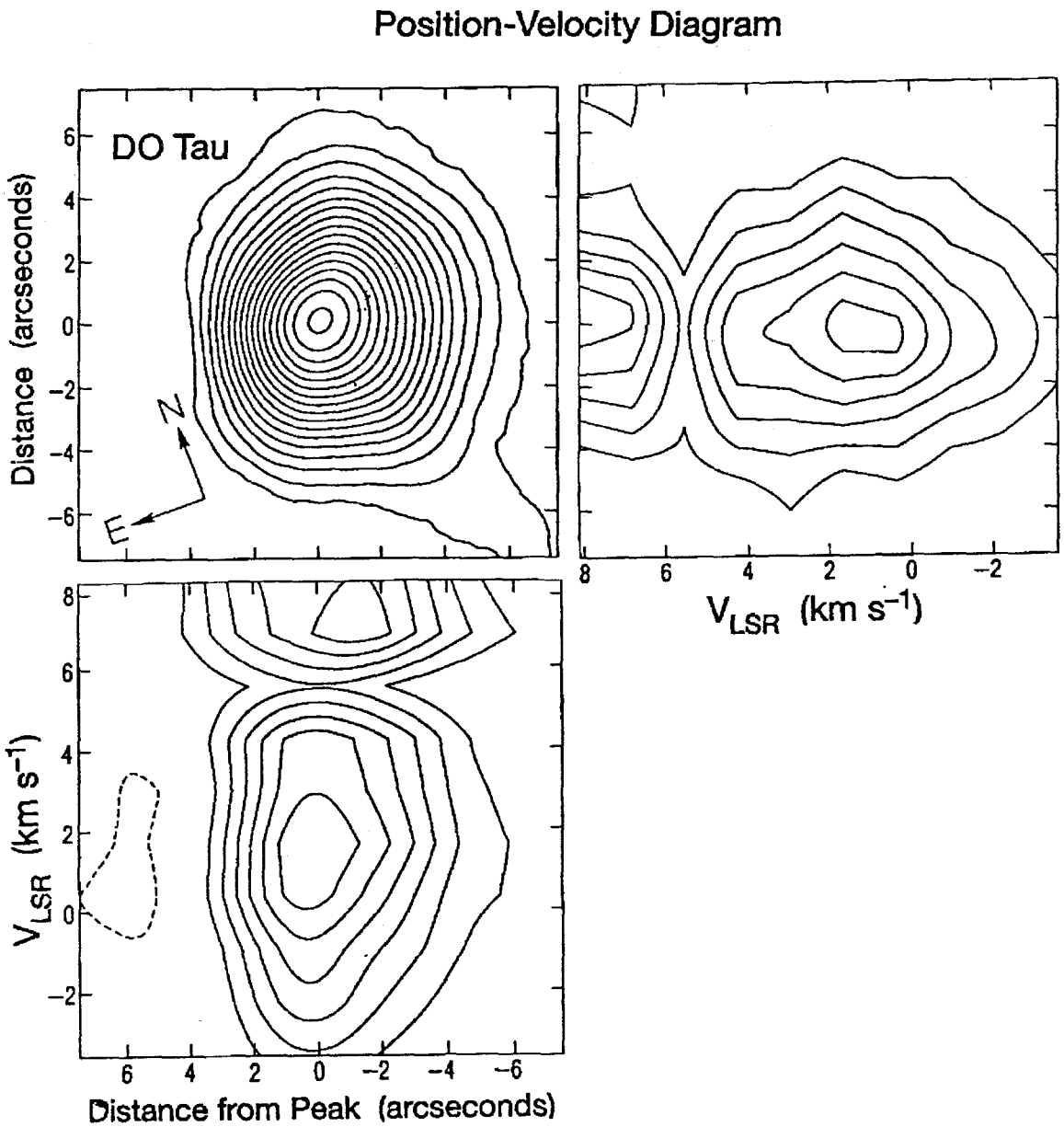

Figure 3.8. Position-Velocity Diagrams (PVDs) for DO Tau taken along axes parallel (upper right) and perpendicular (lower left) to P.A. 160°. As in Figure 3.7, a map of the integrated emission (upper left) has been rotated counter-clockwise by 20° to align the vertical axis with Θ_{CO}, Θ_{pol}, and an axis perpendicular to Θ_{jet}, the P.A. of an optical jet. At $V_{LSR} = 6$ km s^{-1}, an intensity minimum separates the blue-shifted emission from a local maximum centered at the systemic velocity. This maximum corresponds to the feature seen in Figure 3.5. The detailed lineshape is not evident at the velocity resolution used in the PVDs, but a velocity offset across the minimum at $V_{LSR} = 6$ km s^{-1} is most prominent in the PVD constructed along the minor axis, confirming an infall or outflow interpretation for the blue-shifted emission.

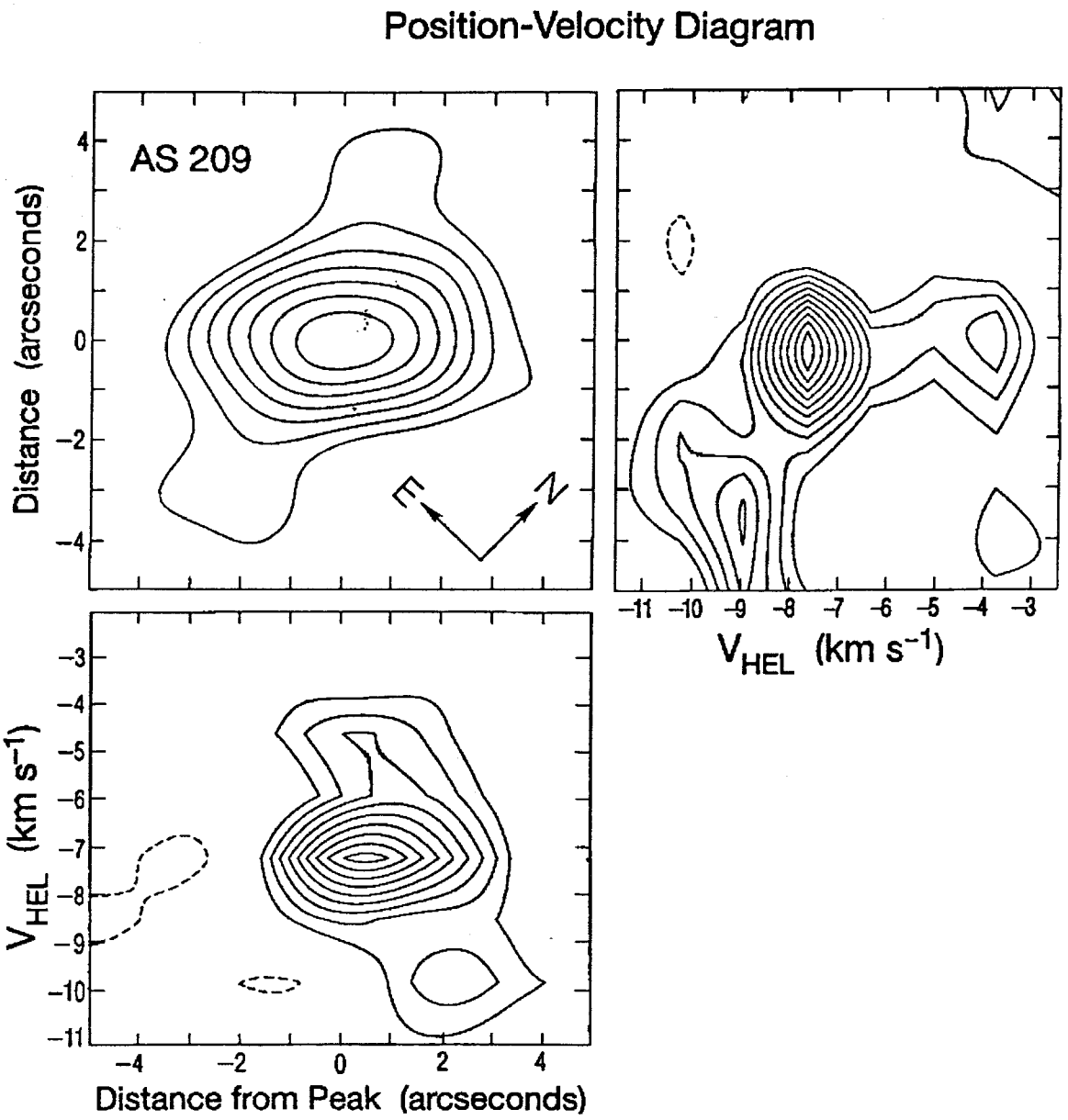

Figure 3.9. Position-Velocity Diagrams (PVDs) for AS 209 taken along axes parallel (upper right) and perpendicular (lower left) to P.A. 136°, in agreement with Θ_{CO} and Θ_{pol} from Table 3.3. As in Figure 3.7, a map of the integrated emission (upper left) has been rotated clockwise by 44° to align the horizontal axis with Θ_{CO} and Θ_{pol}. A diagonal trend indicative of rotation is evident in the PVD along the semi-major axis (lower left). Along the minor axis, most emission is centered at the peak position, but a few displaced peaks are associated with a protrusion from the disk. The latter may be associated with molecular outflow, but are not oriented strictly perpendicular to the disk.

confined to blue-shifted emission associated with a feature that protrudes at an angle from the elongated morphology, perhaps due to outflow. This interpretation is consistent with the hint of a velocity gradient seen across the minor axis of emission in Figure 3.4b. It is worth noting that, among the sample, the spectrum of AS209 in Figure 3.5 most resembles a classic double-peaked lineshape. This object remains a strong candidate for a rotating protoplanetary disk, perhaps with an outflow.

In summary, three of the four sources observed, RY Tau, DL Tau, and AS 209, exhibit velocity gradients consistent with rotation. The spectral lineshapes and widths of these objects also support the view that the dominant gas motion is rotation. Position-Velocity Diagrams along the major and minor axes of CO emission also show evidence of rotation, It may be that the spatial resolution of the current observations is inadequate to trace signatures of Keplerian rotation in detail. Evidence of kinematic components other than rotation is apparent for three sources, RY Tau, DO Tau, and AS 209. One, DO Tau, exhibits a prominent blue-shifted emission wing, consistent with a molecular outflow or non-planar infall. RY Tau and AS 209 show evidence of some velocity structure orthogonal to that interpreted as rotation. In one case, RY Tau, this may be due to uncertainty about the orientation of circumstellar gas; the other shows morphological evidence for outflow.

5. Conclusions

The size, morphology, and velocity structure of molecular emission from the T Tauri stars in this survey are in marked contrast to the earliest observations of T Tauri stars. These suggested sizes greater than 1000 AU (Sargent & Beckwith 1987; Weintraub *et al.* 1987) and gas motions dominated by infall (Hayashi *et al.* 1993; van Langevelde *et al.* 1993) For the stars observed here, the radial extent of circumstellar gas, of order 100 AU, is much smaller and similar to that of the solar system, but masses are only limits and much less than the minimum mass solar nebula. The

morphology of line emission is somewhat elongated with velocity gradients along the semi-major axis; polarization of optical emission and the orientation of an optical jet confirm that elongation of emission is largely due to of circularly symmetric material confined to a plane. The dominant kinematic signature in spectra and PVDs is consistent with centrifugal support of the circumstellar gas.

In the above respects, circumstellar CO($2 \rightarrow 1$) emission from the T Tauri stars surveyed shows characteristics which confirm the conjecture that these stars are surrounded by protoplanetary disks like that which gave rise to our solar system. Further work is needed to secure this interpretation. Only full kinematic modeling of spectral line maps can uniquely establish the velocity field of circumstellar gas. Higher spatial resolution than the $\sim 3''$ available here may also be necessary to trace kinematic patterns sufficiently to identify their origin. Finally, observations in less optically thick isotopes of CO are needed to ascertain whether the circumstellar mass available to planet formation is comparable to that of the minimum mass nebula required to make a planetary system like our own.

CHAPTER 4

A Kinematic Model of Infall and Rotation in a Disk

1. Introduction

Direct observations of the kinematic state of circumstellar gas around T Tauri stars are of major consequence for theories of planetary system formation. If the material is in a state of free-fall, or *dynamic* accretion, it has a greater chance of being incorporated into the star than mass which is centrifugally supported at the same radius. Orbiting material may still be *viscously* accreted onto the star (Adams & Lin 1993), but this process is vastly less efficient at evacuating all circumstellar material. Virtually every viscous mechanism invoked for angular momentum transfer in disks requires that some fraction of circumstellar mass remains in orbit (Lin & Papaloizou 1985). This remnant material is potentially available to form planets.

For the majority of T Tauri stars, circumstellar masses of dust and gas are small compared with the stellar mass (Beckwith *et al.* 1990; André & Montmerle 1994), and viscous accretion timescales are estimated to be much larger than orbital timescales (cf. Cassen *et al.* 1985). Consequently, centrifugally supported gas and dust is expected to travel in nearly circular Keplerian orbits about the central star. The positive identification of Keplerian rotation in circumstellar disks thus has profound consequences, implying that the detected gas is confined to disks that represent nascent planetary systems rather than originating in protostellar envelopes.

The instrumental technology needed to image circumstellar molecular gas around the nearest T Tauri stars is very young. Disks radiate predominantly at far infrared and sub-millimeter wavelengths and have angular extent of order 1″. Molecular line widths indicate velocity dispersions of only a few km s^{-1}. These properties place stringent requirements on the astronomical techniques employed for their study. High velocity and spatial resolution at wavelengths longward of 100 μm are necessary. Millimeter-wave arrays have just begun to meet the challenge. High resolution ($\sim$ few arcseconds) aperture synthesis images of the gas in circumstellar disks that meet the

spatial needs are now available. However, new tools must be developed to understand the kinematics which give rise to the complex morphology that appears in spectral line maps. The utility of moment maps, spectra, and Position-Velocity Diagrams (PVDs) for analyzing the kinematics of circumstellar disks was discussed in Chapter 3. While provocative, the results are not conclusive; a more direct comparison of data with models of Keplerian rotation would be preferable. It is possible to analyze complete sets of spatial and velocity information using model-generated spectral line cubes. The fundamental approach is discussed by Beckwith & Sargent (1993) and illustrated by the study of GM Aurigae (Koerner *et al.* 1993 and Chapter 2). Although this initial model can positively identify a rotating disk, it must be modified to take into account the presence of infalling material. A kinematic disk model which parametrizes both infall and rotational velocity components in a simple but physically appropriate manner is presented here. Comparing this model to observed spectral line maps will clarify the kinematic details of the observed, flattened, circumstellar structures. Where disk-envelope systems are revealed, it will allow a determination of the fraction of circumstellar mass available to planetary system formation.

2. Dynamic Accretion in a Disk

Until recently, the protostellar collapse of a molecular cloud core was considered almost exclusively within the context of spherical geometry (e.g., Shu 1977). This was due in large part to the analytical and numerical convenience provided by spherical symmetry, but also because the existence of a general symmetry-breaking mechanism (other than special initial conditions or simple rotation) was unanticipated. Conservation of initial cloud angular momentum was included in the infall models of Cassen & Moosman (1981) and Terebey *et al.* (1984) and resulted in the deflection of radially infalling gas onto a centrifugally supported disk, but the radius, R_{env}, at which pressure support in the cloud gave way to gravitational attraction re-

mained independent of azimuthal or latitudinal angle. These calculations confirmed the popular notion that star formation takes place by means of a *spherical* envelope of gas falling onto a *flattened* disk. This idea appeared to be further supported by observations of roughly spherical molecular cloud cores (Myers & Benson 1983) and a smaller flattened structure around the young stars, HL Tauri and R Mon (Dyck *et al.* 1984; Beckwith *et al.* 1986; Sargent & Beckwith 1987). The inferred anisotropic distribution of circumstellar dust grains around T Tauri stars (Adams *et al.* 1987; 1988) was even commonly cited as evidence that the radiating dust did not reside in an infalling envelope, but was confined to a centrifugally supported circumstellar disk (cf. Beckwith *et al.* 1990). This morphological identification of disks and envelopes – planar rotation vs. spherical infall – has been called into question by mounting observational evidence and theoretical models.

The unexpected discovery of bipolar outflows in very young stars (Snell *et al.* 1980) and the biconical shape of associated reflection nebulae were among the first observational clues that accreting dust and gas may not always be configured in a spherical distribution (cf. Kenyon *et al.* 1993a, 1993b). More recently, it has been suggested that circumstellar dust around many T Tauri stars is not confined to a plane, but occupies some additional volume above and below the disk; clearly it cannot be spherically distributed or the stars would be invisible. Monte Carlo models of stellar light scattered by circumstellar dust require a non-planar density distribution to reproduce many optical and IR observations of reflection nebulae (Whitney *et al.* 1992, 1993; Kenyon *et al.* 1993a). Radiative transfer models also need additional dust to fit observed Spectral Energy Distributions (SEDs) in the mid-infrared spectral region (Natta 1993; Kenyon *et al.* 1993b; Calvet & Hartmann 1994). Standard accretion disk theory indicates a steeper power law dependence of the radial temperature profile than is observed. Additional heating of the disk by the radiation of

stellar-heated dust grains above the disk can account for the observed temperature profile.

A theoretical justification for flat envelopes was recently provided by simulations of Galli & Shu (1993). They solved numerically the MHD equations for a collapsing isothermal sphere threaded by a uniform magnetic field and found that strong magnetic pinching forces deflected infalling gas toward the equatorial plane to form a flattened disequilibrium structure. This structure is not centrifugally supported, but its geometric shape is that of a disk. Galli & Shu (1993) have named it a "pseudo-disk" to differentiate it from a standard accretion disk. They find it has an approximate diameter of 2000 AU when scaled with typical molecular cloud parameters.

Further evidence of infall in disks comes from Stahler *et al.* (1994) who derived an evolutionary sequence of model disks without viscosity in order to study the early development of circumstellar material. They found three distinct components to disks during the infall stage of star formation: an outer disk in which shocked gas retains free-falling momentum; an inner disk where gas is in circular Keplerian orbits, and a turbulent boundary adjoining the regions. Infalling material is flattened because any given parabolic streamline (cf. Cassen & Moosman 1981) is matched by a mirror-image counterpart with which it collides in the equatorial plane. Infalling and angular momentum is transported across a shocked boundary to form an outer disk of infalling gas with conserved angular momentum.

Hayashi *et al.* (1993) have recently suggested that their observations of the flat molecular structure observed around HL Tau support the existence of a pseudo-disk. By reading velocity differences directly from PVDs, constructed from maps obtained with the millimeter array at Nobeyama Radio Observatory, they infer that the mass accretion rate in the infall envelope exceeds that from the disk onto the stellar surface

by an order of magnitude. This has led Lin *et al.* (1994) to propose that HL Tau is an FU Orionis object in quiescence. Although the evidence for some component of infall in HL Tau's circumstellar gas is strong, the PVDs displayed by Hayashi *et al.* (1993) are at inadequate velocity and spatial resolution to quantitatively identify the ratio of infall and rotational velocity components. As discussed previously, it would be advantageous to generate the complete set of synthetic spectral line maps with a model data cube.

The interpretation of the observations of Chapter 3 and the source HL Tau, just described, would benefit from kinematic modeling. Here, a model is described from which synthetic maps may be constructed for a disk, similar to that of Stahler *et al.* (1994), with parametrized partitioning of radial (infalling) and tangential (rotational) velocity components.

3. Rotation and Free Fall Contrasted

The motion of gas falling toward a protostellar source is supersonic within a radius, R_{env} (Shu 1977; Terebey *et al.* 1984), and can be approximated as ballistic trajectories on which individual parcels conserve energy and momentum (Cassen & Moosman 1981). For a mass element with negligible initial angular momentum, the free-fall velocity direction is radially inward toward the young star and the magnitude can be derived approximately from simple energy conservation. For zero total energy at an infinite distance from the central star

$$E = \frac{1}{2}\mathrm{V_r}^2 - \frac{GM_*}{r} = 0 \quad ,$$

where V_r is the radial velocity and M_* is the central mass. Solving for V_r, the velocity magnitude is $\sqrt{2GM_*/r}$. Thus, V_r has the same radial dependence as the Keplerian velocity and differs from it in absolute magnitude by a factor of only $\sqrt{2}$. It is therefore difficult to distinguish between infall and rotation on the basis of spatially

averaged data such as spectra. For infall, however, the velocity direction is orthogonal to that in the rotational state. This geometric difference has a direct effect on the morphology of gas emission in spectral line maps.

It is a simple matter to adapt the rotational model of Koerner *et al.* (1993) (Chapter 2) to investigate the appearance of molecular line emission from free-falling gas that is confined to a disk. The direction of model velocity vectors must be rotated by $\pi/2$ from that of orbital motion, and their magnitudes must be multiplied by a factor of $\sqrt{2}$. Resulting synthetic line maps for a 1000 AU radius disk around a solar mass star, where gas is rotating or in free fall, are shown in Figures 4.1 and 4.2, respectively. The disk is inclined 45° and convolved with a 1″ beam to represent the best possible observing conditions with the Owens Valley Millimeter Array operating at $\lambda = 1$ mm. For sources in the Taurus cloud, 1″ corresponds to the spatial scale 140 AU (Elias 1978; Kenyon *et al.* 1994). The maps shown are at velocities that correspond to the center, inner slope, peak, and outer wing of the integrated intensity spectra, also shown in Figures 4.1 and 4.2. At these velocities, emission morphology is strikingly similar in both cases but, as expected, rotated by 90°. This is a direct consequence of the angular difference between the infalling and rotational velocity vectors and corresponds to the orthogonality of respective velocity gradients in first moment maps and PVDs. An easily identifiable diagnostic appears in maps at the systemic velocity; emission is elongated along the major axis for infall, but along the minor axis for rotation. As discussed in Chapter 3, establishing disk orientation is critical to discriminating between these kinematic states.

Line shapes in Figures 4.1 and 4.2 appear similar, but the infall spectrum is broadened by a factor of $\sqrt{2}$. It is worth emphasizing that *both* spectra are double-peaked, since this shape is frequently invoked as unambiguous evidence of rotation only (e.g., Skrutskie *et al.* 1993).

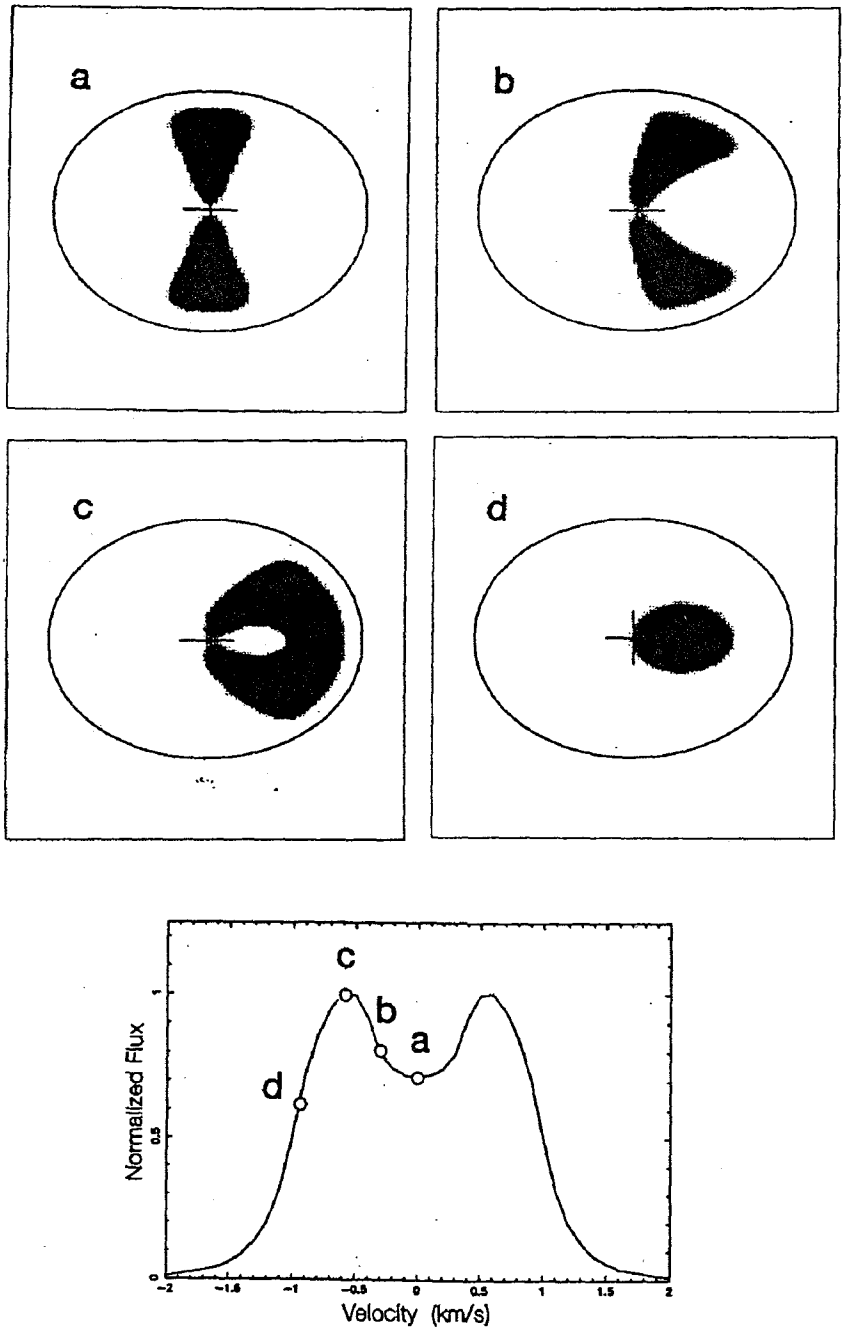

Figure 4.1. Synthetic spectral line maps generated from a kinematic model of a 1000 AU radius disk in Keplerian rotation. The structure is shown as it would appear located at the distance of the Taurus molecular cloud (140 pc) at 1″ resolution, inclined 45° from edge on. Individual maps are at velocities corresponding to regions a,b,c,and d on the double-peaked spectral line shape below. These correspond to the line center, inner slope, peak, and outer wing, respectively.

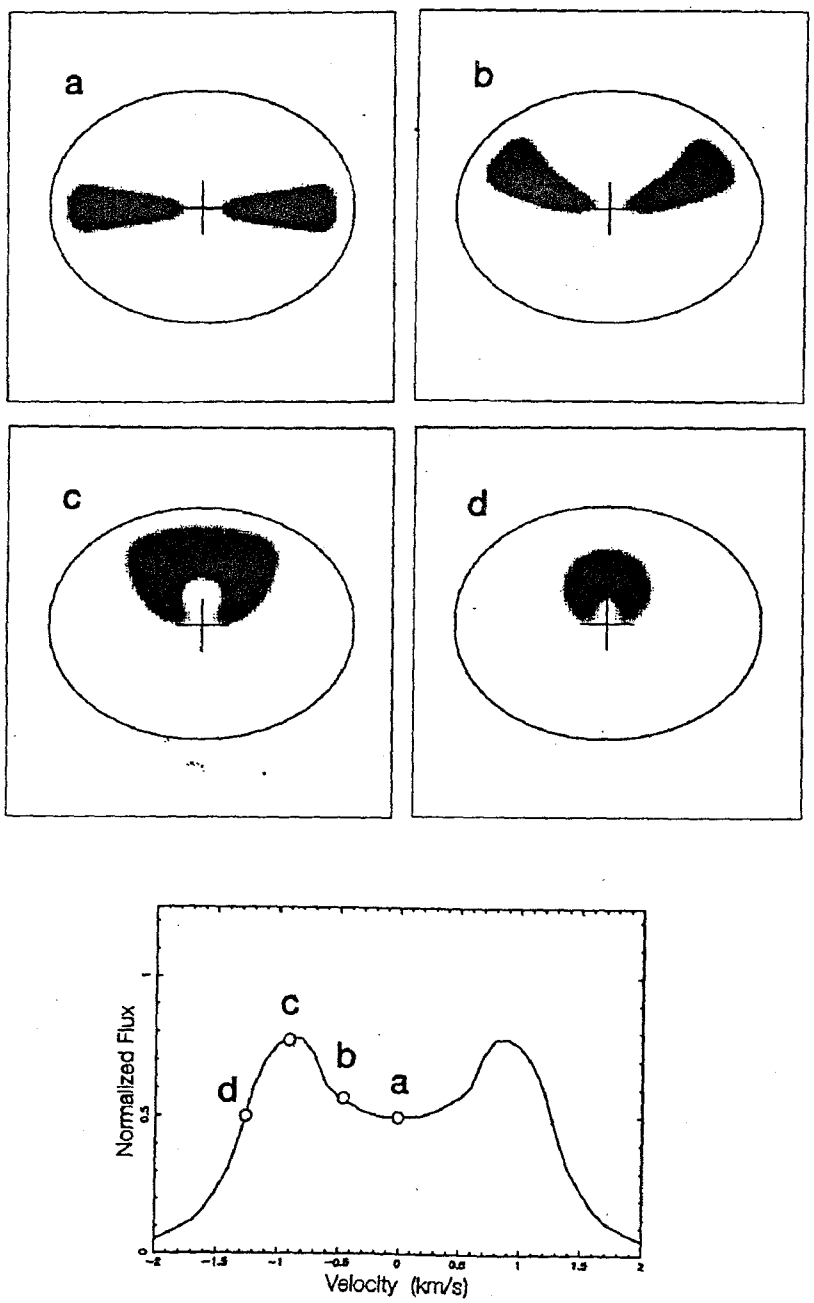

Figure 4.2. As in Figure 4.1, but for a disk of free-falling gas. Note that the spectral lineshape is also double-peaked, but the linewidth is broader by a factor of $\sqrt{2}$.

4. Rotation and Free Fall Combined

The magnitude of rotation observed in molecular cloud cores ($\sim$ 0.2 km s^{-1} pc^{-1} in Taurus; Kleiner & Dickman 1984) virtually assures that some rotational component of velocity will be evident in circumstellar material around T Tauri stars. The *pure* free-fall model illustrated in Figure 4.2 is, therefore, physically implausible; some component of rotation must be present. Figures 4.1 and 4.2 may, however, be considered end-members of a class of disks spanning a range of kinematic states, from pure infall to complete centrifugal support. Orthogonal angular and tangential unit velocity vectors form a complete basis for motion in the polar coordinate system that is particularly appropriate for disks. All that is needed to construct a combined kinematic model is a physically reasonable parametrization of vector magnitudes that is appropriate for flat disk-envelope systems.

The envelope velocity structure is well-defined if the appropriate expressions can be obtained for the tangential velocity, V_θ, and the radial velocity, V_r, as a function of radius. Assuming that gas motions in the envelope are well-approximated by simple ballistic trajectories, simplified equations of energy and angular momentum conservation can be used to solve for these two unknowns. The energy conservation equation is given by

$$\frac{1}{2}\left[{V_\theta}^2 + {V_r}^2\right] - \frac{GM}{R} = 0 \quad ,$$

and conservation of angular momentum requires that

$$V_\theta R = \sqrt{\frac{GM}{R_{disk}}} \times R_{disk} = \sqrt{GMR_{disk}} \quad .$$

Here, R_{disk} is the "centrifugal radius" at which the gas motion is circular Keplerian. Solving for the velocity components separately leads to

$$V_\theta(R) = \sqrt{\frac{GMR_{disk}}{R^2}}\ , \quad \text{and}$$

$$V_r(R) = \sqrt{\frac{2GM}{R} - \frac{GMR_{disk}}{R^2}}\ .$$

These equations can be used to model the region exterior to a freely parametrized centrifugal radius. Their physical significance is straightforward. The tangential velocity, V_Θ, displays R^{-1} dependence expected for angular momentum conservation, while $V_r(R)$ is modified from its free-fall value by a centrifugal force term. This term is small throughout most of the infall path, but achieves half the free-fall value by the time gas arrives at the disk; interior to R_{disk}, the velocity structure returns to the Keplerian specification. It is implicitly assumed that most of the kinetic energy of the infalling material is dissipated in either an accretion shock or a turbulent layer like that of Stahler *et al.* (1994). The term R_{disk} thus specifies velocities in the infall region and also defines its boundary with an inner Keplerian disk. This is precisely the parameter that should be freely fit to the data, since it quantifies the degree to which circumstellar material is centrifugally supported.

Results from the combined infall-rotation model are shown in Figure 4.3 for disks with the same physical parameters as in Section 4.2 (i.e., 1000 AU radius, inclined at 45°). In the upper panels of Figure 4.3, a system with $R_{disk} = 500$ AU is shown. The rotational pattern of the inner disk matches that of the pure rotation model shown in Figure 4.1, but a substantially different pattern is evident in the outer envelope. The rotational component of the infall region distorts the simple pattern seen in Figure 4.2. Due to the R^{-1} dependence, this distortion increases with decreasing radius until an abrupt change occurs at R_{disk} as the radial infall velocity component dissipates.

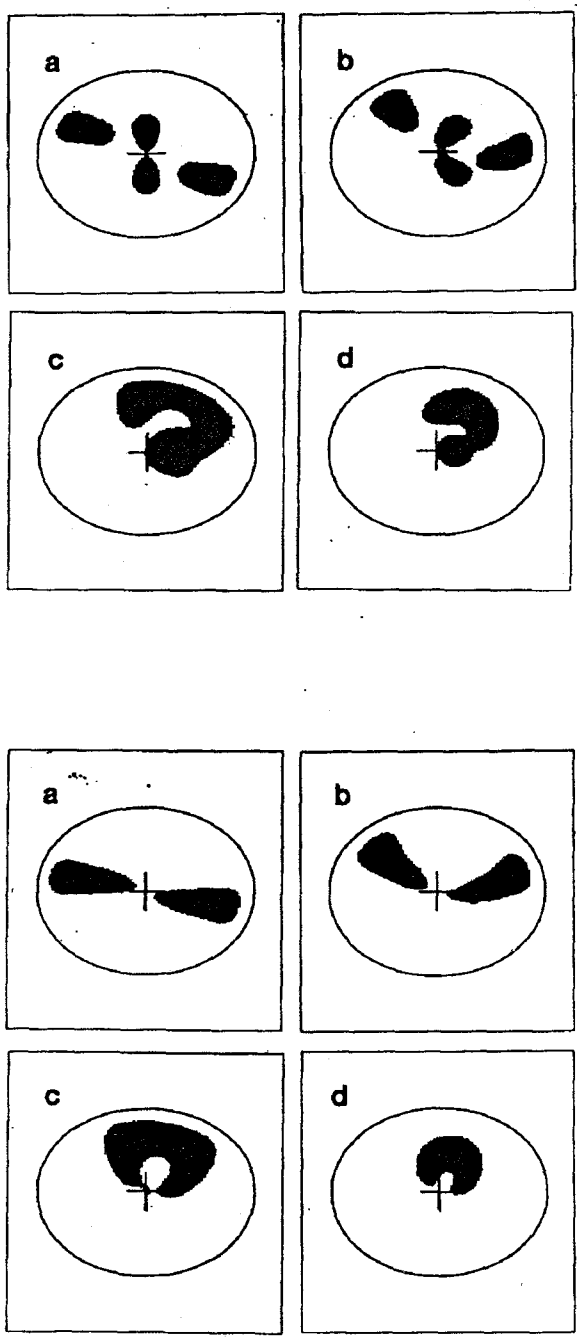

Figure 4.3. a) Synthetic spectral line maps generated from a kinematic model of a 500 AU radius disk in Keplerian rotation surrounded by a flat infalling envelope with outer radius 1000 AU. The whole structure is shown as in Figure 4.1; b) As in a), but with a 100 AU disk in Keplerian rotation. The rotational disk signature is not evident at this resolution but is revealed indirectly by the rotational distortion of the infall pattern. Spectral lineshapes corresponding to both a) and b) are displayed in Figure 4.4.

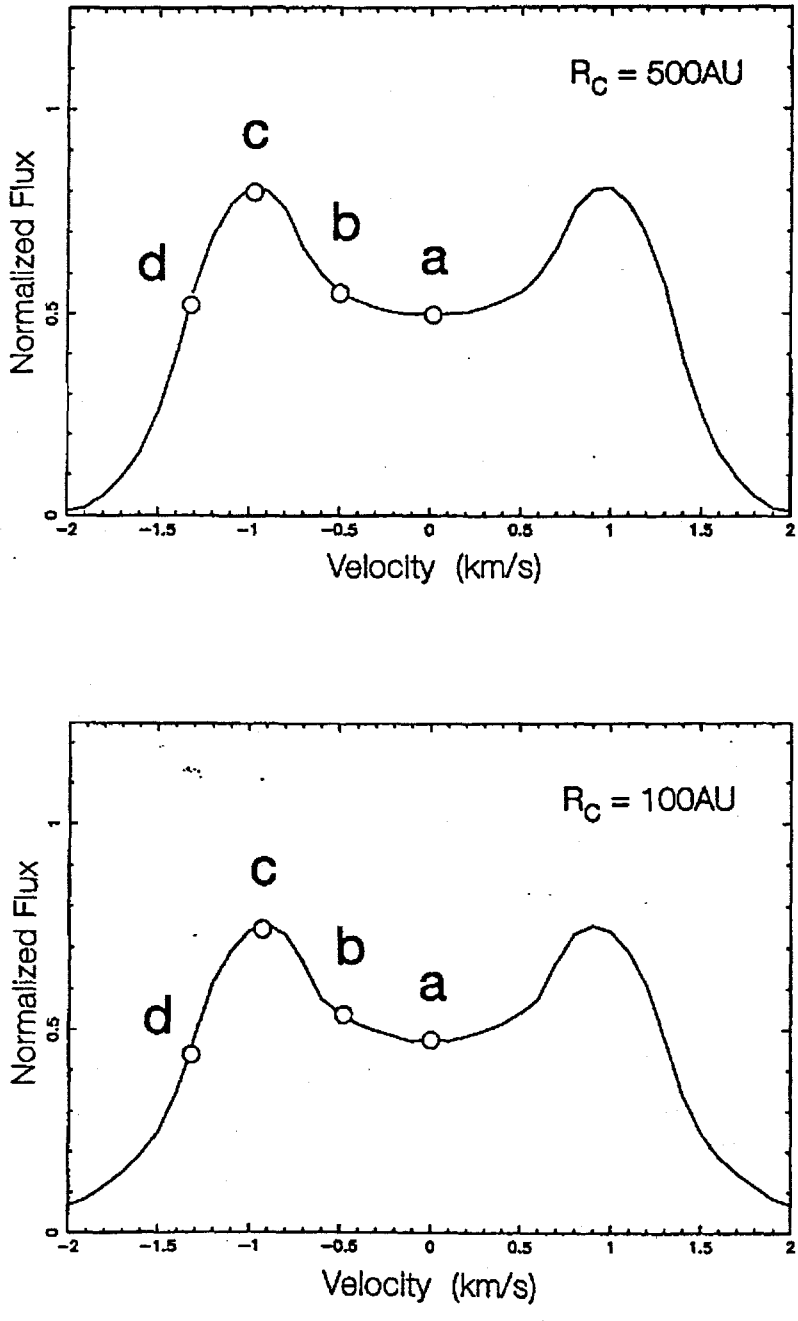

Figure 4.4. Synthetic spectral lineshapes generated from a kinematic model of a disk in a combined state of rotation and infall. Model spectra for a 500 AU radius disk with 1000 AU envelope radius and a 100 AU radius disk with 1000 AU envelope radius are shown in upper and lower plots, respectively. Other parameters are the same as those used to construct the maps in Figure 4.4. Because the outer part of the disk dominates the spectrum, the spectral shapes and widths are very similar to that in Figure 4.3 (pure infall), even though one example is centrifugally supported out to half of its full radius.

The lower panel of Figure 4.3 shows a model with $R_{disk} = 100$ AU. This size is comparable to our own solar system and is more commonly thought to be an appropriate dimension for a centifugally supported disk (cf. Cassen *et al.* 1985). The kinematic pattern of the inner disk is now beyond the resolution of the observations. Nevertheless, the rotational distortion of the outer envelope is detectable, and a disk could in principle be inferred by fitting this distortion. However, the disk orientation would have to be known with great certainty. Spectra appropriate to each example are shown in Figure 4.4. They are both similar to the pure infall spectrum, since the double-peaked chearacter is due to line-of-sight velocities from material near the outer radius where the infall component dominates all three models.

5. Comparison of Model to Data

Koerner *et al.* (1993) matched a kinematic model of Keplerian rotation to aperture synthesis maps of GM Aurigae by simple visual inspection. This was an adequate procedure for their purposes, since the principal objective was to demonstrate that the disk was centrifugally supported. The parameters M and i, central mass and inclination angle, were estimated only as a secondary goal. In the combined rotation-infall model, described above, a third parameter must be determined in order to establish the case for centrifugal support. The accompanying patterns in the synthetic aperture synthesis maps also display an increased degree of complexity (cf. Figure 4.3) that is difficult to interpret by simple visual inspection. A more quantitative method of comparing model maps with the data is now required.

The kinematic model generates spectral line maps from a disk with a radial emissivity, $\epsilon(r)$, that approximates the integrated line emission with Gaussian functions (cf. Koerner *et al.* 1993). Since $\epsilon(r)$ is not dictated by any physical parameters of interest, its absolute value is of little interest in a quantitative fit to the data. It is important, however, that its radial dependence be suitably chosen to allow model-

to-data comparisons to be considered on the basis of kinematic considerations alone. This is accomplished by fitting one or more elliptical Gaussians to the integrated line emission, deconvolving with the CLEAN beam, and using the resulting widths at half maximum along the semi-major axis to approximate the radial intensity of disk emission. Although amplitude fitting with a complete radiative transfer model of circumstellar line emission (e.g., Beckwith & Sargent 1993) is desirable for a study of the density and temperature structure of disks, this requires observations in multiple CO isotopes and optically thin transitions. For the purely kinematic analysis described here, only the *morphology* in spectral line maps is quantitatively compared for parameter estimation. Hence, cross-correlation rather than least squares fitting has been employed to quantitatively compare model maps with aperture synthesis images.

The cross-correlation function, $\chi(\mathbf{r})$, is given by

$$\chi(\mathbf{r}) = N \int_{-\mathbf{r}}^{+\mathbf{r}} I(\mathbf{r}' - \mathbf{r}) M(\mathbf{r}') d\mathbf{r}' \quad ,$$

where $\mathbf{r} = (x, y)$ is the position in the map plane, N is a normalizing factor such that $\chi(0,0) = 1$ for two identical functions, $I(\mathbf{r})$ is the observed image intensity, and $M(\mathbf{r})$ is the model image intensity. In the numerical code used to generate model emission, synthetic maps are Fourier transformed for convolution with a Gaussian beam that matches the synthesized beam of the observations. It is thus convenient to carry out cross-correlation of the Fourier Transform of the model with the Fourier Transform of the image. The cross-correlation in Fourier Space, $\widehat{\chi(\mathbf{v})}$, is a simple product, given by

$$\widehat{\chi(\mathbf{v})} = \widehat{I(\mathbf{v})}\ \widehat{M^*(\mathbf{v})} \quad ,$$

where $\mathbf{v} = (u, v)$ is the positional coordinate in the Fourier plane, $\widehat{I(\mathbf{v})}$ is the Fourier transform of the image, and $\widehat{M^*(\mathbf{v})}$ is the complex conjugate of the Fourier transform of the model.

For specific values of the parameters R_{disk}, M, and i, a weighted average of the cross-correlations of model maps with corresponding observed maps in a complete spectral line cube can now be obtained. Best-fit parameter values can be obtained by maximizing χ over parameter space. The uncertainty in this procedure is not rigorously quantified; an analytic expression for the goodness of fit or uncertainty in parameter estimation is not formally available, for example. Nevertheless, this method provides a best-fit estimate of M, i, and R_{disk}, given the model. Visual inspection still provides a qualitative check on the goodness of fit. Eventually, Monte Carlo simulations can be carried out to assess goodness of fit and uncertainties in estimating the parameters. Ongoing research in collaboration with A.I. Sargent aimed at refining estimates of the centrifugal radius of HL Tau will incorporate this technique. The objective here, however, was similar to that for GM Aur; quantitative parameter estimates have been employed to obtain the best assessments of the kinematic state of newly-detected circumstellar gas around a sample of T Tauri stars.

CHAPTER 5

Kinematic Modeling of Molecular Line Emission from T Tauri Stars

1. Introduction

Preliminary velocity analyses of molecular line emission from T Tauri stars, presented in Chapter 3, strongly suggest that the detected circumstellar gas is centrifugally supported inside solar-system sized radii. Most ambiguity in this interpretation partly stems from reliance on first moment velocity maps and Position-Velocity Diagrams (PVDs). In both maps and PVDs, data is averaged either spatially and spectrally, reducing information available to constrain final interpretations. The study of GM Aur, described in Chapter 2, demonstrated that it is now observationally feasible to identify velocity-related patterns on scales relevant to circumstellar disks and simulate these high-resolution data sets with kinematic models, as outlined in Chapter 4. Using this procedure, any ambiguity in more simplistic kinematic interpretations can be eliminated. Good quality data are, however, essential. Here, the method is applied on a case by case basis to the T Tauri star observations described in Chapter 3.

2. RY Tau

Aperture synthesis maps of CO(2→1) emission from RY Tau at velocity intervals of $\Delta V = 0.6$ km s^{-1} are displayed in Figure 5.1. Proceeding from left to right and top to bottom, map velocities start at $V_{LSR} = 3.8$ km s^{-1} and cover the range $\Delta V = 7.2$ km s^{-1}, comprising most of the linewidth of the spectrum of RY Tau in Figure 3.5. Peak intensity in the maps shows a velocity dependence which corresponds to the double-peaked spectral line shape. Emission appears in the first four maps, peaking at $V_{LSR} = 5.0$ km s^{-1}. It largely disappears in maps near the systemic velocity, but re-emerges at red-shifted velocities to achieve another local maximum at $V_{LSR} = 8.6$ km s^{-1}. Peak positions shift along P.A. $\sim 20°$ to produce the velocity gradient seen in Figure 3.1b, but only by a fraction of the beam-width. Both the spectral and spatial distribution of peak intensities are consistent with a kinematic

interpretation of circumstellar gas in which a disk is centrifugally supported about a rotational axis perpendicular to P.A. $\sim 20°$ as inferred from the first moment velocity map in Figure 3.1b.

Kinematic patterns like those seen for GM Aur are difficult to identify in the maps in Figure 5.1, since spatial resolution and the angular size of circumstellar emission are similar ($\sim 2''$). Features that appear to be resolved could be spurious, because the intensity of extended emission is comparable to the rms noise in the map. As a result, correlations of the maps in Figure 5.1 with those generated by a kinematic model are not as useful as they might be. Nevertheless, the technique serves as an additional check on interpretations derived from simpler analyses, and can perhaps indicate a range of parameters consistent with the data.

Unlike the situation for the larger disk around GM Aur, the P.A. of elongation, Θ_{CO}, the systemic velocity, V_{sys}, and the outer radius, R_{out}, for RY Tau cannot be determined from the emission morphology alone, since kinematic patterns are unresolved in the synthesized beam. One solution is to include them as free parameters with the centrifugal radius R_{disk}, central mass M, and inclination angle i. Here, a model of a rotating disk was cross-correlated with the data while varying the parameters $M, i, \Theta_{CO}, V_{sys}$, and R_{out}. The best-fit values of Θ_{CO}, V_{sys}, and R_{out} were then used in a second iteration of model-fitting over a range of values for R_{disk}, M, and i. The best-fit value for Θ_{CO}, 10°, is consistent with the velocity gradient in Figure 3.1b and with measurements of the linear polarization of optical emission (Bastien 1982). The best-fit systemic velocity, $V_{sys} = 7.25$ km s^{-1} (V_{LSR}), agrees with estimates of RY Tau's velocity based on optical spectra, 7.7 ± 2.4 km s^{-1}, (Hartmann *et al.* 1986) and with visual inspection of the spectrum in Figure 3.5. The estimate for the outer radius, $R_{out} = 200$ AU, agrees with the half-maximum value, $R_{HM} = 167$ AU, obtained by Gaussian fitting to the integrated emission and implies that any disk around RY

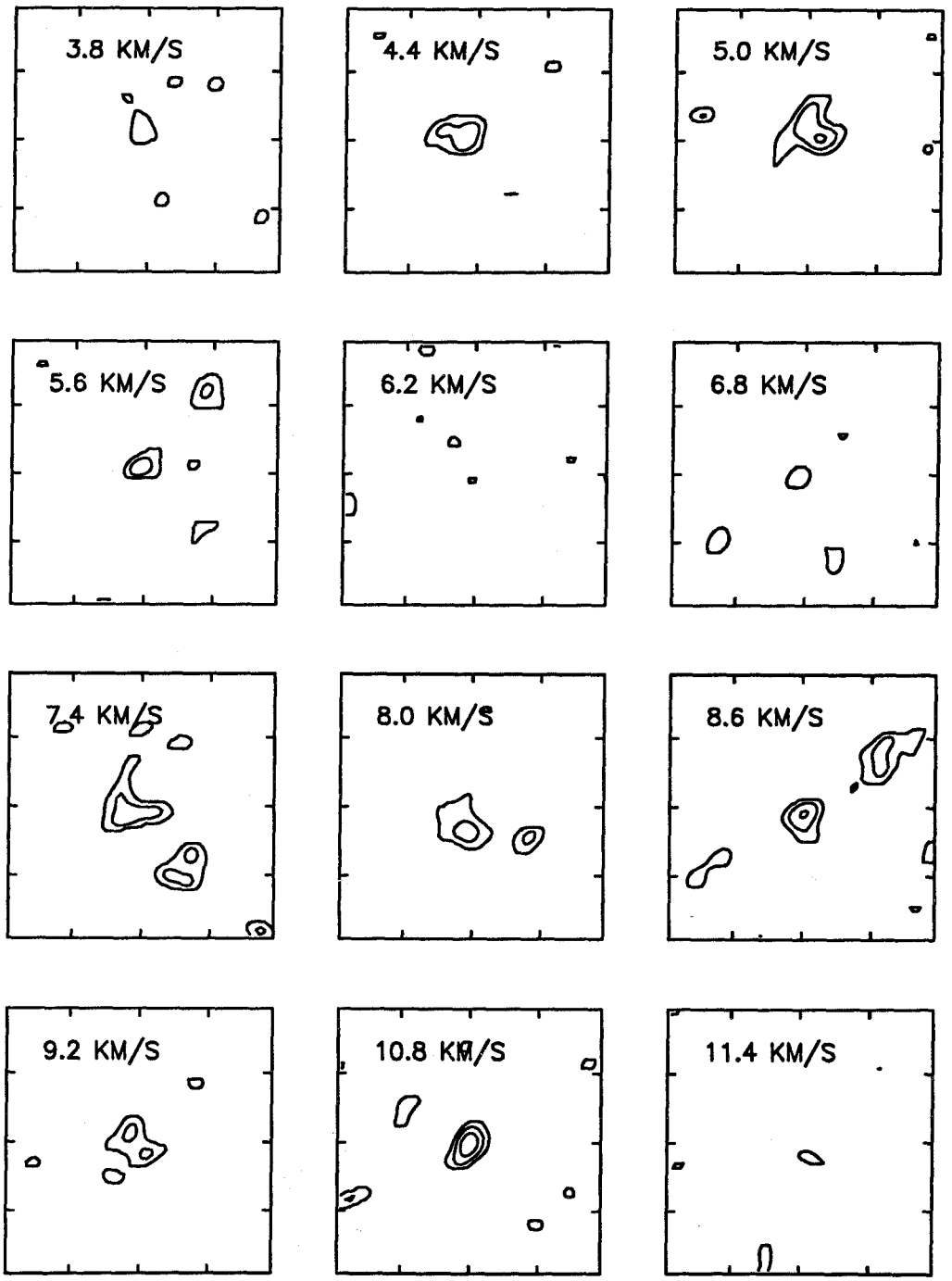

Figure 5.1. Aperture synthesis maps of CO (2→1) emission from RY Tauri at velocity intervals of $\Delta V = 0.6$ km s^{-1}. Tick-marks are placed at 5″ intervals; the (0,0) position is the map phase center and stellar position from Table 3.1. Proceeding from left to right and top to bottom, map velocities start at $V_{LSR} = 3.8$ km s^{-1} and cover a range of $\Delta V = 7.2$ km s^{-1}. Contours are spaced at the 1 σ level, 180 mJy, and begin at 2 σ.

Tau is somewhat truncated.

These values of $\Theta_{CO}, V_{sys}, R_{out}$, and R_{HM} were used in a cross-correlation between the kinematic model described in Chapter 4 and the aperture synthesis maps of RY Tau, shown in Figure 5.1, for a wide range of values of the parameters R_{disk}, M, and i. Contour maps of the correlation coefficient χ, as a function of M and i, are shown for discrete values of R_{disk} in Figure 5.2. For all maps, χ rises steeply to a broad plateau of ~ 0.5 but fails to narrowly constrain values of the central mass and inclination angle. The maximum value of χ in each of the contour maps is plotted for respective values of R_{disk} in Figure 5.3. For the most part, χ monotonically increases with R_{disk} and reaches a maximum at $R_{disk} \approx R_{out}$, implying that the observations are best fit by a rotational velocity field. The range of variation is about 8% of the maximum value of χ, but the curve flattens out for $R_{disk} > 125$ AU, so that a purely rotational model is not completely mandated by the model fit. A partial infall component cannot be strictly excluded, but the overall low value of χ prevents any real assessment of its magnitude.

The best-fit values for R_{disk}, M, and i are 175 AU, 1.25 $M_{\odot}$, and 60°, respectively. This value of the centrifugal radius, R_{disk}, matches R_{HM} (Chapter 3), but falls just short of R_{out}. There is little significance in this discrepancy; χ differs little if $R_{disk} = R_{out}$. However, it suggests that an element of infall could be present in molecular gas that is otherwise centrifugally supported. The estimate for M is lower than the stellar mass estimate, $1.69 M_{\odot}$ (Beckwith *et al.* 1990). Both mass estimates are uncertain, but recent models of the convective tracks of pre-main-sequence stars revise M_* upward to as high as 2–2.5 $M_{\odot}$ (d'Antona & Mazzitelli 1993), increasing the disparity. At first glance, this result suggests the breakdown of a model assumption which requires nearly all mass to be concentrated in a central point. It can be seen from Figure 5.2, however, that $2\ M_{\odot} < M < 2.5\ M_{\odot}$ is an acceptable range for M

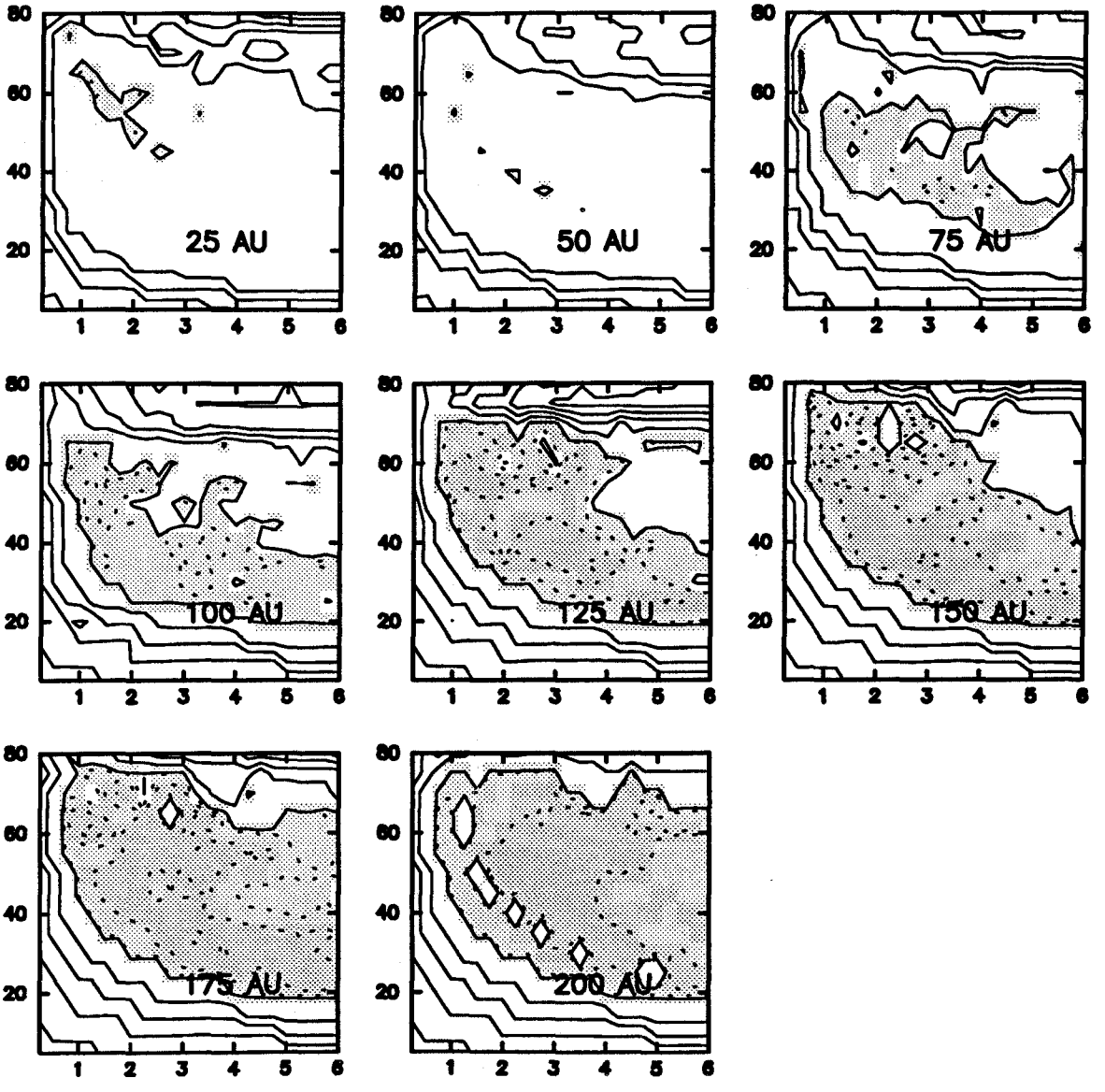

Figure 5.2. Contour maps of the correlation coefficient, χ, as a function of the central mass M and the inclination angle i of a model disk. Solid contour levels are at 10% of the maximum attainable value of χ (1.0) and dotted contours are at 1% intervals, starting at 0.5. Grey scale values begin at 0.5 and identify the maximum values of χ. From left to right and top to bottom, plots are displayed for discrete values of the centrifugal radius R_{disk} at intervals of 25 AU in the range 25AU $\leq R_{disk} \leq$ 200 AU. Closed contours in the upper left hand corner of the penultimate map (R_{disk} = 175 AU) identify the best-fit parameter values, 1.25 $M_{\odot}$ and 60°, for M and i, respectively. However, it is evident that these are not well constrained.

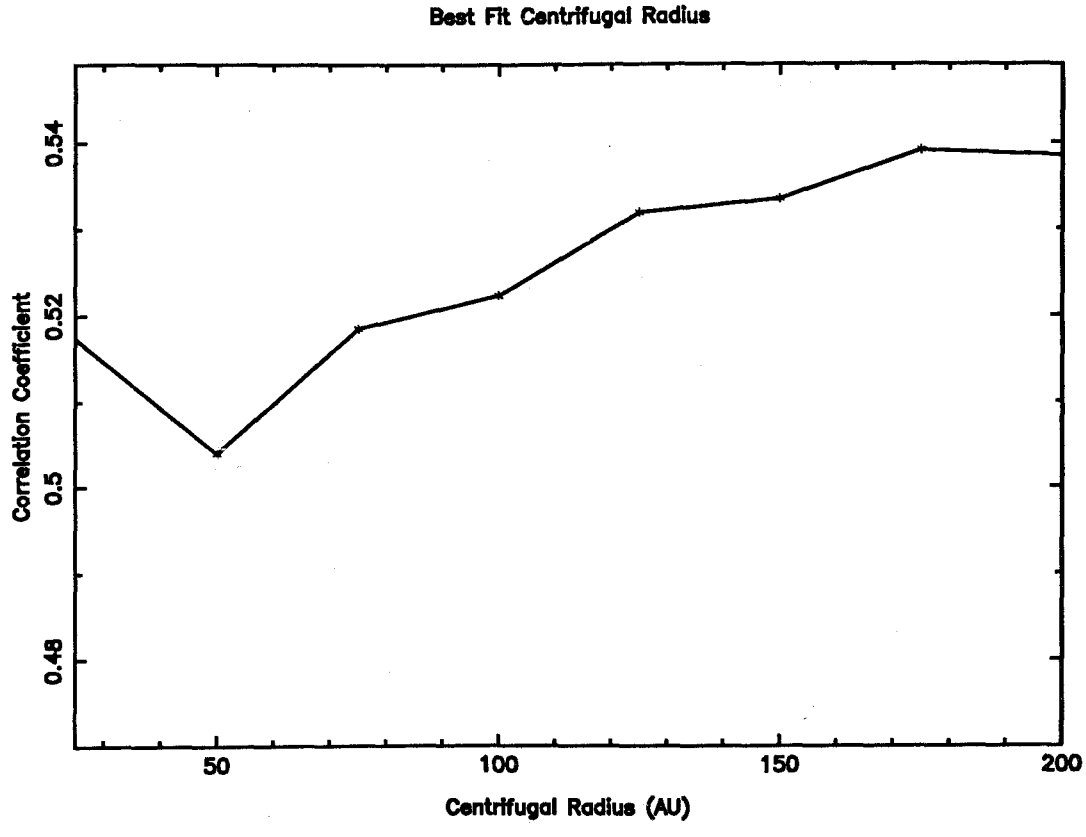

Figure 5.3. Plot of the maximum value of χ in each contour plot in Figure 5.2. The curve slopes upward and peaks at 175 AU, suggesting that circumstellar gas around RY Tau is predominantly in a state of rotation, but the differences in χ are likely to be of only marginal significance, due to the lack of spatial resolution in the observations.

on kinematic grounds, since χ has a local maximum in this region of parameter space with amplitude very close to that for $M = 1.25\ M_{\odot}$.

It was pointed out in Chapter 4 that $\chi = 1$ corresponds to the cross-correlation of identical positionally aligned maps. For RY Tau, χ has reached little better than half this value. What are the implications for the reliability of the underlying model and the resulting kinematic interpretation? Although an analytic formulation for the "goodness-of-fit" does not exist for cross-correlation, a qualitative check is afforded by inspecting the aperture synthesis maps simulated using the parameter values for which χ is maximized. Synthetic aperture synthesis maps, generated from the kinematic model with $R_{disk} = 175$ AU, $M = 2.25\ M_{\odot}$, and $i = 60°$, are presented as contour maps in Figure 5.4. The contours are superposed on a grey scale representation of the RY Tau observations. The distribution and intensity of emission in the synthetic spectral line maps approximately match the greyscale images. The beam-like morphology of model emission confirms that radiation from a disk with the asssigned parameters is unresolved. The apparent elongation of closed contours is entirely the result of beam convolution; the elongation direction of the disk is nearly perpendicular to this.

In general, the correspondence between the model and observations is quite good in the immediate vicinity of the star. However, much emission is apparent outside this region and is not fit by the kinematic model. This emission shows random structure from map to map and is less likely to emanate from truly circumstellar gas than from the ambient cloud. Possible exceptions are evident in maps at velocities 7.4 km s^{-1} and 8.6 km s^{-1}. Off-center emission at 8.6 km s^{-1} shows a linear trend perpendicular to the elongation axis, Θ_{CO}, as might be expected for gas entrained in an outflow. Emission in the map closest to the systemic velocity, on the other hand, is parallel to Θ_{CO} as might be expected for infalling gas from flattened outer regions

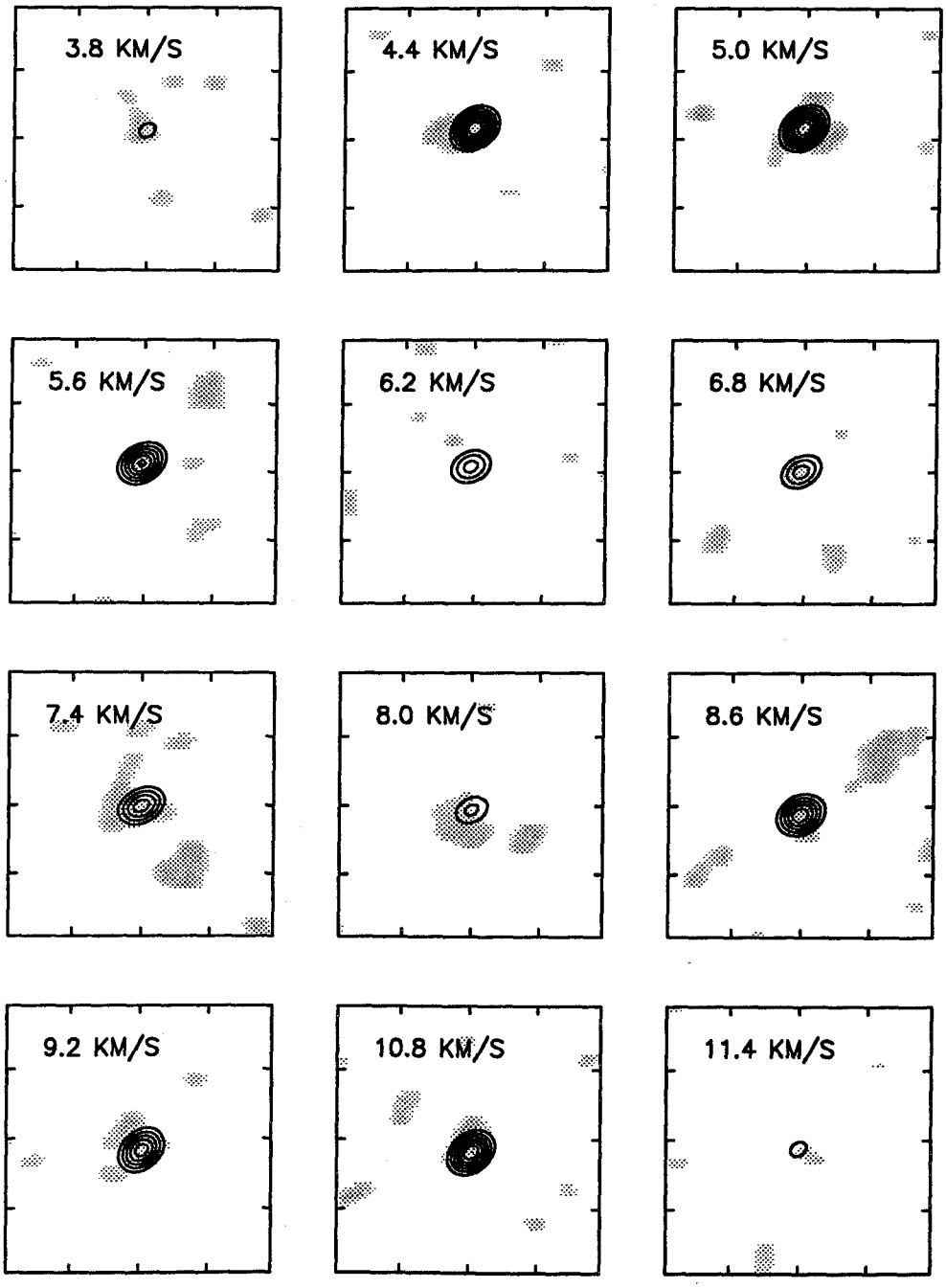

Figure 5.4. Contour maps of a model of RY Tau's circumstellar emission superposed on a greyscale representation of the aperture synthesis maps seen in Figure 5.1. Model parameters, R_{disk} = 175 AU, M = 2.25 $M_{\odot}$, and i = 60°, were chosen as the best-fitting parameters that also satisfy a central mass constraint. The apparent elongation of closed contours is entirely the result of beam convolution; the elongation direction of the disk is nearly perpendicular to this. It can be seen that model emission is largely unresolved, but peak intensities and positions have been fit to best match those of the data. Off-center emission contributes to a low overall value of χ.

(compare with Figure 4.2). Thus, this off-center emission *qualitatively* confirms the model even though it also lowers χ.

The visual agreement between central emission in observed and simulated maps in Figure 5.4 provide additional evidence that the molecular gas around RY Tau is centrifugally supported. The low value of χ is probably an effect of off-center emission and not a poor match between circumstellar emission and the model. Observations at higher spatial resolution are still necessary, however, to identify kinematic patterns unequivocally and render this conclusion incontrovertible.

3. DL Tau

In Figure 5.5, spectral line maps of CO(2→1) emission from DL Tau are displayed at velocity intervals of $\Delta V = 0.11$ km s^{-1}. The map with the most blue-shifted velocity, $V_{LSR} = 6.5$ km s^{-1}, appears in the upper left corner. Remaining maps are ordered as in Figure 5.1 and cover a velocity range of $\Delta V = 1.2$ km s^{-1}. If this narrow velocity width is due to Keplerian rotation or free-falling gas, the central mass must be small or the orientation face-on. A stellar mass of 0.56 $M_\odot$ is estimated for DL Tau from fits to evolutionary tracks in the H-R diagram (Beckwith *et al.* 1990). This mass estimate is highly model-dependent and must be viewed with even more caution than that for RY Tau, since stellar models show greater uncertainty with decreasing mass (cf. d'Antona & Mazzitelli 1993). If accurate, it argues against an edge-on orientation for DL Tau, in contrast to the elongation suggested in Fig. 5.5. Higher spatial resolution is needed to take full advantage of correlation with a kinematic model and sharply constrain the stellar mass of DL Tau, but positional shifts of peak emission and small variations in morphology justify an attempt to find a narrowed range of kinematic parameters consistent with the data.

The orientation of circumstellar gas around DL Tau is reasonably well constrained; for the modeling described below, Θ_{CO} was set to 84°, as suggested by all

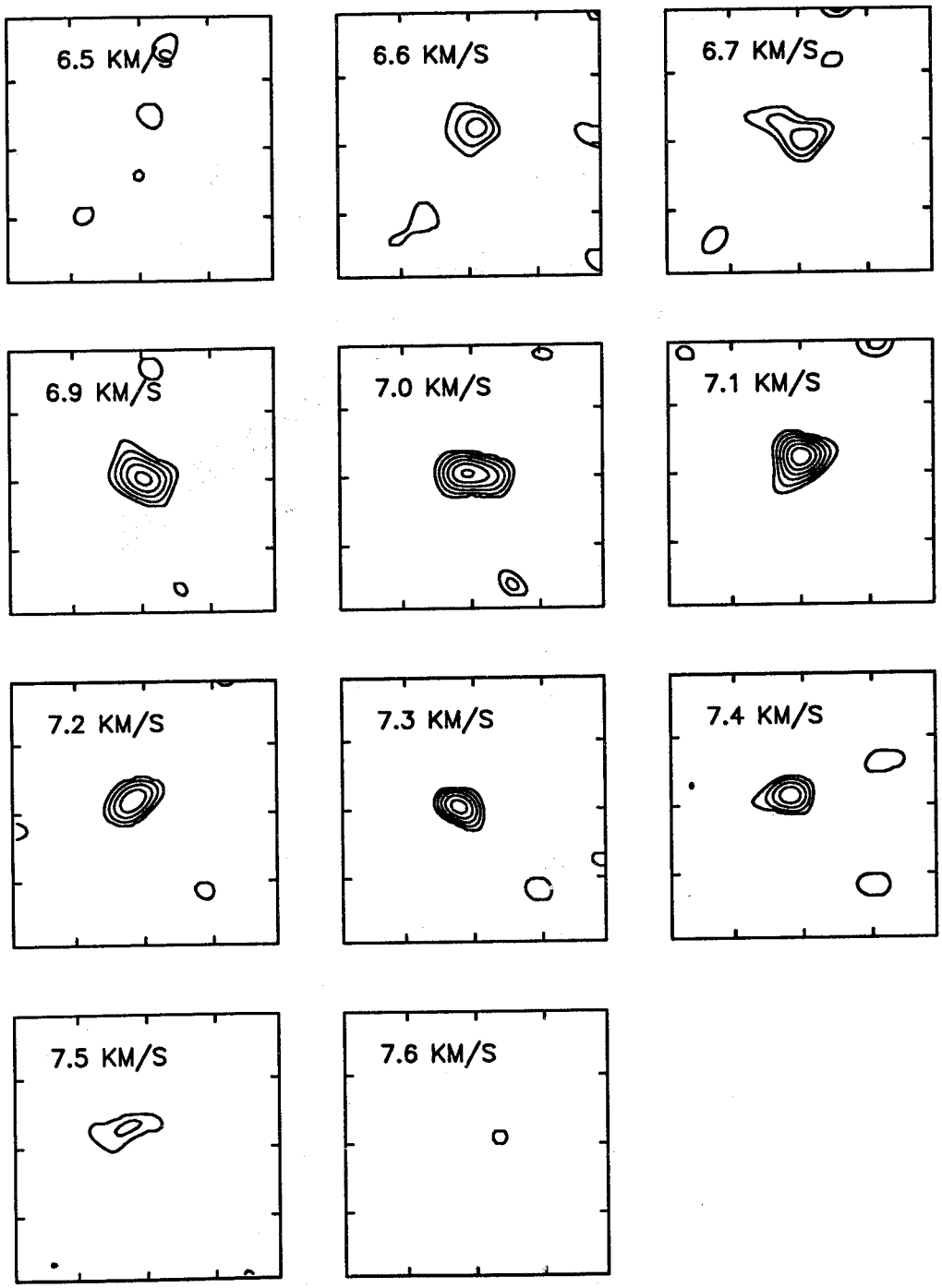

Figure 5.5. Aperture synthesis maps of CO (2→1) emission from DL Tauri at velocity intervals of $\Delta V = 0.11$ km s^{-1} with tick-marks at 5″ intervals. Maps are ordered as in Figure 51, starting at $V_{LSR} = 6.5$ km s^{-1} and covering a range of $\Delta V = 1.2$ km s^{-1}. Contours are spaced at the 1 σ level, 100 mJy, and begin at 2 σ. Peak positions shift several arcseconds predominantly along PA 84°.

three independent diagnostics listed in Table 3.2. Insufficient spatial resolution precluded accurate determination of V_{sys} and R_{out} from morphology alone; these were left as free parameters in an initial iteration carried out as described for RY Tau. The best-fit values, $V_{sys} = 7.1$ km s^{-1} and $R_{out} = 250$ AU, were then used in a second iteration of model-to-data cross-correlation, as described in Section 5.2, encompassing a wide range of values for the parameters R_{disk}, M, and i.

The results of cross-correlation between a kinematic disk model and the spectral line maps of DL Tau are shown in Figures 5.6–5.7. Peak values of χ are higher than for RY Tau (~ 0.65) and occur predominantly at values for the central mass that are lower than the 0.56 $M_{\odot}$ estimate of Beckwith *et al.* (1990). Contour maps of χ are plotted in Figure 5.6 as a function of M and i for discrete values of the radius of a centrifugally supported region. They reveal broad regions of parameter space with $\chi > 0.6$ in each map. Although χ is not sharply peaked for any set of parameter values, a local maximum is found in every map for M and i values of approximately 0.1 $M_{\odot}$ and 65°, respectively. The area of (M, i) parameter space with $\chi > 0.64$ increases markedly with increasing R_{disk}, suggesting that gas is centrifugally supported, but the maximum value in each map changes little. Thus, a preferred value of the centrifugal radius is not strongly apparent in Figure 5.7, but the sequence of contour plots in Figure 5.6 favors rotation. The most likely kinematic interpretation consistent with maxima in χ is that circumstellar gas resides in a nearly edge-on disk rotating around a very low mass star, but there is no compelling reason to prefer rotation over infall on the basis of model-fitting described here.

Contour maps of emission from a model using the best-fit parameters, $R_{disk} = 200$ AU, $i = 75°$, and $M = 0.25$ $M_{\odot}$, are shown in Figure 5.8 overlaid on grey scale maps of the CO(2→1) emission from DL Tau. The synthetic maps and observations agree well. Again, however, very little spatial information is available at the 3″ resolu-

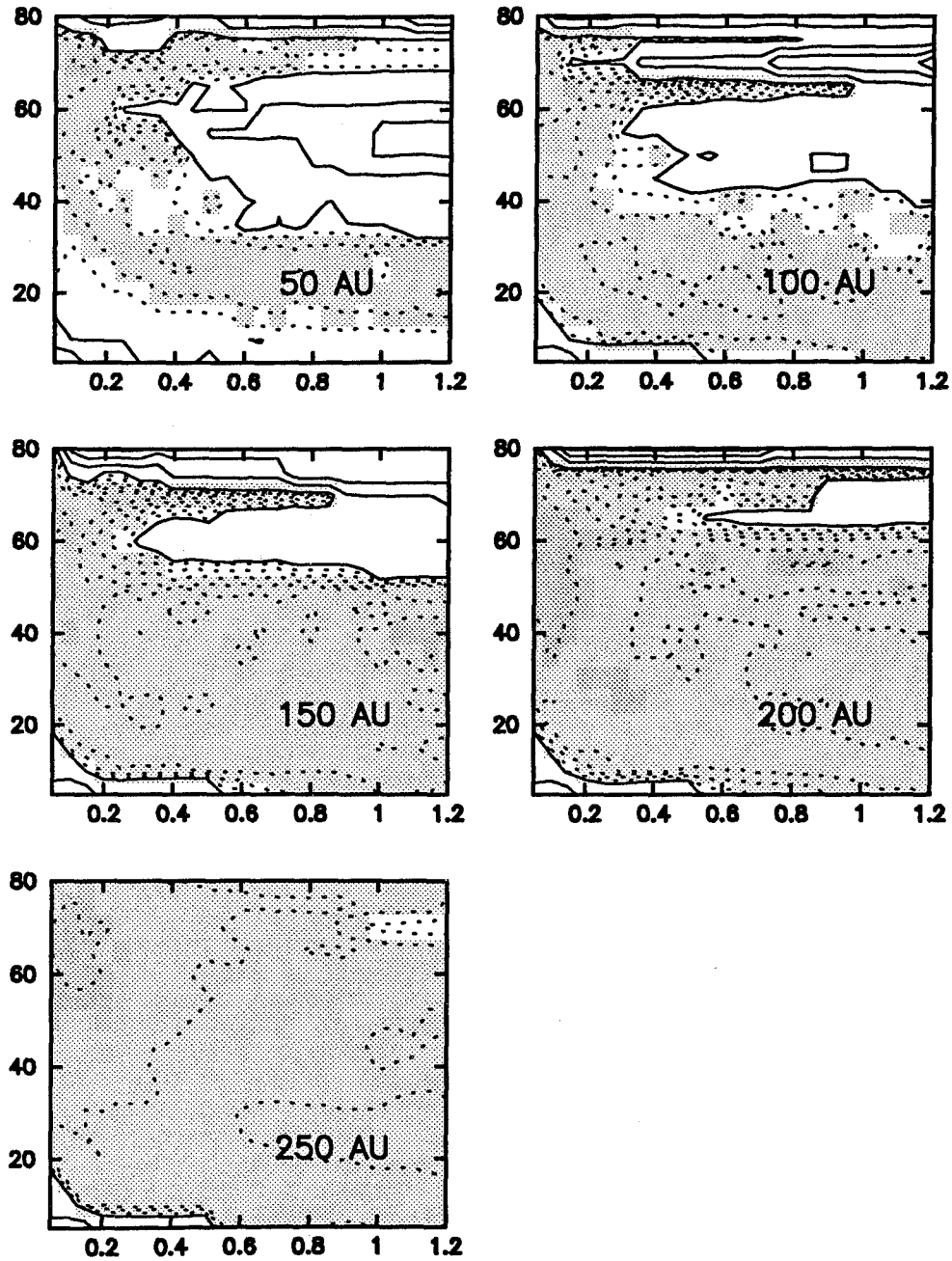

Figure 5.6. Contour maps of the correlation coefficient, χ, as a function of the central mass M and the inclination angle i of a model disk. Solid contour levels are at 10% of the maximum attainable value of χ (1.0) and dotted contours are at 1% intervals, starting at 0.6. Grey scale values begin at 0.6 and identify the maximum values of χ. As in Figure 52, plots are displayed for discrete values of the centrifugal radius R_{disk}, but at larger intervals of 50 AU in the range 50AU $\leq R_{disk} \leq$ 250 AU. Plots exhibit successively larger areas of parameter space with $\chi > 0.6$ as R_{disk} increases, suggesting rotation. The maximum value of χ in each map is encompassed by closed contours in the upper left hand corner of each map. The best-fit parameter values occur in the penultimate map ($R_{disk} = 200$ AU) at 0.25 $M_{\odot}$ and 75°.

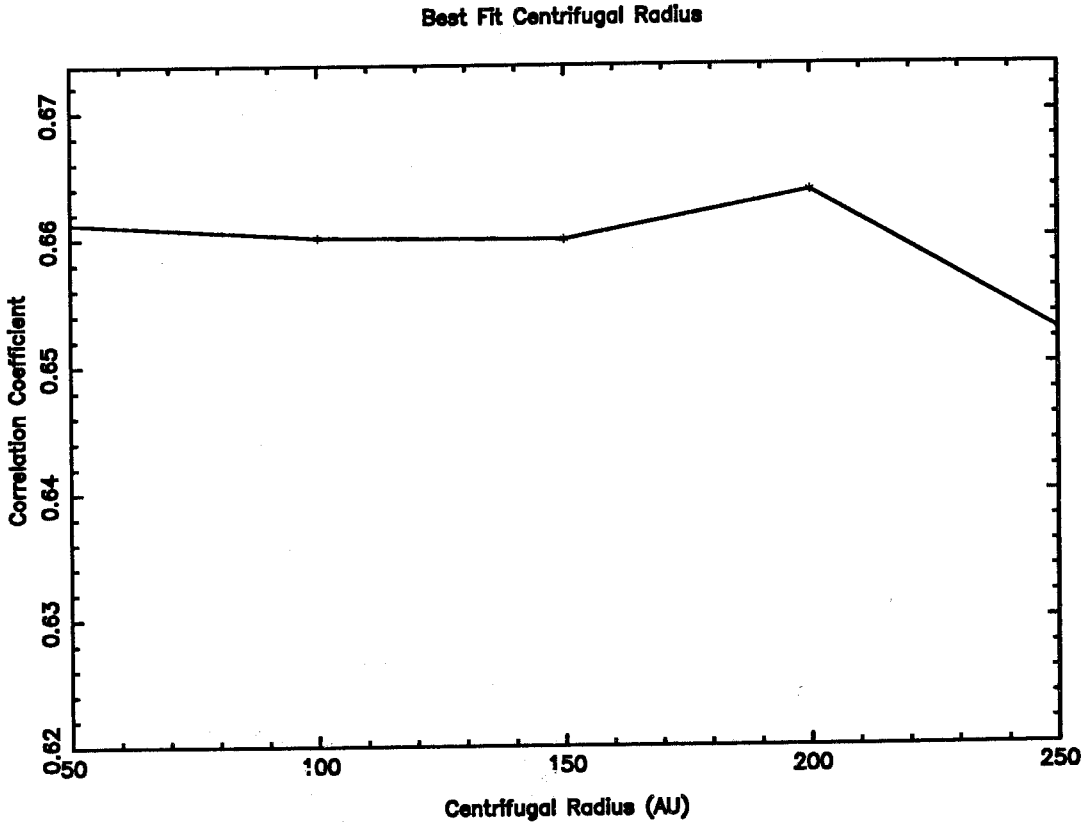

Figure 5.7. Plot of the maximum value of χ with respect to the centrifugal radius. The best-fit value occurs near the outer edge of the disk, suggesting that circumstellar gas is predominantly centrifugally supported, but the curve is largely flat and fails to narrowly constrain the centrifugal radius.

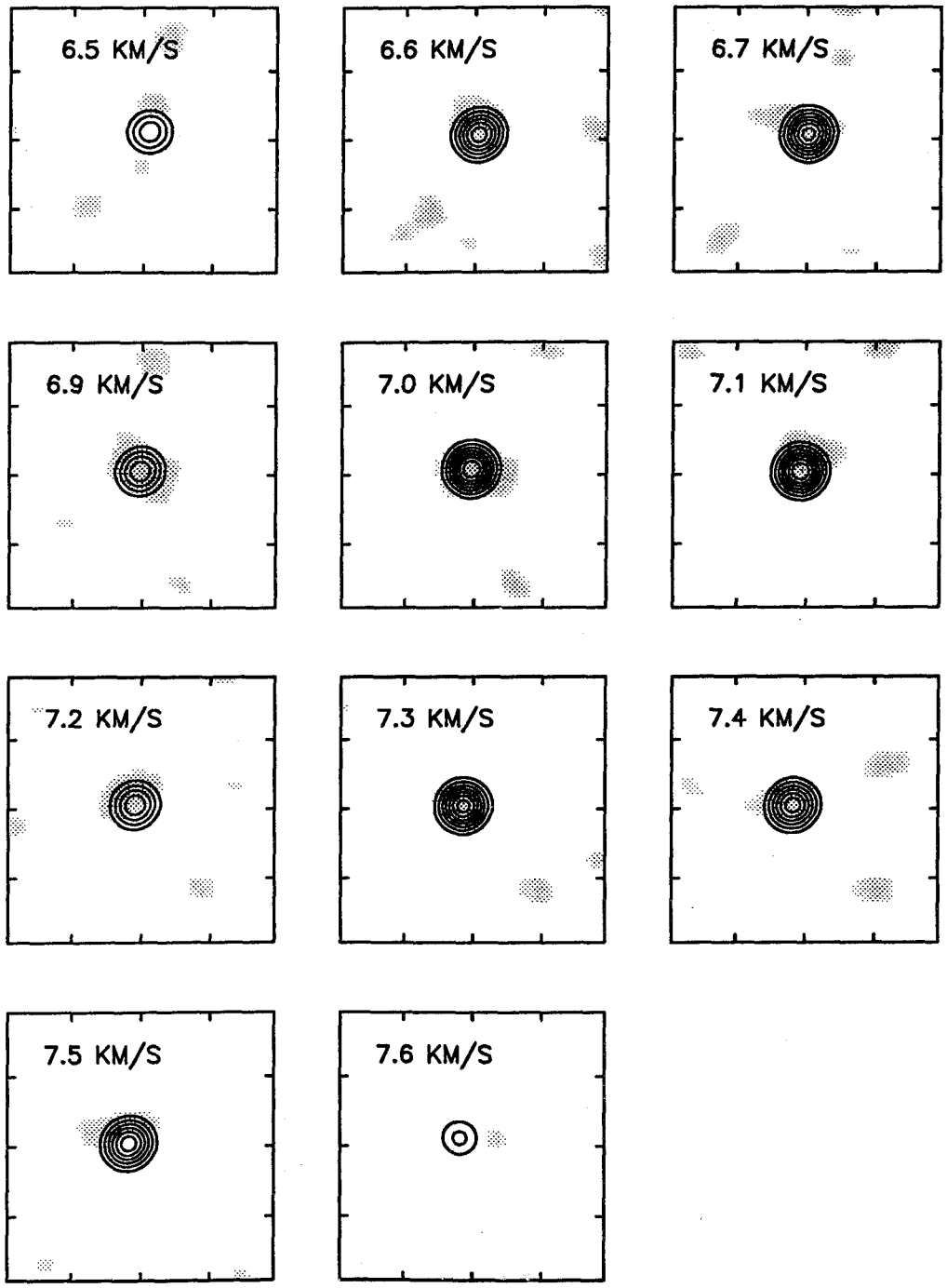

Figure 5.8. Contour maps of a model of DL Tau's circumstellar emission superposed on a greyscale representation of aperture synthesis maps seen in Figure 5.5. Best-fit model parameters used in the simulation are $R_{disk} = 200$ AU, $M = 0.25\ M_{\odot}$, and $i = 75°$. It can be seen that model emission is unresolved in the nearly circular beam.

tion. The morphology of model emission is completely dominated by the synthesized beam, and systematic offsets of peak positions from map to map are of similar magnitude to spatial differences between peaks in the observed and model emission. These factors severely limit what can be achieved by modeling of kinematic patterns, and the question of rotation versus infall can be addressed only crudely. Yet, the results for DL Tau demonstrate that a centrifugally supported disk interpretation is most consistent with the molecular line observations, as suggested by moment maps and PVDs.

4. DO Tau

Molecular line emission detected from DO Tau is distributed over a region of larger angular extent than that from RY Tau or DL Tau. Correspondingly more detail can be seen in maps of the CO($2 \rightarrow 1$) emission. Consequently, this object holds greater promise for successful analysis using a model of the line emission morphology. The first moment velocity maps (Figures 3.1b-4b) and spectra (Figure 3.5) for DO Tau differ markedly from those for the other two sources. Peak intensity is an order of magnitude larger than for DL Tau, but lies at blue-shifted velocities outside the bandwidth covered by the high-resolution spectrometer setting. It is unlikely that most of this emission derives from centrifugally-supported gas, since it appears at velocities that would require a central mass of approximately 15 $M_{\odot}$. There is no comparison between this and the stellar mass estimate of 0.7 $M_{\odot}$ or the mass of circumstellar material estimated from $\lambda = 1.3$ mm dust continuum emission, 0.018 $M_{\odot}$ (Beckwith *et al.* 1990). Emission in the narrow high-resolution bandwidth, however, is observed at velocities close to the radial velocity of DO Tau and is more likely to characterize the circumstellar kinematic signature; fortuitously, this emission is isolated from blue-shifted radiation by a prominent spectral dip (see Figure 3.5).

Spectral line maps of CO($2 \rightarrow 1$) emission from DO Tau are displayed in Figure

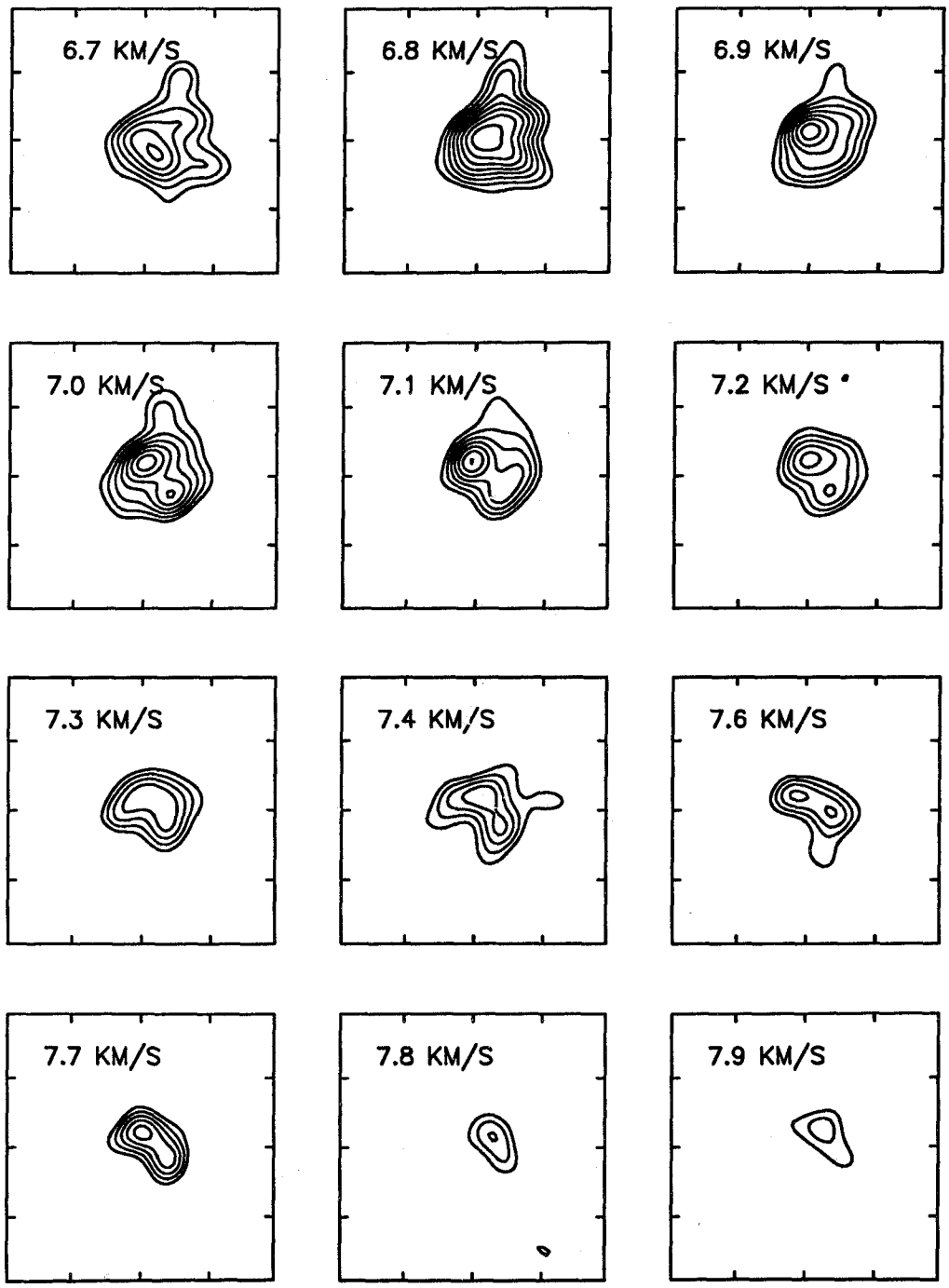

Figure 5.9. Spectral line maps of CO(2→1) emission as in Figs. 5.1 and 5.5, but for DO Tau. Velocity intervals are $\Delta V = 0.11$ km s^{-1} and over the velocity range of peaked emission observed in the high-velocity-resolution band, $\Delta V = 1.7$ km s^{-1}. The far blue-shifted velocity is at $V_{LSR} = 6.7$ km s^{-1}.

5.9 for the narrow velocity range of emission found in the high-velocity-resolution band, $\Delta V = 1.7$ km s^{-1}, and at velocity intervals $\Delta V = 0.11$ km s^{-1}. Ordering is as in previous figures with the map at the far blue-shifted velocity, $V_{LSR} = 6.7$ km s^{-1}, in the upper left corner. Emission is clearly resolved and systematic trends are evident; morphological patterns vary smoothly from map to map at a rate acceptable for circumstellar gas. Peak intensities are not symmetric about some central velocity, but decrease with increasing velocity. The centroid of emission integrated over the narrow velocity interval is offset to the NW from both the stellar position and that of the total integrated line emission. Little or no emission was dectable at the velocities corresponding to the minimum in DO Tau's spectrum (Figure 3.5). This minimum occurs at ~ 6 km s^{-1}, the velocity of the Taurus dark cloud, and is probably caused by absorption by foreground molecular material, since DO Tau is located in a particularly dense region (cf. Ungerechts & Thaddeus 1987).

One possible interpretation is that maps in Figure 5.9 correspond to the red-shifted portion of a sequence of spectral line maps from purely circumstellar gas. In this picture, the blue-shifted half of circumstellar emission is confused by ambient cloud emission and possible self-absorption. The positional offset of red-shifted maps implies that gas rotates with a receding side to the NW. In contrast to GM Aur, it is not immediately apparent from comparison of DO Tau with typical synthetic maps such as in Figures 4.1 and 4.2 that the observed patterns correspond to rotation alone. To explore the possibility that gas is in a combined state of infall and rotation within the confines of a circumstellar disk around DO Tau, simulations of the spectral line maps have been cross-correlated with aperture synthesis maps, as described for RY and DL Tau.

The discovery of an optical jet from DO Tau (Hirth *et al.* 1994) eliminates the need to vary Θ_{CO} as a free parameter, assuming that the jet is directed normally

with respect to the plane of the disk. The direction of elongation derived in this way, $\Theta_{jet} + \pi/2 = 160°$, agrees with polarization measurements (Bastien 1982) and observed elongation of CO emission in Figure 3.3. Comparison of synthetic maps from kinematic models and Figure 5.9 indicates that the systemic velocity, V_{sys}, is approximately 7.0 km s^{-1}. The three maps around this velocity in Figure 5.9 show inner double lobed structure approximately perpendicular to the elongation axis as in Figures IV.1–4. The radial extent of emission in some maps also indicates that circumstellar CO is present well outside the half-power radius (R_{HM} = 357 AU) derived from Gaussian fits. This information narrows the range over which it is necessary to vary V_{sys} and R_{out} as free parameters. Preliminary cross-correlation over a range of V_{sys}, R_{out}, M, and i yields V_{sys} = 6.9 km s^{-1} and R_{out} = 500 AU for DO Tau. These values were used in a second iteration over more finely gridded values of R_{disk}, M, and i, discussed below.

Results of the cross-correlation of DO Tau spectral line maps with those generated by a kinematic model are shown in Figures 5.10 and 5.11 and contrast favorably with those for RY and DL Tau. The maximum value of χ ($\sim$ 0.84) is substantially higher and visibly more peaked in contour maps, yielding best-fit parameter values for M and i of 1.6 $M_\odot$ and 30°, respectively. Although both parameters are better constrained than in the earlier examples, the range of acceptable values for M is broader than that for i, judging by the shape of highest contours. For R_{disk} = 350 AU, χ is still within 1% of its maximum value when M and i take on the values 0.7 $M_\odot$ and 40°, respectively. This estimate for M is in better agreement with combined estimates of the stellar mass and innermost disk (Beckwith *et al.* 1990). The corresponding value of i defines the orientation required for a circularly symmetric disk to appear in projection as an ellipse with semi-major and semi-minor axes in the ratio 5/4, the same as that derived from deconvolution of a Gaussian fit to DO Tau's

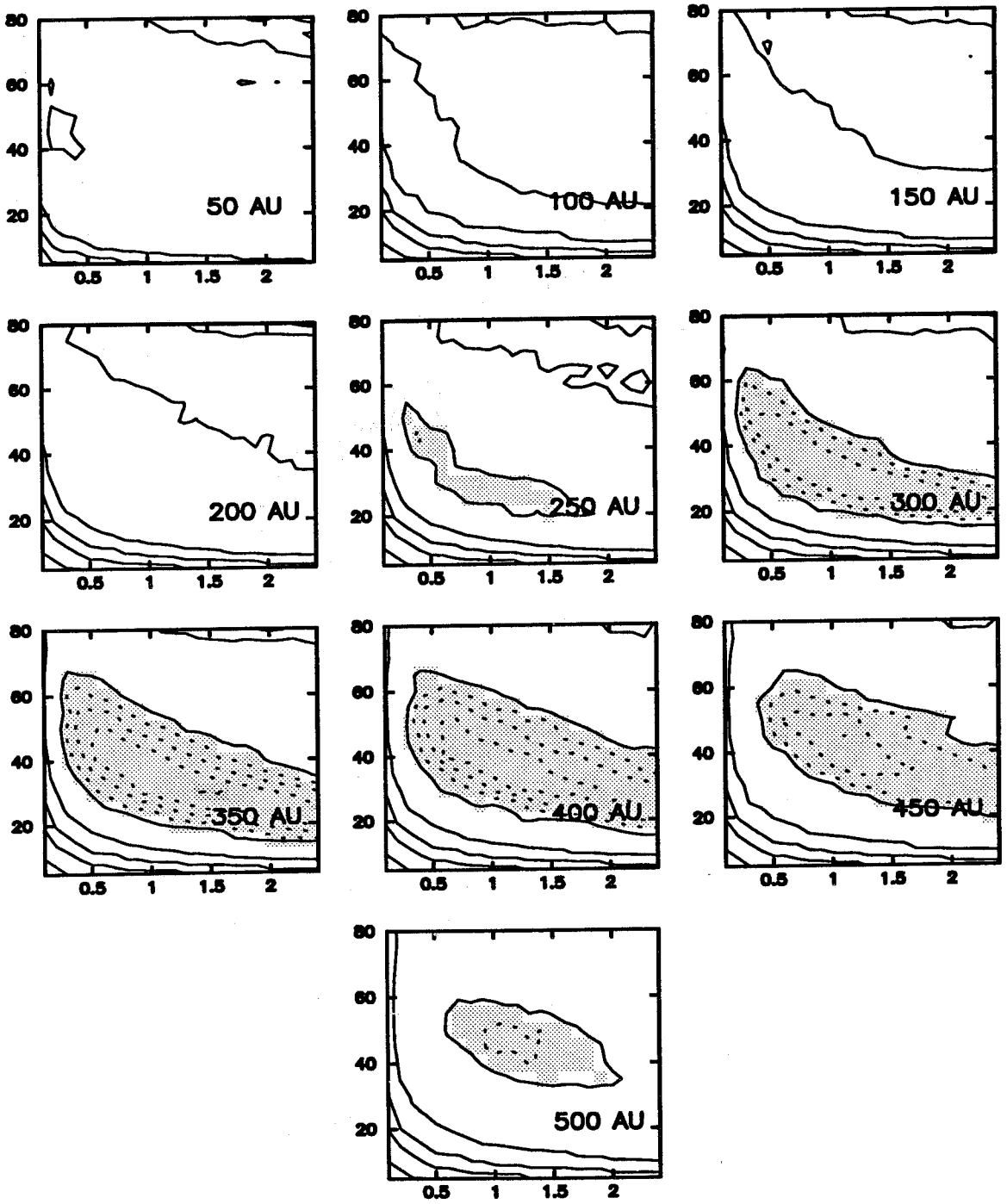

Figure 5.10. Contour maps of the correlation coefficient, χ, as a function of the central mass M and the inclination angle i of a model disk. Contour levels are as in previous figures with dotted contours and grey scale levels beginning at $\chi = 0.8$. Plots are displayed at 50 AU intervals of the centrifugal radius R_{disk}, ranging from 50 to 500 AU. The area of contours enclosing a region where χ lies within 10% of its maximum value is substantially smaller than for RY or DL Tau. Best-fit parameter values for M and i occur for R_{disk} = 350 AU at 1.6 $M_{\odot}$ and 30°.

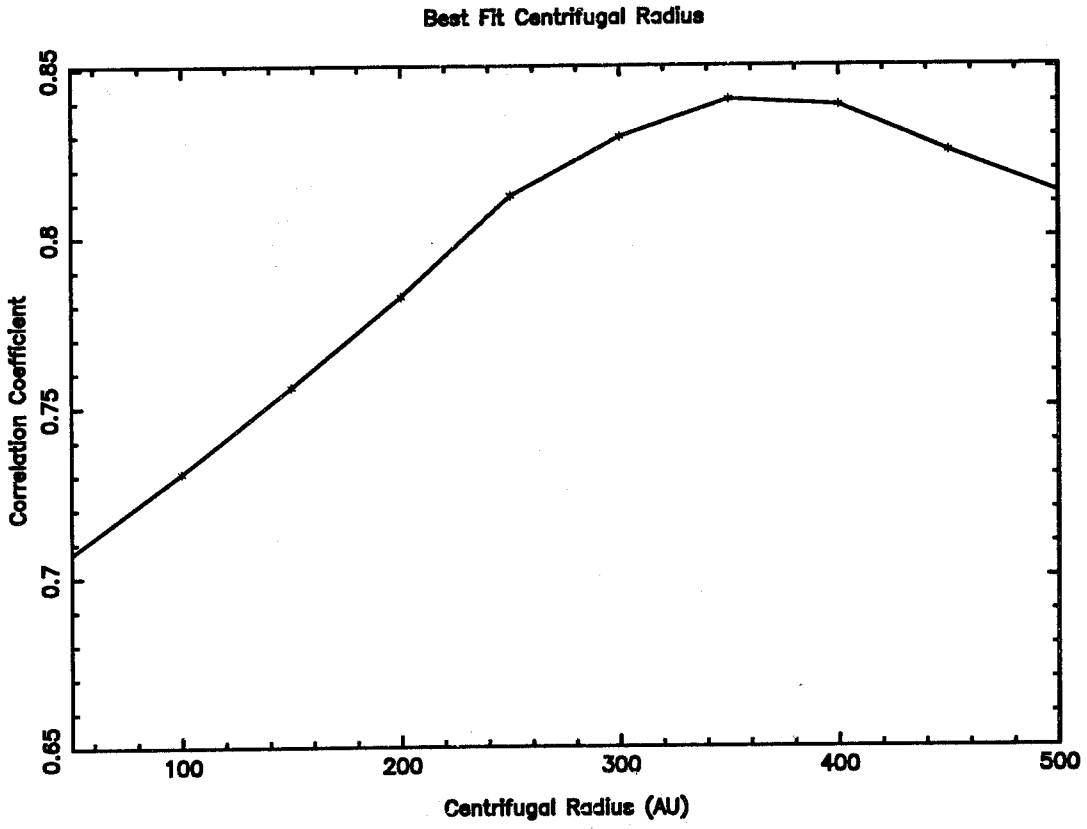

Figure 5.11. Plot of the maximum value of χ with respect to the centrifugal radius. The best-fit value occurs at R_{disk} = 350 AU, similar to the half-maximum radius of integrated emission. The correlation coefficient is strongly peaked compared to fits to RY Tau and DL Tau.

circumstellar emission (Figure 3.3a). The plot of χ with respect to R_{disk} reveals a smoothly varying function that is significantly more peaked than for either RY or DL Tau. The amplitude ranges over 15% of the peak value of χ, centered at $R_{disk} = 350$ AU $\approx R_{HM}$. When contrasted with the best-fit outer radius, $R_{out} = 500$ AU, this value strongly suggests that a substantial component of circumstellar gas is falling onto a large centrifugally supported disk.

In Figure 5.12, contour plots of model maps simulated with the use of the best-fit parameters confirm that the data are well fit by the model with $\Theta_{CO} = 160°$, $R_{out} = 500$ AU, $R_{disk} = 350$ AU, $M = 1.6\ M_{\odot}$ and $i = 30°$. Closed contours are coincident with nearly all of the observed emission, shown in grey-scale. Features are present in both observed and modeled emission that might not be easily recognized from visual inspection as kinematically significant. In particular, many of the structures in observed maps exhibit concave morphology open to the SE. This orientation is exactly opposite to that expected for emission from the NW half of a purely rotating disk. A combination of radially dependent infall and rotational velocities, however, reproduces this structure in synthetic maps. Other features duplicated by the model include a northern extension in maps near the systemic velocity and asymmetry in double lobed structure near the systemic velocity (more easily seen in Figure 5.9). All in all, it is surprising that so much agreement exists between a model of purely circumstellar emission and observations of line emission from an object which also shows molecular features at high velocities (the blue-shifted gas). To first order, confusion has not obscured a systematic kinematic pattern, but minor differences between observed and model emission are apparent. In all likelihood, model confinement of infalling gas to a planar configuration is a requirement that must be relaxed somewhat to fit these features.

In summary, molecular line maps of DO Tau show resolved structure within a

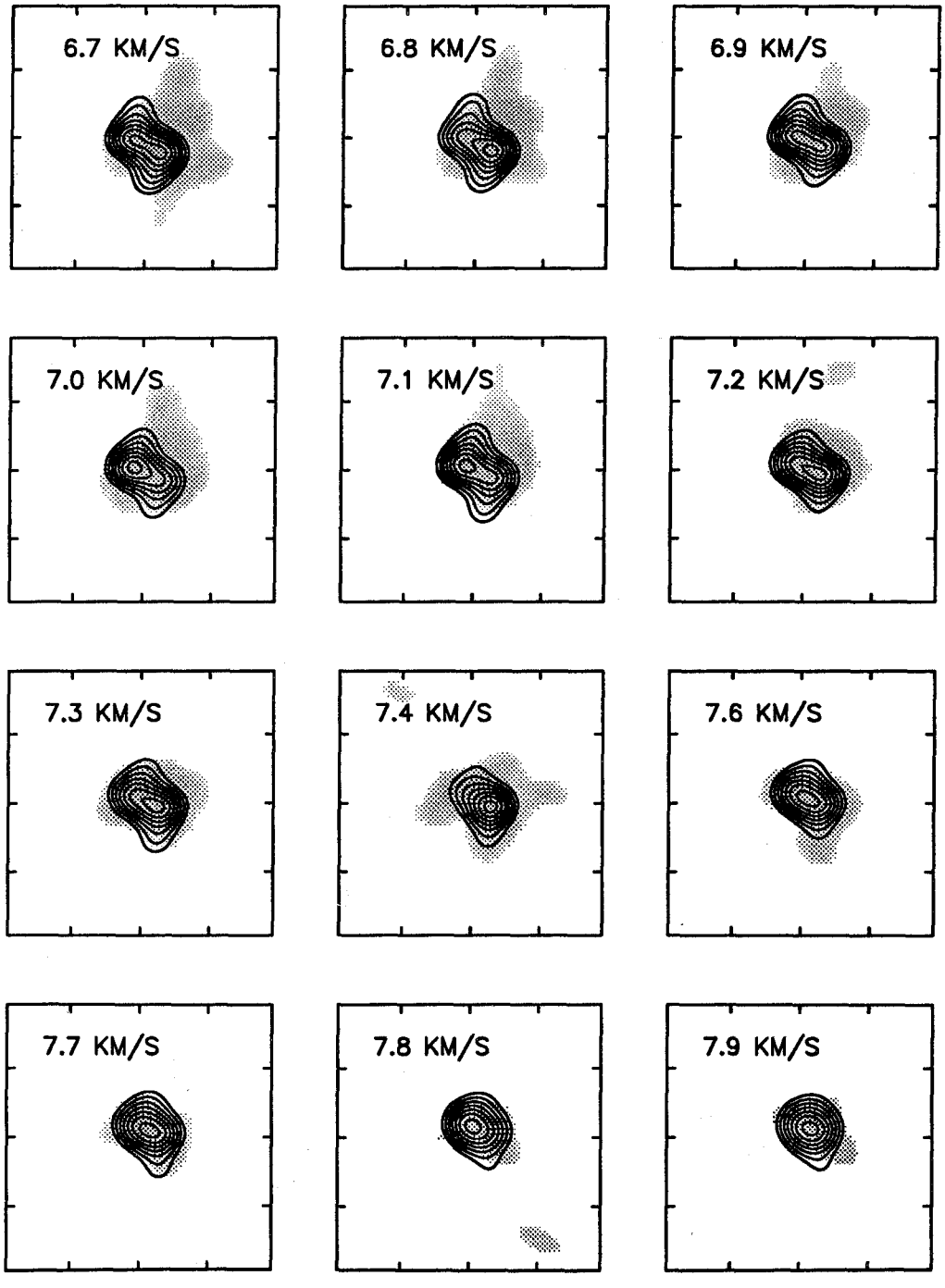

Figure 5.12. Contour maps of a model of DO Tau's circumstellar emission superposed on a greyscale representation of aperture synthesis maps seen in Figure 5.9. Best-fit model parameters used in the simulation are $R_{disk} = 350$ AU, $M = 1.6\ M_{\odot}$, and $i = 30°$. Both model and observed emission are resolved and show structure that varies systematically from map to map. Model emission duplicates the northern extension seen in the first maps, asymmetric peaks in the second row maps and arc like structure, concave to the SE, in many maps.

narrow velocity range. These exhibit systematic morphological variations that depend on velocity in such a way as to suggest a kinematic origin, but kinematic patterns are not easily identificable on the basis of visual comparison with models of rotation alone. Cross-correlation of the data with maps simulated by a combined model of infall and rotation yields more satisfactory results than for RY and DL Tau, in keeping with the better resolution of morphological features in aperture synthesis maps. Parameter estimates are more refined and suggest a strong infall component as well as centrifugally supported rotation of the circumstellar gas. Model maps duplicate observed features that are hard to account for with a rotational model alone. The preferred range for M and i includes a set of values that is simultaneously consistent with both published stellar mass estimates and a value of the inclination derived from the morphology of CO($2\rightarrow1$) emission. Most importantly, the correlation coefficient χ is strongly peaked for a value of the centrifugal radius consonant with the half-power radius of integrated emission, 350 AU. Together with a best-fit outer radius, $R_{out} = 500$ AU, this provides compelling evidence for the existence of a centrifugally supported disk around DO Tau onto which gas is still dynamically accreting.

5. AS 209

The CO($2\rightarrow1$) spectrum of AS 209 in Figure 3.5 is comparable to that of RY Tau in lineshape, width, and intensity. There is a suggestion of the double-peaked shape characteristic of circumstellar material, confirming AS 209 as a promising candidate for a protoplanetary disk system. However, the asymmetric line shape and extensions of the gas orthogonal to the elongation axis indicate that other factors, such as outflow or self-absorption, may have an effect. Further analysis is needed to establish the kinematic signature of the circumstellar gas, but detailed modeling of the aperture synthesis maps is complicated by limited spatial and velocity resolution.

The central velocity for the observations, -4.0 km s^{-1}, is the systemic velocity of

AS 209 determined from optical observations (Walter F.M., private communication). Uncertainty in this value contributed to mis-alignment of the center of the high-resolution spectrometer band with the emission peak, and much of the emission with sufficient signal-to-noise ratio for model-fitting lies outside the band. Consequently, spectral line maps for AS 209 were constructed with lower velocity resolution (1.3 km s^{-1}) than for other sources. Low source declination ($-14°$) also resulted in reduced spatial resolution in the N–S direction, since observations in only one configuration of the Owens Valley array were available. Although peak positions shift with velocity to a measurable degree, line emission is largely unresolved. Nevertheless, simulation of mapped emission from AS 209 is likely to prove instructive, even if it provides only supporting evidence of the origin of the molecular emission.

Spectral line maps of CO($2 \rightarrow 1$) emission from AS 209 are displayed in Figure 5.13 at velocity intervals of ΔV = 1.3 km s^{-1}. The extreme blue-shifted map, again in the upper left corner, is centered at V_{HEL} = -9.9 km s^{-1}, and the total velocity width represented by all 6 maps is 7.8 km s^{-1}. A disproportionate fraction of the total line intensity emits entirely from the third map at velocity V_{HEL} = -7.3 km s^{-1}, suggesting that much of the morphology variations needed to constrain kinematic interpretation lie unresolved within the velocity width of one channel. However, relative to adjacent maps, this emission is displaced and asymmetrically elongated to the SE along the PA of elongation, 136°. This shift in position and morphology supports a rotational interpretation of the gas with angular momentum vector pointing NE, as suggested by the first moment velocity map of Figure 3.4b.

A first attempt at model correlation with aperture synthesis maps in Figure 5.13 yielded a disappointing result. Maximum values of χ were obtained for best-fit parameter values that produced substantial excess emission in model maps at velocities where relatively little is found. This is largely due to the fact that the cross-

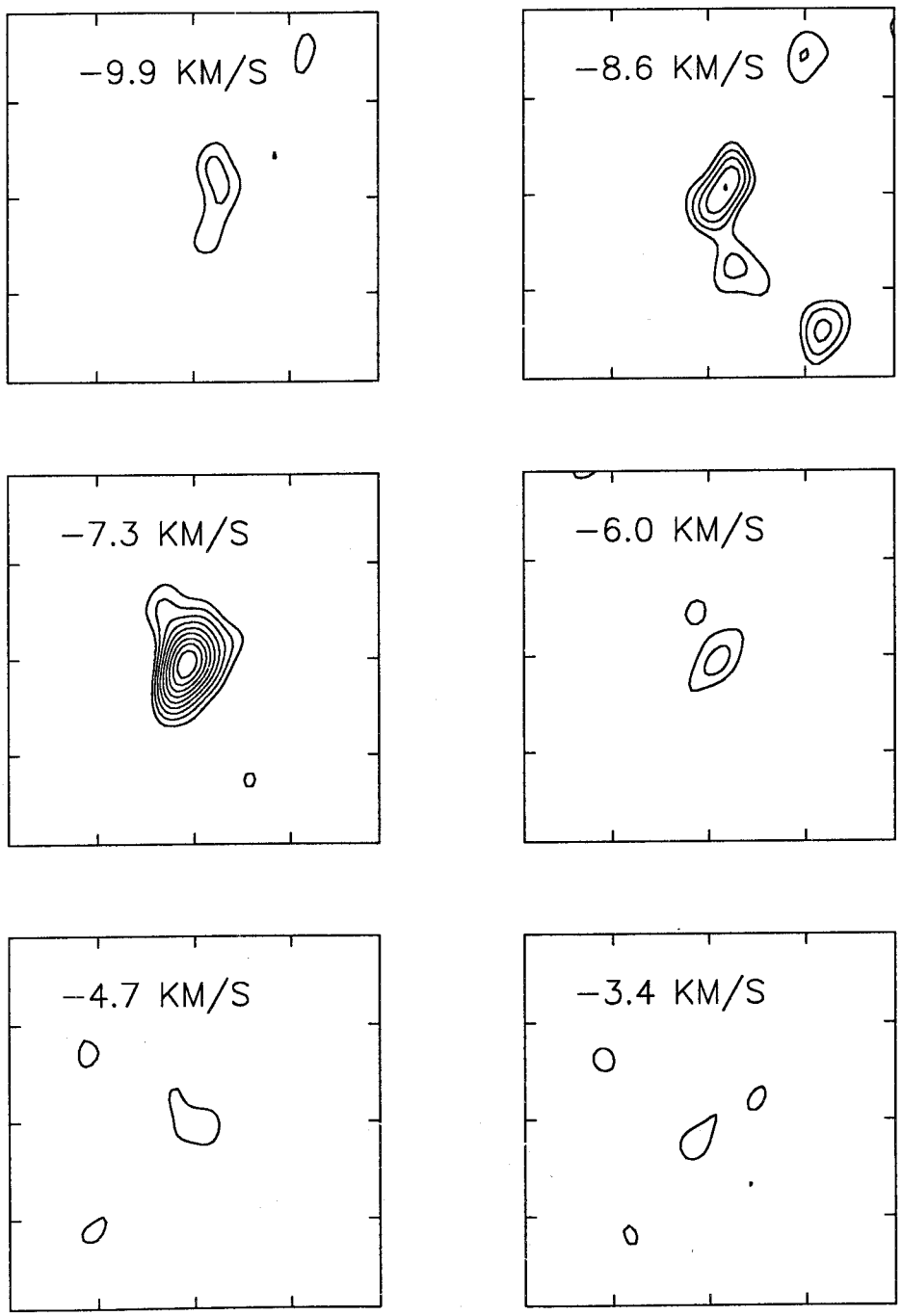

Figure 5.13. Aperture synthesis maps of CO (2→1) emission from AS 209 at velocity intervals of $\Delta V = 1.3$ km s^{-1} with tick-marks at 5″ intervals. Maps start at V_{HEL} = -9.9 km s^{-1} and cover a range of $\Delta V = 7.8$ km s^{-1}. Contours are spaced at the 1 σ level, 100 mJy, and begin at 2 σ.

correlation coefficient χ, as defined in Chapter 4, optimizes a fit of the morphology of model maps at a given velocity, but does nothing to fit the relative intensity of maps with respect to velocity. Spectral line maps of AS 209 are especially affected by this limitation because they are at the lowest spatial and velocity resolution and include the least number of maps with high signal-to-noise, adjacent to images with low-intensity centered emission at high velocities (see maps at V_{HEL} = -4.7 and -3.4 km s^{-1} in Figure 5.13). For such conditions, a merit function is needed which also constrains the relative amplitude for maps at different velocities.

The total power in an individual image provides a measure of the absolute amplitude and is easily calculated in the numerical code by summing over the discrete power spectrum as

$$P(v_k) = \sum_i \sum_j \widehat{Im_k}(u_i, v_j) \widehat{Im_k}^*(u_i, v_j) \quad ,$$

where $P(v_k)$ is the total power in the kth map with velocity v_k and $\widehat{Im_k}$ is the Fourier Transform of the corresponding image. This value depends on the absolute value of emission intensity, a quantity which in turn depends on many unknown physical parameters. For comparison between model and observed maps, *relative* amplitudes can be calculated by dividing $P(v)$ by the sum over all maps as

$$\Delta P(v_k) = \frac{P(v_k)}{\sum_k P(v_k)} \quad .$$

Here $\Delta P(v_k)$ is the the fractional power of a map at velocity v_k. This quantity provides a measure of integrated map intensity *relative to other maps* in a spectral line cube. It consitutes a merit function, independent from χ, that can be differenced for observed and model maps, then squared and minimized in a "least-squares" procedure. Unlike the cross-correlation procedure described in Chapter IV, however, this

method estimates best-fit parameters solely on the basis of a fit to the relative integrated map intensity between maps (i.e. a spectral line fit) and is unable to take account of any spatial information available in aperture synthesis maps.

For the purpose of analyzing the underlying kinematics behind the appearance of emission in low-resolution maps of circumstellar gas around AS 209, a hybrid merit function has been created which combines ΔP and χ to measure both the difference in morphology and relative amplitude between observed and model maps. For uniformity of analysis, an attempt has been made to mimic the behaviour of the previous correlation coefficient (maximization instead of minimization) with the following expression:

$$\chi' = \frac{\chi}{2\ Max(\chi)} + \frac{Min(\Delta P)}{2\ \Delta P} \quad ,$$

where χ' is the revised merit function, $Max(\chi)$ is the maximum, and $Min(\Delta P)$ is the minimum value attained by χ and ΔP, respectively, over the appropriate range of parameter space. It can be seen from the above expression that both terms on the right hand side achieve a maximum value of 0.5 when parameters take on their best-fit values independently for χ and ΔP. Thus, the maximum possible value attained by χ' is 1.0 for maps which are positionally coincident, morphologically identical, and show the same ratio of integrated intensities between maps at different velocities. This function can now be calculated, plotted, and maximized over a range of parameters in the same way as χ was for RY, DL, and DO Tau. A more satisfactory model fit to line maps of AS 209 may thus be achieved.

Maps of line emission from AS 209 were cross-correlated with those of a kinematic model in the usual way and ΔP was calculated with an added subroutine. Both χ and ΔP were written out to files along with associated parameter values. From these, $Max(\chi)$ and $Min(\Delta P)$ were derived, and χ' was calculated for plotting in the

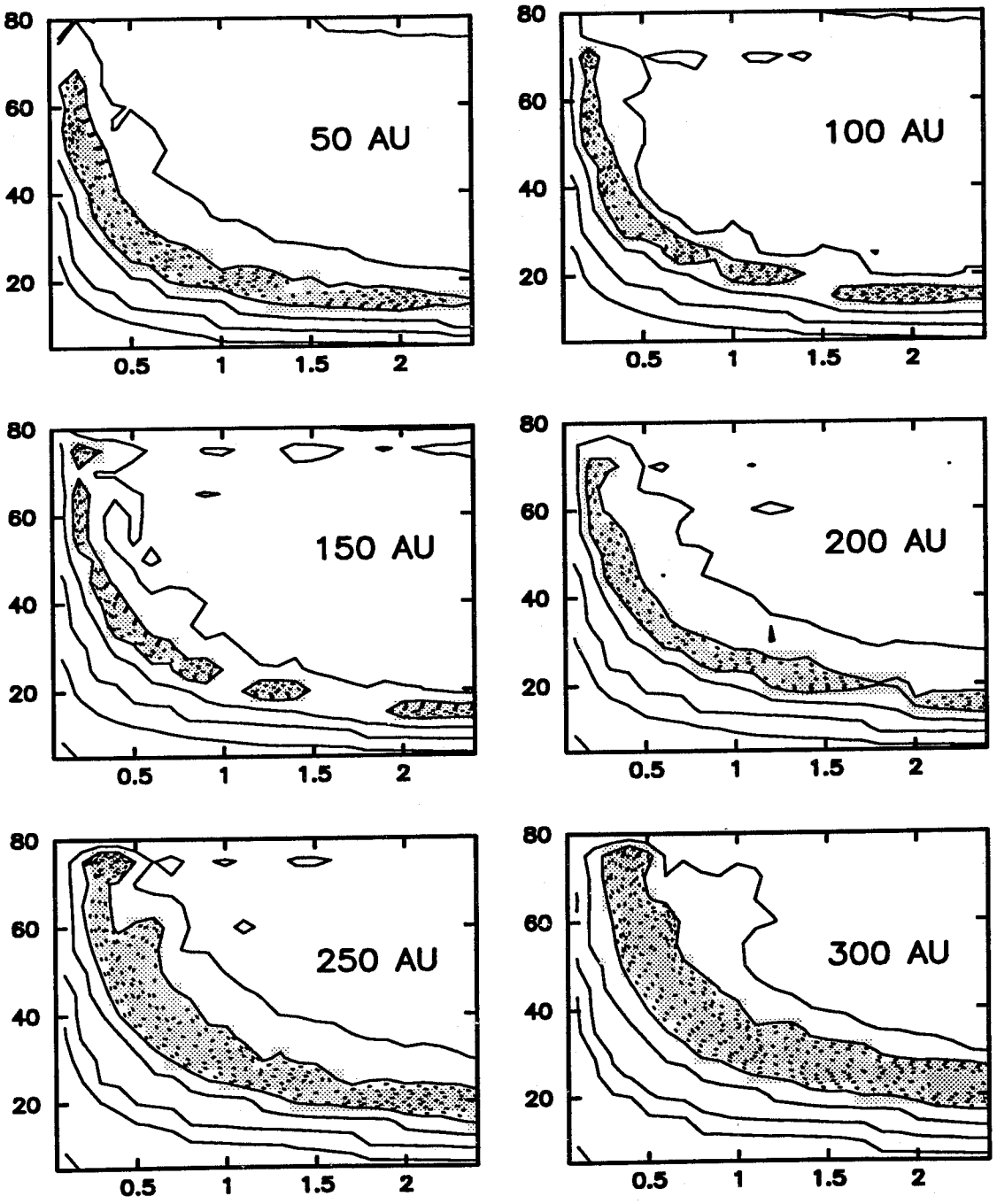

Figure 5.14. Contour maps of the modified correlation coefficient, χ', as a function of the central mass M and the inclination angle i of a model disk. Solid contour levels are at 10% of the maximum attainable value of χ' (1.0) and dotted contours are at 1% intervals, starting at 0.8.

same manner as χ. Results are shown in Figure 5.14 and 5.15.

Contour maps of χ' with respect to M and i show distinct differences from those obtained for low-resolution images of RY and DL Tau with the cross-correlation function alone. A plateau of maximum values has collapsed to a curved ridge with much smaller area, but which still encompasses a large range of M and i values. The location and curvature of a line in the center of this ridge reflects an inverse proportionality between these parameters that is heightened by the explicit introduction of lineshape information into χ' through ΔP. It is analytically approximated by the dependence of the velocity width on M and i as $\Delta V \propto \sin(i)\ M^{1/2}$. The locus of maximum χ' values shifts away from the origin with increases in R_{disk}, reflecting the $\sqrt{2}$ difference in velocity between infalling and rotating gas, but a plot of χ' with respect to R_{disk} (Figure 5.15) fails to clearly eliminate infall or rotation as an interpretation for circumstellar gas motions. This is easily understood as the consequence of low spatial resolution, since the distinction between infall and rotation is largely a geometric effect. Figure 5.15 shows a maximum for both pure infall and pure rotation and a minimum for combined models, but the range of χ' values is small. The best-fit parameter values are $R_{disk} = 310\text{AU}(= R_{out})$, $i = 75°$, and $M = 0.4\ M_{\odot}$. These differ markedly from values obtained by maximizing χ (200 AU, 50°, and 1.6 $M_{\odot}$) or minimizing ΔP (200 AU, 80°, and 0.7 $M_{\odot}$). It is worth noting, however, that the best-fit parameters obtained from using χ alone result in too much emission in neighboring channels, while those from $\Delta\rho$ fail to simulate emission that is positionally coincident with observed emission.

The combined merit function, χ', has been maximized by parameter values which indicate that a nearly edge-on disk is in Keplerian rotation about a star of low mass, while other methods have resulted in disks with a large infall component surrounding stars of higher mass. A worthwhile test of the superiority of χ' as a merit

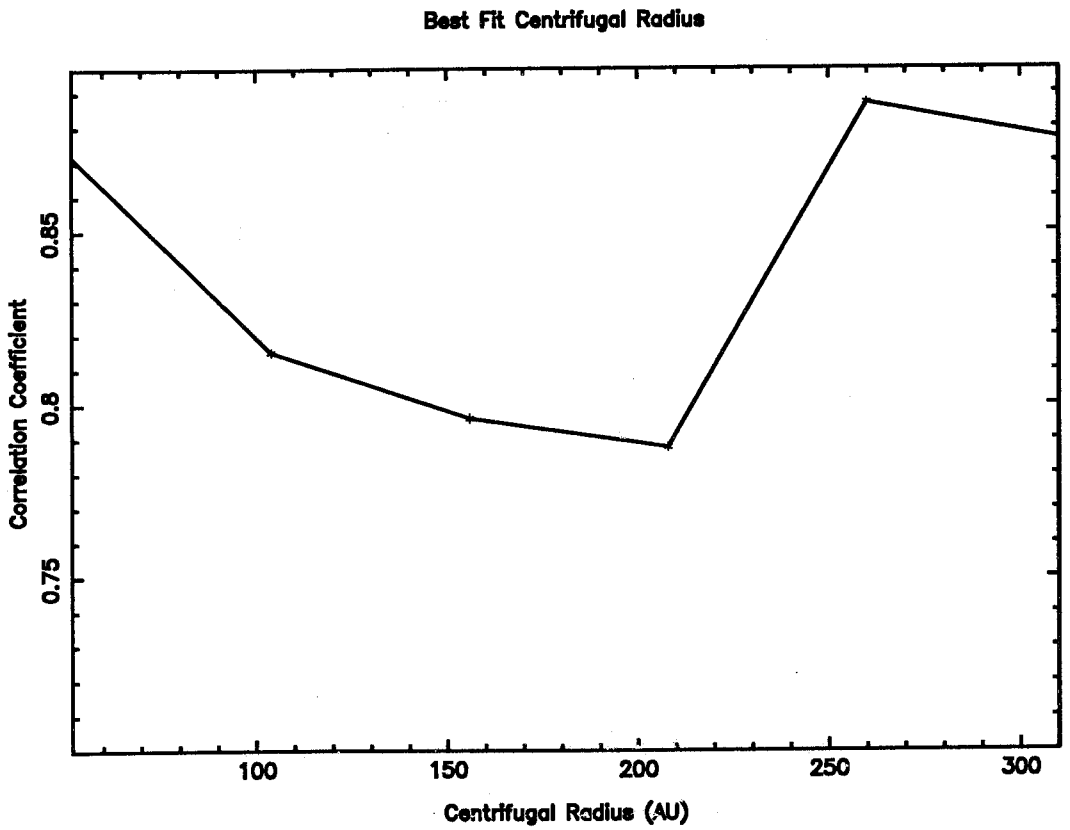

Figure 5.15. Plot of the maximum value of χ with respect to the centrifugal radius. The best-fit value occurs near the outer edge of the disk, but this value is not well constrained due to the low resolution of the images.

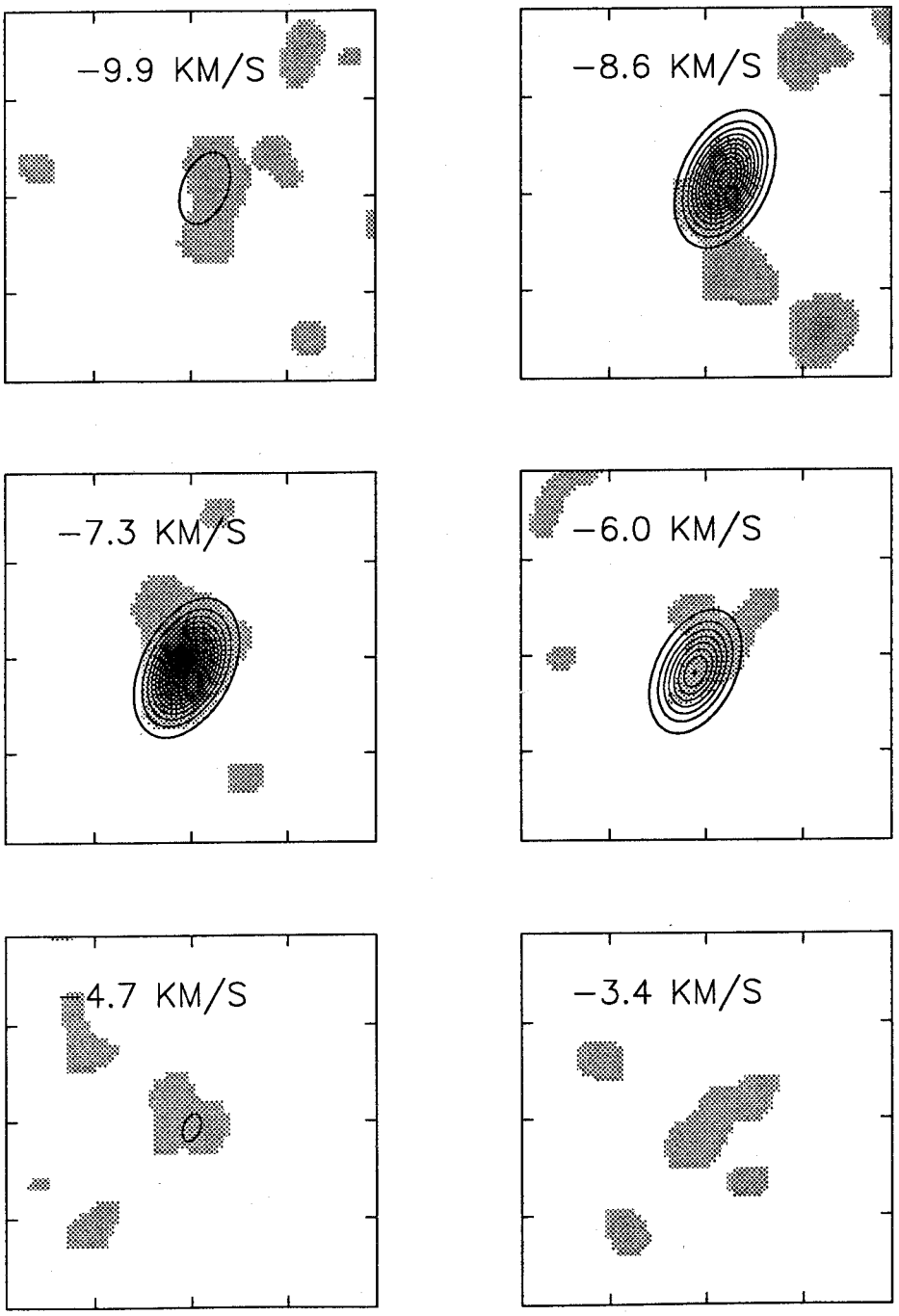

Figure 5.16. Contour maps of a model of AS 209's circumstellar emission superposed on a greyscale representation of aperture synthesis maps seen in Figure 5.13. Best-fit model parameters used in the simulation are R_{disk} = 310 AU, M = 0.4 $M_{\odot}$, and i = 75°. The position and intensity of emission both approximate observed emission.

function is provided by maps constructed from a model with its best-fit parameters, $R_{disk} = 310$ AU, $M = 0.4\ M_{\odot}$, and $i = 75°$, shown in Figure 5.16. Contour plots of model emission show that kinematic patterns are largely unresolved in the synthesized beam, but model-fitting is able to duplicate the position and intensity of grey-scale observed emission. This was not achieved with the use of χ or ΔP alone and suggests that χ' is a suitable function for use with low-resolution data with reliable relative amplitudes. Higher resolution data is necessary to establish best-fit parameter values with certainty, but the results of Figure 5.16 (compare also with Figure 5.13) show that a rotating edge-on disk is consistent with low-resolution molecular line images of circumstellar gas around AS 209.

6. Discussion

Circumstellar gas was successfully detected from all four T Tauri stars observed with the Owens Valley millimeter array in a CO(2→1) survey presented in this work (Chapter 3). Taken with the detections of HL Tau (Sargent & Beckwith 1987, 1991), T Tau (Weintraub *et al.* 1987), DG Tau (Sargent & Beckwith 1989), GG Tau (Kawabe *et al.* 1993; Koerner *et al.* 1993) and GM Aur, this suggests that circumstellar gas is commonly associated with T Tauri stars. A key result of this study has been the discovery that the radial extent of observed gas is generally confined to a small solar-system sized region, much smaller than suggested by earlier observations (Beckwith & Sargent 1993; Sargent & Beckwith 1994). The small size supports the widespread belief that such structures represent circumstellar disks similar to that which gave rise to our solar system (Lin & Papaloizou 1985). However, the small angular size subtended by emitting molecular gas results in an overall reduction of integrated intensity of circumstellar line emission and places concomitantly higher demands on the sensitivity of millimeter arrays. Fractions of the disk which appear at distinct velocities are also correspondingly smaller, raising the level of spatial res-

olution required for kinematic analysis.

The quality of the aperture synthesis images presented in Chapter 3 was sufficient to warrant kinematic analysis with first moment velocity maps and PVDs. These techniques admit multiple kinematic interpretations, since much of the data is averaged, but analysis of molecular line maps strongly supported the hypothesis that the circumstellar gas was rotating. In this chapter, an effort has been made to rigorously identify the kinematic structure of circumstellar material by cross-correlation with a planar model of gas in a parametrized range of kinematic states, from Keplerian rotation to free fall. Results of this analysis support the hypothesis that detected circumstellar gas is largely centrifugally supported and therefore potentially pre-planetary, but the certainty of this conclusion varies from source to source, depending on the degree to which kinematic patterns are resolved. Spatial resolution, $\sim 3''$, was similar for all observations, so the success or failure of kinematic analyses is predominantly a function of source size. Completely satisfying identification of the kinematic state of circumstellar gas was possible only for DO Tau, the source with the largest radial extent of circumstellar emission. Sources for which model-fitting yielded highly suggestive, but inconclusive, results are likely to be definitively interpreted with analyses of observations carried out at higher spatial resolution. Spatial resolution of $1''$ is available with the Owens Valley millimeter array operating in good weather conditions, so marked improvement is already possible. As high-quality data becomes increasingly available, it will be desirable to obtain a more rigorous understanding of the meaning and behaviour of the merit functions, χ and χ'. Monte Carlo simulations should be carried out to quantify the goodness of fit and rigorously estimate the confidence level that should be attached to best-fit parameter values. These undertakings lie beyond the scope of the present work and are better carried out with higher quality data, but analysis presented here takes first steps toward the

numerical simulation of velocity patterns observed from aperture synthesis maps of circumstellar disks and paves the way for refined estimation of their properties.

CHAPTER 6

Summary and Discussion

Work presented here explicitly demonstrates the existence of circumstellar disks around T Tauri stars and establishes that they have properties corresponding to conditions believed to have existed in the early solar nebula. This hypothesis has recently become widely accepted, but only on the basis of circumstantial evidence; for the most part, disk properties have been inferred from models of the wavelength distribution of radiation. All of the principal conclusions presented here, however, follow from direct imaging. Elliptical gaseous structures are spatially resolved and appear in aperture synthesis images associated with the stellar position, with radii of order 100 AU. Lower mass limits for the molecular gas, derived with the assumption that emisson is optically thin, are smaller than the minimum mass nebula and are likely to be greatly exceeded by the true mass, since emission is optically thick out to radial distances of greater than 50 AU. The elongation of circumstellar gas matches the orientation inferred from disk models of the observed polarization of scattered light and, in one instance, is perpendicular to a recently discovered optical jet. Velocity gradients are found parallel to the elongation axis and are consistent with centrifugal support of the gas about the central star. This latter point is the subject of recent controversy, since aperture synthesis images of circumstellar gas around HL Tauri have been interpreted as depicting gas in a free-fall state (Hayashi *et al.* 1993). Since infalling gas is less likely than orbiting gas to assist in planet-forming processes, such an interpretation weakens the conjecture that detected circumstellar matter around young stars leads to the existence of planetary systems around older ones. For this reason, kinematic analysis of the circumstellar gas has been the dominant theme of this research.

Kinematic modeling of spectral line maps of $^{13}CO(2\rightarrow 1)$ emission from GM Aurigae demonstrated Keplerian rotation of circumstellar gas by duplicating systematic patterns of emission seen in maps of the the disk at discrete velocities. This

kinematic signature is essentially unique; no other physically probable velocity configuration is commonly known to produce the observed pattern. Successful analysis requires high quality observations, however. Sensitivity and spatial resolution must be sufficient to identify patterns within very narrow bandwidths. This requirement was met for GM Aur, in part, because rotating molecular gas was detected out to radial distances of 1000 AU from the star; kinematic patterns were correspondingly large and easy to resolve.

Circumstellar molecular emission from all other T Tauri stars detected in this work originated from substantially smaller regions than the disk around GM Aur. Only DO Tauri had a disk large enough to exhibit systematic kinematic patterns. For these small disks, kinematic analyses were carried out which yielded evidence diagnostic of rotation, but these results were not conclusive. First moment velocity maps and Position-Velocity Diagrams (PVDs) indicated that a dominant component of rotation was consistent with the observations of all of the sample considered, but these admitted other interpretations. The strength of these arguments is worthy of consideration. A rotating disk will display a velocity gradient along the semi-major axis of emission, orthogonal to that produced by infall or outflow. The infall diagnosis is clearly non-unique, and the appearance of *any* gradient can be mimicked by the random distribution of very few random clumps of gas if they are sufficiently bright. However, this method is powerfully discriminatory if rotation and infall are the only likely alternatives and the orientation of circumstellar gas is known with certainty. Unfortunately, it is just those disks which are too small to display kinematic patterns for which the orientation of material is most uncertain.

To a first approximation, all of the sources which were too small to display well-resolved kinematic patterns exhibited velocity gradients which were predominantly aligned with the elongation axis of emission. RY Tau and DL Tau showed the

most distinct velocity gradients in first moment velocity maps, but orientations were best determined for DL Tau and AS 209. For this reason, the strongest case for a centrifugally supported disk can be made for circumstellar gas around DL Tau. For AS 209 and RY Tau, the uncertainty in orientation admits a possible infall component to circumstellar gas, but is not likely to be off by more than 45°. This indicates that the *dominant* velocity component of the molecular gas is rotational. Kinematic modeling of emission in spectral line maps further demonstrated that the location and intensity of peak positions varied systematically in a manner consistent with a rotating disk and virtually eliminated the possibility that the velocity gradients observed in moment maps were the product of fortuitously placed random bright clumps. It is thus a conclusion of this work that circumstellar gas around all three of these sources is predominantly in a state of centrifugally support. Evidence for total centrifugal support of circumstellar gas is strongest for DL Tau.

Only one of the T Tauri stars imaged in CO($2 \rightarrow 1$) emission was large enough for circumstellar kinematic patterns to be identified in spectral line maps. Emission from the molecular gas around DO Tauri was well-fit by a model of gas falling onto a 350 AU radius rotating disk. The behaviour of the cross-correlation coefficient, χ, with respect to variations in the centrifugal radius, R_{disk}, and the model replication of prominent morphological features attest to the reliability of this interpretation. In this regard, DO Tau joins HL Tau as the only examples thus far for which evidence of infall has been clearly identified on the basis of the morphology of spectral line maps. Both of these sources are known to display prominent optical jets and have relatively early stellar ages for T Tauri stars. DO Tau is estimated to be 6×10^5 years (Beckwith *et al.* 1990), and HL Tau's age has recently been estimated as less than 10^5 years (Stapelfeldt *et al.* 1994). In contrast, GM Aur and DL Tau show the clearest evidence in this study for total rotation of circumstellar gas. No optical

jet has been detected in either of these and forbidden line emission diagnostic of energetic mass loss is either dramatically reduced or entirely absent (Cabrit *et al.* 1991). Stellar ages, 2×10^6 and 1.2×10^6 years for GM Aur and DL Tau, respectively, are correspondingly higher. These are too few objects from which to draw unassailable general conclusions, but the simultaneous presence of molecular infall and optical jets in the youngest stars and absent infall or energetic outflow in older ones raises a conjecture phrased here in the form of the following question: Are energetic bipolar outflows from young stars correlated with infall *from the molecular cloud*? Strong evidence exists for a correlation between outflows and the presence of circumstellar disks which accrete onto the star (cf. Edwards *et al.* 1993). Observations presented here suggest that the presence of optical jets is also correlated with infall onto the disk. They are also consistent with a timescale of less than 10^6 years for infall of molecular gas.

The issues raised above point out the need for further observations of the molecular gas from a larger sample of T Tauri stars. Future work will first of all reveal to what degree the trends indicated above are maintained in a statistically significant population. Secondary effects on circumstellar evolution, such as stellar mass, the presence of companions, and the effect of the surrounding environment, cannot even be considered here, but may be identified in a larger population. Finally, the sample studied in this work has presented a preliminary picture of a major transition in early stages of disk evolution: the cessation of infall from the molecular cloud. A later transition will be identified in future highly sensitive observations of T Tauri stars: dispersal of the gaseous disk. The timescale for this latter phase is of great importance to theories of giant planet formation.

References

Adams, F. C., and D. N. C. Lin 1993. Transport processes and the evolution of disks. In *Protostars and Planets III* (E. H. Levy, J. I. Lunine and M. S. Mathews, Eds.), pp. 721–748. Univ. of Arizona Press, Tucson.

Adams, F. C., C. J. Lada, and F. H. Shu 1987. Spectral evolution of young stellar objects. *Astrophys. J.*, **312**, 788–806.

Adams, F. C., C. J. Lada, and F. H. Shu 1988. The disks of T-Tauri stars with flat infrared spectra. *Astrophys. J.*, **326**, 865–883.

Adams, F. C., J. P. Emerson, and G. A. Fuller 1990. Submillimeter photometry and disk masses of T-Tauri disk systems. *Astrophys. J.*, **357**, 606–620.

André, P., and T. Montmerle 1994. From T Tauri stars to protostars - circumstellar material and young stellar objects in the ρ Ophiuchi cloud. *Astrophys. J.*, **420**, 837–862.

Bastien, P. 1982. A linear polarization survy of T Tauri stars. *Astron. Astrophys. Suppl.*, **48**, 153–164.

Beckwith, S. V. W., and A. I. Sargent 1991. Particle emissivity in circumstellar disks. *Astrophys. J.*, **381**, 250–258.

Beckwith, S. V. W., and A. I. Sargent 1993a. The occurrence and properties of disks around young stars. In *Protostars and Planets III* (E. H. Levy, J. I. Lunine and M. S. Mathews, Eds.), pp. 521–541. Univ. of Arizona Press, Tucson.

Beckwith, S. V. W., and A. I. Sargent 1993b. Molecular line emission from circumstellar disks. *Astrophys. J.*, **402**, 280–291.

Beckwith, S. V. W., A. I. Sargent, N. Z. Scoville, C. R. Masson, B. Zuckerman, and T. G. Phillips 1986. Small scale structure of the circumstellar gas of HL Tauri

and R Mononcerotis. *Astrophys. J.*, **309**, 755–761.

Beckwith, S. V. W., A. I. Sargent, R. Chini, and R. Güsten 1990. A survey for circumstellar disks around young stellar objects. *Astron. J.*, **99**, 924–945.

Bodenhiemer, P., T. Ruzmaikina, R. D. Mathieu 1993. Stellar multiple systems: constraints on the mechanism of origin. In *Protostars and Planets III* (E. H. Levy, J. I. Lunine and M. S. Mathews, Eds.), pp. 367–404. Univ. of Arizona Press, Tucson.

Boss, A. P., and H. W. Yorke, 1993. An alternative to unseen companions to T Tauri stars. Submitted for publication.

Cabrit, S., S. Edwards, S. E. Strom, and K. M. Strom 1991. Forbidden-line emission and infrared excesses in T-Tauri stars – Evidence for accretion-driven mass loss. *Astrophys. J.*, **354**, 687–700.

Cassen, P. M., and A. Moosman 1981. On the formation of protostellar disks. *Icarus*, **48**, 353–376.

Cassen, P. M., F. H. Shu, and S. Tereby 1985. Protostellar disks and star formation: An overview. In *Protostars and Planets II* (D. C. Black and M. S. Mathews, Eds.), pp. 448–482. Univ. of Arizona Press, Tucson.

Chandler, C. J., and A. I. Sargent 1993. The small-scale structure and kinematics of B335. *Astrophys. J.*, **414**, L29–L32.

Cohen, M., and L. V. Kuhi 1979. Observational studies of pre-main-sequence evolution. *Astrophys. J. Suppl.*, **41**, 743–843.

D'Antona., F., and I. Mazzitelli 1993. New pre-main sequence tracks for M$\leq$2.5$M_{\odot}$ as tests of opacities andf convection models. *Astrophys. J. Suppl.*, **90**, 467–500.

de Geus, E. J., Bronfman, L., & P. Thaddeus 1990. A CO survey of the dark clouds in Ophiuchus. *Astron. Astrophys.*, **231**, 137–150.

Draine, B. T., and H. M. Lee 1984. Optical properties of interstellar graphite and silicate grains. *Astrophys. J.*, **285**, 89–108.

Dutrey A., S. Guilloteau, and M. Simon 1994. Images of the GG Tauri rotating ring. *Astron. Astrophys.*, **286**, 149–159.

Dyck, H. M., T. Simon, and B. Zuckerman 1982. Discovery of an infrared companion to T Tauri. *Astrophys. J.*, **255**, L103–L106.

Edwards S., T. Ray, and R. Mundt 1993. Energetic mass outflows from young stars. In *Protostars and Planets III* (E. H. Levy, J. I. Lunine and M. S. Mathews, Eds.), pp. 567–602. Univ. of Arizona Press, Tucson.

Elias, J. 1978. A study of the Taurus dark cloud complex. *Astrophys. J.*, **224**, 857–872.

Elsasser, H., and H. J. Staude 1978. On the polarization of young stellar objects. *Astron. Astrophys.*, **70**, L3–L6.

Feigelson, E. D., and W. M. DeCampli 1981. Observations of x-ray emission from T Tauri stars. *Astrophys. J.*, **243**, L89–L93.

Fukui, Y., T. Iwata, A. Mizuno, J. Bally, and A. P. Lane 1993. Molecular outflows. In *Protostars and Planets III* (E. H. Levy, J. I. Lunine and M. S. Mathews, Eds.), pp. 603–639. Univ. of Arizona Press, Tucson.

Galli, D., and F. H. Shu 1993. Collapse of magnetized molecular cloud cores. 1. Semianalytical solution. *Astrophys. J.*, **417**, 220–242.

Galli, D., and F. H. Shu 1993. Collapse of magnetized molecular cloud cores. 2. Numerical results. *Astrophys. J.*, **417**, 243–258.

Ghez, A., G. Neugebauer, and K. Mathews 1993. The multiplicity of T Tauri stars in the star-forming regions Taurus Auriga and Ophiucus Scorpius - a 2.2 micron speckle imaging survey. *Astron. J.*, **106**, 2005–2023.

Hartmann, L., R. Hewett, S. Stahler, and R. D. Mathieu 1986. Rotational and radial velocities of T-Tauri stars. *Astrophys. J.*, **309**, 275–293.

Hartmann, L., B. F. Jones, J. R. Stauffer, and S. J. Kenyon 1991. A proper motion survey for pre-main-sequence stars in Taurus-Auriga. *Astron. J.*, **101**, 1050–1062.

Hayashi, M., N. Ohashi, and S. M. Miyama 1993. A dynamically accreting gas disk around HL Tauri. *Astrophys. J.*, **418**, L71–L74.

Henning, T., W. Pfau, H. Zinnecker, and T. Prusti 1994. A 1.3-mm survey for circumstellar dust around young Chameleon objects. *Astron. Astrophys.*, **276**, 129–141.

Herbig, G. H., and K. R. Bell 1988. Third catalog of emission line stars of the Orion population. In *Lick Observatory Bull. No. 1111.* (Univ. of California).

Hildebrand, R. H. 1983. The determination of cloud masses and dust characteristics from submillimetre thermal emission. *Quart.J.R.A.S.*, **24**, 267–282.

Hirth, G. A., R. Mundt, and J. Solf 1994. Jet flows and disk winds from T Tauri stars - the case of CW Tau. *Astron. Astrophys.*, **285**, 929–942.

Hirth, G. A., R. Mundt, J. Solf, and T. P. Ray 1994. Asymmetries in bipolar jets from young stars. *Astrophys. J.*, **427**, L99–L102.

Kawabe, R., M. Ishiguro, T. Omodaka, Y. Kitamura, and S. M. Miyama 1993. Discovery of a rotating protoplanetary gas disk around a young star GG-Tau. *Astrophys. J.*, **404**, L63–L66.

Kenyon. S. J., N. Calvet, and L. Hartmann 1993a. The embedded young stars in the

Taurus-Auriga Molecular Cloud. 1. Models for Spectral Energy Distributions. *Astrophys. J.*, **414**, 676–694.

Kenyon, S. J., B. A. Whitney, M. Gomez, and L. Hartmann 1993b. The embedded young stars in the Taurus-Auriga Molecular Cloud. 2. Models for scattered-light images. *Astrophys. J.*, **414**, 773–792.

Kleiner, S. C., and R. L. Dickman 1984. Large-scale structure of the Taurus molecular complex. I. Density fluctuations - a fossil jeans length?. *Astrophys. J.*, **286**, 255–262.

Koerner, D. W., A. I. Sargent, and S. V. W. Beckwith 1993. Gas and dust in the pre-main-sequence multiple system GG Tauri. *Astrophys. J.*, **408**, L93–L96.

Lin, D. N. C., and J. Papaloizou 1985. On the dynamical origin of the solar system. In *Protostars and Planets II* (D. C. Black and M. S. Mathews, Eds.), pp. 981–1072. Univ. of Arizona Press, Tucson.

Marsh, K. A., and M. J. Mahoney 1992. Evidence for unseen companions around T Tauri stars. *Astrophys. J.*, **395**, L115–L118.

Mathieu, R. D., F. C. Adams, and D. W. Latham 1991. The T Tauri spectroscopic binary GW Orionis. *Astron. J.*, **101**, 2184–2198.

Myers, P. C., and P. J. Benson 1983. Dense cores in dark clouds: II. NH_3 observations and star formation. *Astrophys. J.*, **266**, 309–320.

Natta, A. 1993. The temperature profile of T Tauri disks. *Astrophys. J.*, **412**, 761–770.

Ohashi, N., R. Kawabe, M. Hayashi, and H. Ishiguro 1991. Observations of 11 protostellar sources in Taurus with the Nobeyama Millimeter Array: growth of circumstellar disks. *Astron. J.*, **102**, 2054–2065.

Richer, J. S., and R. Padman 1991. The position velocity diagrams of protostellar disks. *Mon. Not. Royal Astron. Soc.*, **251**, 707–718.

Rydgren, A. E., and F. J. Vrba 1983. Additional UBVRI and JHKL photometry of T Tauri stars. *Astron. J.*, **88**, 1017–1026.

Safronov, V. S. 1991. Kuiper prize lecture: some problems in the formation of planets. *Icarus*, **94**, 260–271.

Sargent, A. I., and S. Beckwith 1987. Kinematics of the circumstellar gas of HL Tauri and R Monocerotis. *Astrophys. J.*, **323**, 294–305.

Sargent, A. I., and S. Beckwith 1991. The molecular structure around HL Tauri. *Astrophys. J.*, **382**, L31–L35.

Sargent, A. I., and S. Beckwith 1993. Disks around T Tauri stars. In *Millimeter and Submillimeter Wave Interferometry* (M. Ishiguro, R. Kawabe, Eds.), pp. 232–254. BookCrafters, San Francisco.

Scoville, N. Z., A. I. Sargent, D. B. Sanders, M. J. Claussen, C. R. Masson, K. Lo, and T. G. Phillips 1986. High-resolution mapping of molecular outflows in NGC2071, W49, and NGC7538. *Astrophys. J.*, **303**, 416–432.

Shu, F. H. 1977. Self-similar collapse of isothermal spheres and star formation. *Astrophys. J.*, **214**, 488–497.

Skrutskie, M. F., D. Dutkevitch, S. E. Strom, S. Edwards, and K. M. Strom 1991. A sensitive 10 μm search for emission arising from circumstellar dust associated with solar-type pre-main-sequence stars. *Astron. J.*, **99**, 1187–1195.

Skrutskie, M. F., R. Snell, D. Dutkevitch, S. E. Strom, and F. P. Schloerb 1991. A search for remnant molecular disks around young nearby stars. *Astron. J.*, **102**,

1749–1752.

Skrutskie, M. F., R. L. Snell, K. M. Strom, S. E. Strom, and S. Edwards 1993. Detection of circumstellar gas associated with GG Tauri. *Astrophys. J.*, **409**, 422–428.

Snell, R. L., R. B. Loren, and R. L. Plambeck 1980. Observations of CO in L1551: evidence for stellar wind driven shocks. *Astrophys. J.*, **239**, L17–L22.

Stahler, S. W., D. G. Korycansky, M. J. Brothers, and J. Touma 1994. Early evolution of protostellar disks. *Astrophys. J.*, **431**, 341–358.

Stapelfeldt, K. R., C. J. Burrows, J. Krist, J. J. Hester, J. Trauger, G. Ballester, S. Casertano, J. Clarke, D. Crisp, R. W. Evans, J. S. Gallagher, R. E. Griffiths, J. G. Hoessel, J. A. Holtzman, J. R. Mould, P. Scowen, A. M. Watson, and J. A. Westphal, WFPC2 Imaging of the circumstellar nebulosity of HL Tauri. Submitted to *Astrophys. J.*, 1994.

Strom, K. M., S. E. Strom, S. Edwards, S. Cabrit, and M. F. Skrutskie 1989. Circumstellar material associated with solar-type pre-main-sequence stars – a possible constraint on the timescale for planet building. *Astron. J.*, **97**, 1451–1470.

Tamura, M., and S. Sato 1989. A 2 micron polarization survey of T-Tauri stars. *Astron. J.*, **98**, 1368–1381.

Terebey, S., F. H. Shu, and P. Cassen 1984. The collapse of the cores of slowly rotating isothermal clouds. *Astrophys. J.*, **286**, 529–551.

Ungerechts, H., and P. Thaddeus 1987. A CO survey of the dark nebulae in Perseus, Taurus, and Auriga. *Astrophys. J. Suppl.*, **377**, 510–518.

van Langevelde, H. J., E. F. van Dishoeck, and G. A. Blake 1994. Evidence for

HCO^+ infall toward T Tauri? *Astrophys. J.*, in press.

Weidenschilling, S. J. 1977. The distribution of mass in the planetary system and solar nebula. *Astrophys. Space Sci.*, **51**, 153–158.

Weintraub, D. A., C. R. Masson, and B. Zuckerman 1987. Measurements of Keplerian rotation of the gas in the circumbinary disk aroun T Tauri. *Astrophys. J.*, **344**, 915–924.

Weintraub, D. A., G. Sandell, and W. D. Duncan 1989. Submillimeter measurements of T Tauri and FU Orionis stars. *Astrophys. J.*, **340**, L69–L72.

Weintraub, D. A., C. R. Masson, and B. Zuckerman 1989. Measurements of Keplerian rotation of the gas in the circumbinary disk around T Tauri. *Astrophys. J.*, **344**, 915–924.

Whitney, B. A., and L. Hartmann 1992. Model scattering envelopes of young stellar objects. 1. Method and application to circumstellar disks. *Astrophys. J.*, **395**, 529–539.

Whitney, B. A., and L. Hartmann 1993. Model scattering envelopes of young stellar objects. 2. Infalling envelopes. *Astrophys. J.*, **402**, 605–622.

Whittet, D. C. B. 1974. The ratio of total to selective absorption in the Rho Ophiuchi cloud. *Mon. Not. Royal Astron. Soc.*, **168**, 371–378.

Yamashita, T., T. Handa, T. Omodaka, Y. Kitamura, E. Kawazoe, S. Hayashi, and N. Kaifu 1993. Upper limits to the CO J=1–0 emission around Vega-like stars: gas depletion of the circumstellar ring around ϵ Eridani. *Astrophys. J.*, **402**, L65–L67.

Zhou, S. D., N. J. Evans, C. Kompe, and C. M. Walmsley 1993. Evidence for proto-

stellar collapse in B335. *Astrophys. J.*, **404**, 232–246.